Czech Technical University

Faculty of Electrical Engineering

Department of Physics

Daria Miliaieva

ASSEMBLY AND OPTOELECTRONIC PROPERTIES OF NANODIAMOND-DYE COMPOSITES

Doctoral Thesis

Supervisor: prof. RNDr. Bohuslav Rezek PhD.

PhD programme: Electrical Engineering and Information Technology (P2612)

Study Branch: Electrotechnology and Materials (2602V009)

August 2019

Acknowledgements

Declaration of Honour

I, Daria Miliaieva, hereby declare that this dissertation thesis is the result of my own work and that I cited all the information sources I used. This thesis has not been submitted either in whole or part for a degree at any other university or institution. The printed version is equivalent to the submitted electronic one. Also, I agree with the publication of the thesis.

Abstract

Nanoscale composite of detonation nanodiamond (DND) and polypyrrole (PPy) as an organic dye was explored as a novel concept for energy generation, using nanodiamond as an inorganic electron acceptor. We established technology for the composite layer-by-layer synthesis that is suitable for solar cell fabrication. The formation, pronounced material interaction, and photovoltaic properties of DND/PPy composites were characterised down to nanoscale by atomic force microscopy, infrared spectroscopy, Kelvin probe and electronic transport measurements. The data showed that DNDs with different surface terminations (hydrogenated, oxidised, poly-functional) assemble PPy oligomers in different ways. This led to the composites with different optoelectronic properties. Tight material interaction resulted in significantly enhanced photovoltage and broadband (1 - 3.5 eV) optical absorption in DND/PPy composites compared to pristine DND and PPy. Combination of both oxygen and hydrogen functional groups on the nanodiamond surface appears to be the most favourable for the optoelectronic effects. Theoretical density functional theory calculations corroborated the experimental data. Prototype hybrid solar cell demonstrated the functionality of the concept.

Keywords: Nanodiamond, polypyrrole, atomic force microscopy, photovoltaics.

Abstrakt

Nanoškálový kompozit detonačního nanodiamantu (DND) a organického barviva polypyrrolu (PPy) byl zkoumán jako nový koncept pro výrobu energie, kde nanodiamant byl využit jako anorganický akceptor elektronů. Zavedli jsme technologii pro syntézu kompozitu vrstvu po vrstvě, která je vhodná pro výrobu solárních článků. Formace, výrazná interakce v rámci materiálu a fotovoltaické vlastnosti DND/PPy kompozitů byly charakterizovány na nanoškále pomocí mikroskopie atomárních sil, infračervené spektroskopie, Kelvinovy sondy a měření elektronického transportu. Data ukázala, že DND s různými povrchovými zakončeními (hydrogenované, oxidované, polyfunkční) interagují a navazují oligomery PPy různými způsoby. To vede ke vzniku kompozitů s různými optoelektronickými vlastnostmi. Výsledkem těsné interakce v rámci materiálu je významně zvýšené fotonapětí a širokopásmová optická absorpce (1 - 3,5 eV) v DND/PPy kompozitech ve srovnání s původním DND a PPy. Pro optoelektronické efekty se jeví jako nejpříznivější kombinace kyslíkových a vodíkových funkčních skupin na nanodiamondovém povrchu. Prezentované experimentální data jsou podpořeny teoretickými výpočty pomocí teorie hustotního funkcionálu. Funkčnost tohoto konceptu byla prokázána prototypovým hybridním solárním článkem.

Klíčová slova: Nanodiamant, polypyrrol, mikroskopie atomárních sil, fotovoltaika.

Contents

Aims of the thesis

The thesis aims at investigating interactions between the nanodiamond particles and polypyrrole for the feasible photovoltaic applications. The objectives of the thesis are (a) to develop the fabrication scalable and inexpensive technique for nanodiamond-polypyrrole synthesis; (b) to find methods of bonding nature investigation in the nanocomposite; (c) to extensively study its optoelectronic properties and stability, both short- and long-term; (d) to bring understanding in the charge transfer mechanism in the nanodiamond-polypyrrole composite by combining the results of the experimental methods and theoretical calculations; (e) to construct and test the prototype solar cell with nanodiamond-polypyrrole as active material.

1. Introduction

The cost of electricity from photovoltaic (PV) modules is expected to slide down compared to the cost of the conventional sources of electrical energy by 2032.[1] It is of no wonder since PV field is advancing rapidly. One of the most unprecedented development has occurred in organic photovoltaic (OPV), which is an attractive type of photovoltaics due to its raw materials low-cost, flexibility and low-energy roll-to-roll fabrication technology.[2] In the past 4-5 years, organic solar cell efficiencies have risen from 4% to over 16% in single-junction architectures[3–6] and exceed 17% in multi-junction devices.[7] It is now predicted that 20% is achievable shortly.[8,9] Still, the power conversion efficiency of OPV devices is lower than the efficiencies of the nowadays PV leaders: multi-junction solar cell GaInP/GaAs/GaInAsP/GaInAs with the light concentrator (44.7%)[10]; crystalline silicon heterojunction (26.7%)[11] and perovskite/silicon tandem (28.0%)[12] solar cells. However, the record efficiencies are typically achieved on laboratory scale samples while OPV is the established technology capable fabricating large-area solar cell installations. Therefore, despite generally lower efficiency of OPV cells compared to the record ones, the research on materials for organic photovoltaics (OPV) is going on for improving efficiency and for addressing some lasting problems like long-term stability.[7]

In the OPV system, organic substances that play the roles of the donor (D) and acceptor (A) of electrons are combined. Basic stages of OPV functioning could be defined as (1) creation of the exciton by light-absorbing substance (could be either D or/and A); (2) transfer of the exciton to the interface of D and A; (3) dissociation of the exciton if there is proper band alignment of D and A;[13] (4) transfer of the free charges (holes and electrons) through D and A to the electrodes with subsequent delivery of charges into the external circuit.

The problem may occur while transferring the exciton to D-A interface due to short exciton diffusion length in organic materials (about 10 nm). First-generation organic solar cells which brought together D and A layers proved to have low power conversion efficiency (under 1%).[14] For sufficient light-harvesting, the thicknesses of D and A layers used in these OPV were 100-200 nm. Due to such thicknesses exciton created in light-absorbing area recombined before it could reach the interface of D and A. Therefore bulk heterojunction (BHJ) became a good alternative for solar cells with

3

layered D and A increasing OPV power conversion efficiency from 0.1 to 7.4%.[15] In BHJ nanodomains of D and A of the size of the exciton diffusion length are brought together. In this case, exciton reaches D-A interfaces before its recombination.[14,15] The drawback, which decreases the efficiency of BHJ, are non-continuous percolation pathways for the free charges from the place of exciton dissociation at D-A interface to the corresponding electrodes.[16] Annealing of BHJ after fabrication arranges D and A nanodomains and improves the performance of solar cell.[16]

Semiconducting conjugated polymers are most commonly used as the donor materials for OPV due to broad solar spectrum absorption,[17,18] mechanical flexibility[19] and less expensive fabrication in large scale.[16] The classical OPV donors are MEH-PPV, P3HT, PCPDTBT, PFDTBT, PCzDTBT etc.[20] Lately new type of donors appeared, namely conjugated polymers which incorporate both donor and acceptor moieties.[21] The energy-level hybridisation of the donor and acceptor units in such polymers leads to the extraordinarily narrow bandgaps (1.2-1.9 eV) and consequently, to effective light absorption and enhanced performance of a solar cell.[22]

Until recently the best seller blend for organic solar cells was a combination of P3HT conjugated polymer with the fullerene derivatives, such as [6,6]-phenyl-C_{61}-butyric acid methyl ester ($PC_{60}BM$) and its analogue [6,6]-phenyl-C_{71}-butyric acid methyl ester ($PC_{70}BM$).[23,24] The record fullerene-based blend efficiency of 7.4% was achieved in a blend of indene-C_{60}-bisadduct (ICBA) and P3HT.[25] High synthesis cost, limited optical absorption, poor bandgap tunability, morphological and photochemical instability of commonly used fullerenes promotes the research of the alternatives of fullerenes for light-harvesting blends.[26–28] Small molecule non-fullerene acceptors (NFA) made a break-through in OPV efficiency in the past few years due to their optical properties and electronic levels tunability as well as high thermal, photochemical and morphological stability.[9] The most promising NFA classes are rylene diimide-based materials and materials with fused aromatic cores with strong electron-accepting end groups.[29]

Substituting organic acceptor in OPV with inorganic nanoparticles can bring the benefits, namely (1) improvement of optoelectronic stability of the solar cells; (2) enhancement of the light absorption range by changing the size or surface chemistry of the nanoparticle and consequently, its bandgap; (3) enhancement of the light-harvesting since the rate of the photoinduced charges transfer in the inorganic material is of a

picosecond order and faster than their recombination rate; (4) morphology of the inorganic materials is tailorable to produce simultaneously efficient exciton dissociation interfaces and free charge-transporting pathways.[30,31] In this respect, the different forms of carbon have been under investigation for the role of electron acceptor in OPV. Single wall carbon nanotubes (SWCNT) may be used for fabrication of the blend with a polymer for photovoltaic applications due to their excellent transport properties.[32] The highest efficiency 0.72% was reported for the composite of SWCNT coated with the ordered layer of P3HT.[33]

Graphene having high electrical conductivity and charge mobility (~104 cm^{2}V^{-1}s^{-1} at room temperature) while being transparent is a suitable material for applications in optoelectronic devices as well.[32] Liu et al.[34] fabricated solar cells based on the mixture of graphene, functionalized by phenyl isocyanate, and P3HT with the power conversion efficiency of 1.1% (compared to pristine P3HT efficiency of 0.005%).

Bulk diamond interface with the semiconducting conjugated polymer polypyrrole (PPy) was shown to provide facile exciton dissociation.[35] This property of the diamond-PPy composite is beneficial for free charge generation. Considering the good conductivity of PPy[36] and its ability to absorb visible light,[37] the diamond-PPy composite could be a valuable light-harvesting component for photovoltaic devices. At the same time, the covalent bond detected between hydrogenated bulk diamond and PPy[38] could provide strong interaction and stabilisation between the components of the composite.

If bulk diamond in the diamond-PPy composite was substituted with the detonation nanodiamond (DND), the cost of composite fabrication technology would decrease greatly because of inexpensive and large-scale DNDs production.[39] In this work, we, therefore, focused on the fabrication of DND/PPy composites by novel wet-chemical technology. The technology immobilised layers of DND particles on substrates and grafted PPy oligomers to them in order to assure continuous percolation pathways for the free charges (generated from the dissociated excitons at the interface of the materials) to the corresponding electrodes and provide a suitable processing method for large-area solar cell fabrication. We explored properties of the fabricated DND/PPy composites with view to their prospective application in photovoltaics: the interaction between PPy and DND of different terminations (polyfunctional, hydrogenated, oxidised) was investigated by Fourier-transform infrared spectroscopy

5

(GAR-FTIR) and scattering-type near-field optical microscopy combined with infrared spectroscopy (SNOM-IR); PPy morphology and thickness in the composites were obtained by atomic force microscopy (AFM); optical absorption spectra were recorded by photothermal deflection spectroscopy (PDS); optoelectronic properties and their long-term stability was investigated by means of Kelvin Probe method. Also, we fabricated the prototype solar cells with DND/PPy composites and examined their current-voltage characteristics.

1.1 Detonation nanodiamond

Nanodiamonds represent a relatively novel type of carbon nanomaterial. Nanodiamonds denote nanoparticles in sizes below 100 nm and even down to 1 nm[40] that are composed of diamond and often also of other carbon phases. The most common and widely available are the nanodiamonds synthesised by the controlled detonation of explosives, so-called detonation nanodiamonds (DNDs). DNDs are obtained from a wide variety of explosives. Most often it is mixture of TNT (2-methyl-1,3,5-trinitrobenzene) and RDX (1,3,5-trinitroperhydro-1,3,5-triazine). The explosion takes place in the detonation chamber in an inert medium of either gas (Ar, N_2, etc.) or water (ice). During the detonation of explosive, high pressure and high temperature are kept only for a fraction of microsecond restricting the size of DNDs. Based on X-ray diffraction analysis, the size distribution of primary DND particles is in the range of 2 to 10 nm with a mean size of 4-5 nm. After the formation of the primary particles, they continue to move in the turbulent flow inside the detonation chamber colliding with each other and the walls of the chamber. Thereby agglomerates of the particles are formed with sizes of several hundred nanometers. The forces that keep together DND in the form of special kind of agglomerates, so-called core agglutinates, differ from electrostatic and van der Waals forces.[41] There are available techniques to disintegrate agglutinates down to primary particles by milling DND soot with metallic beads, sonication of DNDs in oversaturated salt solution [42] or annealing in air.[40]

The properties of the primary DND particle depend on its size, chemical termination of its surface and impurities in the core of the particle. In general, the smaller the particle, the more reactive it is.[41] For example, during air annealing, the smallest particles are burnt in the first row compared to larger ones. FTIR analysis of commercial DND after purification (usually it is treatment in mineral acids) shows the presence of CH and COOH, lactone, ether and carbonyl groups, while Raman spectroscopy reveals sp^2 carbon on the surface of DNDs. The distribution of the surface groups is likely not uniform and dependent on the particular DND facet.[43]

In Figure 1, subsequent building up of the adamantane $C_{10}H_{16}$ – the elementary unit of the diamond - to diamantane and triamantane (so-called diamondoids) is shown. When the size of the built-up particle reaches a few nanometers, it starts to be called nanodiamond. It could be seen that there are two types of C atoms in adamantane and diamondoids: connected to either one or two H atoms. Analogously primary Carbon atoms (sp^3 Carbon bonded to 1 H atom) in nanodiamond form [111] plane, while

secondary C atoms form [100] plane. The planes (facets) surface energies are different, which could be the reason for different surface terminations of [111] and [100] facets as in the case of the bulk diamond.[44]
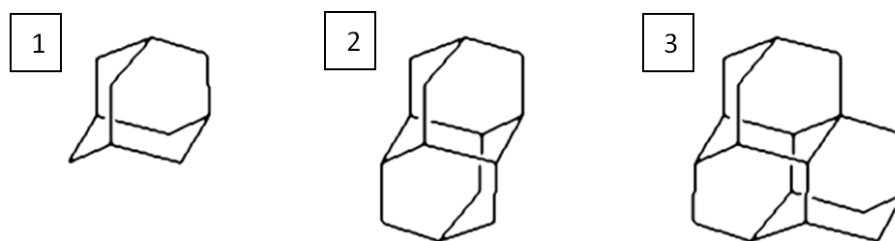

Figure 1. (1) Adamantane　(2) Diamantane　(3) Triamantane.[41]

Various techniques are available to change DNDs surface termination.[41] Complete hydrogenation of DND seems to be still a challenging task. In one of the hydrogenation method DNDs were subjected to 500 ^{0}C at 10 mbar for 5 hours.[45] There are obvious changes in the FTIR spectrum after hydrogenation (appearance of the band around 2800 cm^{-1} which is attributed to CH vibrations), but still, some features of oxygen-containing groups are present in hydrogenated DNDs. In another hydrogenation method, the authors used 800 W microwave hydrogen plasma to treat oxidised DNDs.[46] The resulting sample showed a reduction of carbonyl groups and an increase in the amount of CH and OH groups.

Oxidation of DNDs is possible either by treatment with mineral acids or by annealing in air at temperatures around 425 ^{o}C (higher temperatures may cause oxidation of the core of DND particle and DND size reduction).[47] Oxidised DNDs are hydrophilic compared to hydrophobic hydrogenated DNDs.[48] Electronic properties of hydrogenated and oxidised DNDs are expected to be different as well.[49]

Oxidised and hydrogenated surfaces can be used as a starting point for further functionalization of DND. One of the first complex moieties grafted to oxidised nanodiamond was trialkoxy silanes.[50] Final product siloxane can be used to study biodistribution.[51] Hydrogenated DNDs were used for aryl diazonium salts functionalization. Aryl diazonium group on nanodiamond can further be transformed into a variety of derivatives such as aryl halogenides, phenols, aryl nitriles etc.[41] Thus, grafting of organic dyes, such as polypyrrole that was used on the bulk diamond, should be feasible also on nanodiamonds. For this, a suitable technology must be developed.

1.2 Polypyrrole

Polypyrrole is conjugated polymer dye that can absorb light in a broad visible spectral range, from ultraviolet to near-infrared [52]. Synthesis of polypyrrole oligomer is schematically represented in Figure 2. The polymerisation starts from the withdrawal of 1 electron from Py monomer by an oxidiser. The oxidising effect can be provided either by a chemical substance (ferric chloride, potassium dichromate, potassium permanganate, oxygen), illumination, or positive potential at the electrode immersed in Py solution.
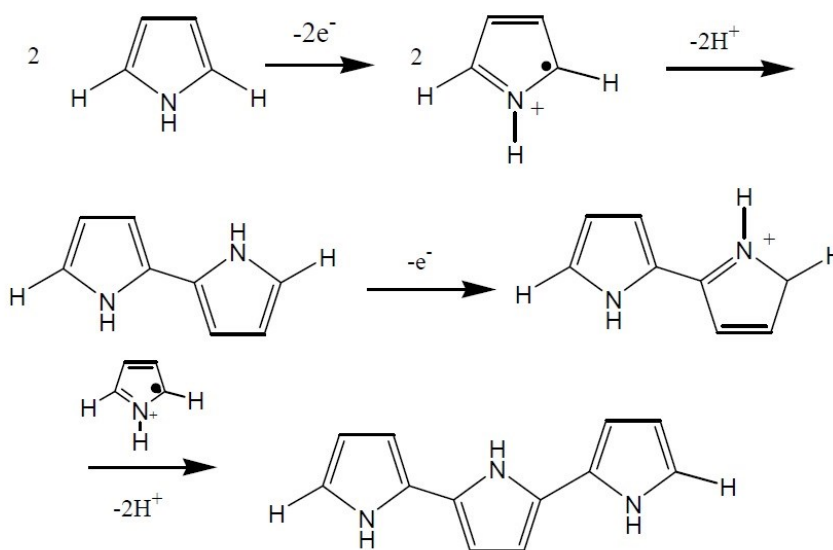
Figure 2. Schematic process of oxidation of pyrrole monomers to polypyrrole oligomer.[53]

The radical-cations form the dimer that is subsequently oxidised and polymerised with new cation-radical. The reaction proceeds until chain terminates, e.g. due to sterical hindrance. The final polymer is black insoluble and chemically stable non-toxic material, although the electronic properties can be adjusted with a variation of the counterions on the polymer chain. If the polymer is further oxidised, it gives rise to polarons (Figure 3) – the particle with separated electron and hole in every unit of 2.5 - 4 Py monomers.[54] There are 2 states (bonding and antibonding polaron states) that appear in the bandgap of PPy after removal of 1 electron.[52] The allowed transitions between the states in PPy chain with polaron: (1) from valence band to conduction band (HOMO-LUMO transition, 3.2 eV), (2) from valence band to antibonding level of

polaron (2.1 eV), (3) from valence band to bonding level of polaron (0.7 eV), (4) from bonding level of polaron to its antibonding level (1.4 eV). [52]
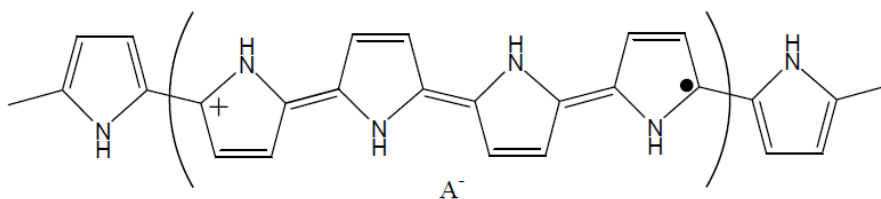

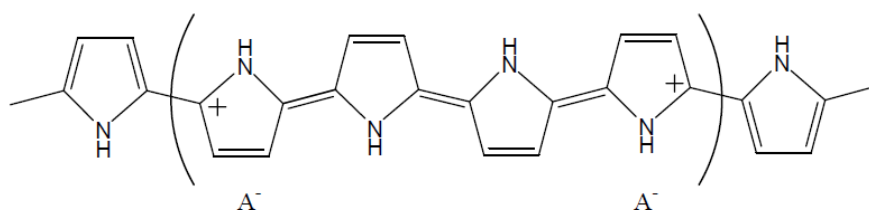**Figure 3**. The formula of 1 elementary unit of polaron.[55]

Figure 4. The formula of 1 elementary unit of bipolaron.[55]

The removal of 2 electrons from the charged unit results in 2 positive charges per unit. Such formation is called bipolaron (Figure 4). The mobility of electrons is higher in bipolarons units compared to polaron units. Therefore, the conductivity is larger in materials where bipolarons are the major charge carriers. Counter-ions influence the delocalisation of the charge and the proportion between polaron and bipolaron states in the chain and finally, conductivity. Bipolarons add 2 bands in the bandgap of PPy. The allowed transitions between the bands in PPy chains with bipolarons are the following (1) from the valence band to conduction band (3.6 eV), (2) from valence band to antibonding bipolaron band (2.7 eV) and (3) from valence band to bonding bipolaron band (1.0 eV). Thus, a broad absorption band can be expected, which can be modified by doping. [54]

Figure 5 shows optical absorption spectra of PPy with different dopants like anthraquinone-2-sulfonate (PPy:AQS⁻), toluene sulfonate (PPy:p-TS⁻), chloride (PPy:Cl⁻). The larger the absorbance, the larger the conductivity. EPS and Raman studies of the PPy with different dopant anions reveal that PPy: AQS⁻ has the largest fraction of bipolarons compared to PPy: p-TS⁻ and especially PPy:Cl⁻ (in which paramagnetic polarons were proved to be the dominant charges). Therefore, NIR band

of optical absorption spectra is produced by bipolarons and such charge distribution is responsible for high conductivity[54].
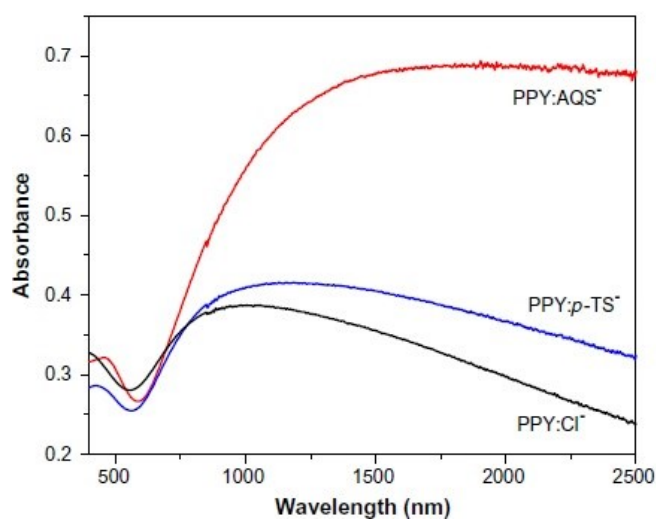
Figure 5. Optical absorption spectra of PPy with different dopant anions.[54]

The structure of the PPy oligomer presented in Figure 2 is idealised. Real PPy chain could have defects like the α-β coupling of monomers and cis-position of amine H of neighbouring monomers, which lead to non-linearity of the chain. Another type of defects, oxygen-containing groups (if the synthesis of PPy was held in water medium) along with hydrogenation of double bond in monomer unit, leads to a loss in conjugation. The defects are presented in Figure 6.
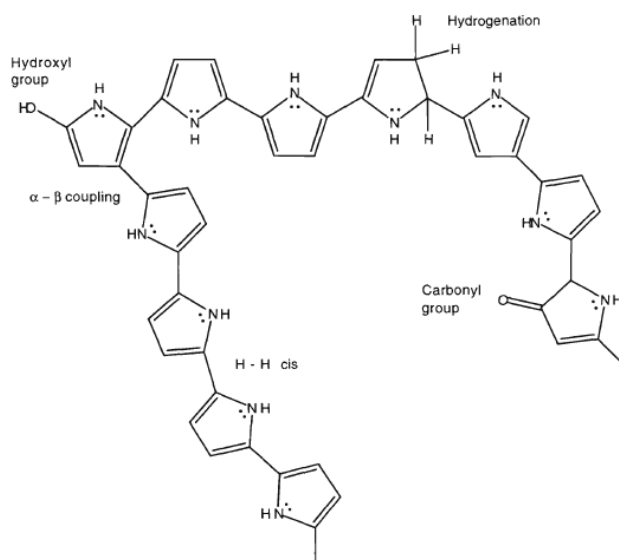
Figure 6. Different defects in PPy chain.[56]

Exclusion of water and oxygen from the solution for polymerisation results in oxygen-free PPy chains. On the other hand, it was found that 1% of the water in polymerisation medium results in high-quality PPy films. Therefore, some optimum in processing should be achieved.

2. Experimental section

2.1 Materials

DNDs were manufactured by Lingyun Granda Nano (China) and distributed by New Metals and Chemicals (Japan). Fourier-transform infrared spectroscopy (FTIR) of as-received DNDs showed pronounced peaks at 2800-3000 cm^{-1} which correspond to C-H surface groups as well as peaks at 1800 cm^{-1} of carbonyl C=O groups. Therefore, further in the text to emphasise the presence of multiple groups on the surface of as-received DNDs, we will refer to them as polyfunctional-DNDs. Zeta potential of polyfunctional-DNDs is positive, + 41 mV (measured by Malvern Zetasizer). Oxidised DND (O-DND) were obtained from polyfunctional-DND by air annealing at 450 ^{0}C for 30 minutes[57]. Zeta potential of such annealed DNDs was -39 mV. Hydrogenated DNDs (H-DNDs) were obtained from O-DNDs by treatment in hydrogen at the atmospheric pressure at 600 ^{0}C for 6 hours. Zeta potential of H-DND is + 40 mV. Hydrochloric acid (HCl, 37%) and pyrrole (98%) were purchased from Sigma-Aldrich (USA) and used as received.

2.2 Sample preparation procedure

To study structural, optical and optoelectronic properties of DNDs/PPy composites, we prepared samples on different substrates: p- and n-type Si, Au, Al, and glass. Substrates were at first nucleated with polyfunctional-DNDs by sonication of the substrate for 15 minutes in polyfunctional-DND water supernatant prepared according to the procedures established in the literature.[57] After that, one of the substrates was annealed in air at 450 ^{0}C for 30 min in order to oxidise the surface of DNDs. Nucleation of Si substrate by H-DND was also performed according to the published procedure.[57] Substrates nucleated with polyfunctional-DND, H-DND and O-DND were immersed into Py solution for 1 hour in the dark and without air conditions. Subsequently, the substrates were immersed into 0.3M HCl solution for 24 hours. Afterwards, the substrates were rinsed with deionised water, dried with the nitrogen and analysed.

2.3 Characterisation techniques

2.3.1 Fourier-transform infrared spectroscopy (FTIR)

FTIR[58] is a technique used to obtain vibrational spectra of solid, liquid or gas samples via absorption of infrared light. During the measurement, the sample is illuminated by broad-band infrared light containing many frequencies of light at once, and it is detected how much of that beam is absorbed by the sample. Next, the beam is

modified to contain a different combination of frequencies, giving a second data point. This process is repeated many times. Afterwards, all this data is being processed by computer backwards using a Fourier transform algorithm to infer what the absorption is at each wavelength.

In this way, the identification of functional groups, their proportion, and their interactions in the compound can be made. For analysis of the composition of the DND/PPy composites, we used grazing angle reflectance Fourier transform infrared (GAR-FTIR) spectroscopy. FTIR spectra were measured using N_2-purged Thermo Nicolet 8700 spectrometer equipped with KBr beam splitter and MCT detector cooled by liquid nitrogen. Au mirrors were chosen as substrates for GAR-FTIR measurements. The optical absorbance was calculated in the standard absorbance units as A = $-\log(R/R_0)$, where R is the spectrum of the analysed material and R_0 is the reference (background) spectrum recorded using clean Au mirror before the analyte application. In all cases, the spectra represent an average of 128 scans recorded with a resolution of 4 cm^{-1}. FTIR spectra were normalized to the intensity of the strongest peak in the spectrum.

2.3.2 Atomic Force Microscopy (AFM)

AFM is a high-resolution type of scanning probe microscopy, which was demonstrated for the first time in 1986 by Binning et al.[59] With AFM, it is possible to measure different forces including mechanical contact force, van der Waals forces, capillary forces, chemical bonding, electrostatic forces, magnetic forces, Casimir forces, solvation forces, etc. AFM consists of a cantilever with a sharp tip (probe) at its end that vibrates at its resonance frequency close to the sample surface. The cantilever is typically silicon or silicon nitride with a tip radius of curvature of the order of nanometers. The laser beam shines on the tip of the cantilever and reflects from it to the photodiode. When the tip is brought into proximity of a sample surface, forces between the tip and the sample change the vibration characteristics (amplitude, frequency) of the tip. This changes the input for the photodiode, which in its turn provides input for the feedback loop. Feedback loop changes the distance between tip and sample so that the amplitude or frequency of tip vibrations is constant. In such a way, a signal for sample imaging is provided. AFM can be operated in a number of modes, depending on the application. In general, possible imaging modes are divided into static (also called contact) modes and a variety of dynamic (non-contact or "tapping") modes where the cantilever oscillates at a given frequency. [59]

Atomic force microscopy (AFM, NTMDT Ntegra) was used in the tapping mode (Si cantilevers with 75 kHz resonance frequency) to characterise the morphology and thickness of the reference poly-DND, H-DND and O-DND nucleated substrates as well as the substrates after the composite formation. Part of the particles on each sample was carefully removed by a thin wood stick. The samples were scanned perpendicular to the interface between the exposed and nucleated part of substrates. Height of the bare substrate was taken as the zero height. Height of each grain on the samples was determined by using a watershed algorithm[60] relative to the exposed substrate. Mean heights of composite and reference DNDs particles were calculated. The PPy layer thickness on DNDs was determined by the formula

$$h_{PPy} = (h_{DND/PPy} - h_{DND}) \pm \sqrt{SD_{DND}^2 + SD_{DND/PPy}^2} \quad (1)$$

where $h_{DND/PPy}$ is average height of DND/PPy composite particles, h_{DND} is average height of pristine DND particles, SD_{DND} is standard deviation (root mean square) of the height values of pristine DND particles, and $SD_{DND/PPy}$ is standard deviation (root mean square) of the height values of DND/PPy composite particles.

2.3.3 Scattering-type near-field optical microscopy-infrared spectroscopy (SNOM-IR)

Nanoscale infrared spectra SNOM-IR were collected by with ca. 20 nm spatial resolution using a scattering-type near-field optical microscope (neaSNOM, neaspec GmbH) equipped with a broadband Difference Frequency Generation (DFG) laser source (Toptica) and an asymmetric Michelson interferometer described elsewhere.[61] PtIr tip with ca. 20 nm diameter was used to probe the sample by operating in tapping mode (tapping amplitude ca. 40nm) at the frequency Ω of ca. 270 kHz, thus modulating the intensity of the scattered IR light at Ω and its higher harmonics. Individual spectra were recorded in ca. 3 minutes each, with a spectral resolution of 8.3 cm^{-1}. Demodulation of the scattered light signal at a higher harmonic $n\Omega$ was used to separate the contribution of the near-field optical signal from that of the background signal.[62] Removal of the instrumental response function from the SNOM-IR spectra was done by normalisation of the measured spectra to a reference Si signal. Resulting SNOM-IR absorption and reflectivity spectra can be directly correlated with the standard far-field IR spectra.[63,64]

2.3.4 Scanning Kelvin Probe (SKP) method

SKP allows determination of a work function (WF) or surface potential (SP) of the sample. Its advantage compared to Kelvin Probe Force microscopy is the possibility of "absolute" dark conditions of measurements as no laser is required for probe position detection in SKP. Bringing together a sample and vibrating electrode (usually in the form of fork or tip) with the known work function, WF tip (e.g. measured independently by XPS) it is possible to define contact potential difference (CPD). Moreover, from equation *CPD = (WF sample – WF tip)/e*, where e is a charge of the electron, the work function of the samples could be found.

SKP was performed with the instrument from KPTechnologies. Scanning of each sample was conducted with a golden tip of 2 mm in diameter at 25 different points. The value of SP for the specified sample at specified conditions (dark/illumination) was taken as the average value of SPs at these 25 points. SP was measured on the same area in the dark and under illumination. As the light source halogen lamp was used with a light intensity of about 200 W/m^2. The reported value of surface photovoltage (SPV) was calculated as *SPV = SP(under illumination) – SP(dark)*.

2.3.5 Photothermal Deflection Spectroscopy (PDS)

PDS is optical spectroscopy that measures the change in refractive index due to the heating of a medium in the vicinity of the sample by light. A probe laser beam is refracted or bent in a manner proportional to the temperature gradient of the transparent medium near the surface. From this deflection, the amount of illumination absorbed by the sample can be determined.

The optical transmittance, reflectance and absorption spectra were measured simultaneously in the broad spectral range from UV to near IR (250–1700 nm). During PDS measurements the samples were immersed into transparent liquid FC72. Absorptance spectra of the samples were normalised via the absorptance spectrum of the highly absorbing black coating.[49] The absorption coefficients at each wavelength were calculated from absorptance spectra of the samples using the formula:

$$Absorption\ coefficient = \frac{-ln(1-Absorptance)}{Sample\ thickness}.$$

The thickness of the PDS samples was evaluated by AFM.

2.3.6 Current-voltage (IV) characterisation

Current-voltage (IV) characteristics were measured by needle probes in a measurement setup using a source-measure unit (Keithley 236). One of the microelectrodes was in contact with a steel carrier disk. The solar cell back electrode was fixed to the steel disk by a gold paste. The other microelectrode is in contact with the solar cell top electrode through a silver paste. The current was measured in the voltage range ± 0.4 V with the sweep rate 50 mV/s. IV curves were measured in the dark and under AM 1.5 solar simulator illumination (light intensity 1000 W/m^2). The characteristic features of the IV curve were determined, namely (1) open-circuit voltage (V_{oc}), the non-zero voltage when there is no current flowing through a solar cell; (2) short-circuit current (I_{sc}), the non-zero current point when there is no external potential applied.[66] Solar-to-electrical power conversion efficiency (η) is another important characteristic of the solar cell. It is calculated as

$$\eta\% = \frac{P_{max} \times 100\%}{P_{incident}},$$

where $P_{incident} = $ *Light intensity x Area under illumination* is the power of incident light and P_{max} is maximum output power of a solar cell which is defined by the maximum product of input voltage and corresponding current. The area under illumination is equal to the area of the top electrode.

The other solar cell performance characteristic is Fill Factor (FF). It represents a competition between charge recombination and extraction by the donor/acceptor from the exciton dissociation interface. [67] FF is calculated as

$$FF = \frac{P_{max}}{V_{oc} \times I_{sc}}.$$

3. Results and discussion

The results of this work were published or submitted to several peer-reviewed journals and conference proceedings. The results show and quantify the optoelectronic effect of nanodiamonds on the conjugated polymer polypyrrole and reveal improved photovoltage in DND/PPy composites and enhanced performance of the solar cell with DND/PPy composite as the active layer compared to the pristine DNDs and PPy. Further details can be found in the enclosed reprints of the journal publications.

The article in Physics Status Solidi A (2016)[68] shows DND/PPy composite formation via GAR-FTIR and it is focused on AFM topography data interpretation. The trend of different polymer thicknesses on DND particles is discussed, the scheme of polymer arrangement relative to the particles is given and a possible explanation of different thicknesses is provided.

The article submitted to the Journal of Materials Chemistry A (2019)[69] elaborates further on chemical bonds formation in DND/PPy different composites and focuses on a comprehensive analysis of optical and optoelectronic properties of the composites, showing their enhancement by optical and electronic effects compared to optoelectronic properties of the pristine PPy or nanodiamonds. The connection between optoelectronic properties and bonding in DND/PPy composites is discussed. Charge transfer mechanism based on experimental and theoretical calculation data is proposed. A test solar cell is fabricated and confirms the nanodiamond role in the facilitation of charge generation from the PPy dye.

The article published in NANOCON2018 Proceedings (2018)[70] addresses the issues of the long-term stability of the electronic properties of the DND/PPy composite. For eight weeks the surface potentials under light and dark were measured and surface photovoltage and its standard deviation were calculated. Surface photovoltage of DND/PPy composite appeared to be the most stable compared to the reference samples and substrate SPVs. Moreover, surface photovoltage of the composite is the positive value while the reference materials and Si substrate have photovoltage of a negative value, which confirms the role of nanodiamond as an electron acceptor.

The supporting article published in Scientific Reports (2016)[71] proposes the technology for size regulation and nucleation procedure of DNDs, which were

important preliminary steps for layer-by-layer synthesis of DND/PPy composite with narrow enough size distribution.

The second supporting article in MRS Advances (2016)[72] investigates the evolution of the size distribution of DNDs depending on annealing temperature and time. The work is related to the previous research,[71] although it is important on its own. For example, for O-DND/PPy composite formation, it was impossible to get dense coverage of O-DND on Si substrate since the particles and the substrate are of the same charge. To obtain dense coverage of O-DND on Si substrate, the substrate was first nucleated with poly-DND and then annealed in the air using the annealing temperature and time obtained reported by Stehlik et al.[71]

The third supporting article is about the factors influencing the stability of the organic solar cells.[73] In particular, it was investigated how the post-treatment of the active material of the solar cell with and without aluminium back-electrode influences its morphology and stability of the optoelectronic properties.

3.1 DND/PPy composite formation and bonding nature in the composites

FTIR, SNOM-IR and AFM measurements were performed to characterise outcomes of the DND/PPy synthesis, namely the structure and composition of the DND/PPy composites and mutual chemical interaction of the components. FTIR spectra of poly-DND/PPy, H-DND and O-DND/PPy as well their references are compared in Figure 7. The spectra indicate the formation of the nanocomposites. The remaining features of pristine DNDs (black arrows) and PPy (red arrows) can be seen in the spectra. At the same time, some of the characteristic vibrations of DNDs are quenched by interaction with PPy. The band of C–H vibrations at 2800–3000 cm^{-1}, is clearly pronounced in the initial H-DNDs and poly-DNDs spectra. It is missing in poly-DND/PPy composite spectrum. It seems to be also missing in H-DND/PPy composite spectrum, yet some C-H vibrations may be hidden in the band of O-H···Cl and N-H···Cl vibrations at 2800–3000 cm^{-1}.[74,75] The peak of carbonyl group, which is present in the reference O-DND spectrum at 1800 cm^{-1} is completely missing in the O-DND/PPy composite spectrum. The regions of 800-1100 and 2250-3770 cm^{-1} (red background) reveal the new features in the DNDs/PPy composite compared to the pristine components. Moreover, the difference between the composites spectra in these regions suggests the different type of interaction between PPy

and DND of different surface terminations. The peak at 1034 cm^{-1} of poly-DND/PPy composite has a distinct shoulder at 970 cm^{-1}, which is absent in the PPy reference spectrum. This feature is attributed to C-C out-of-plane deformations of PPy ring.[76,77]
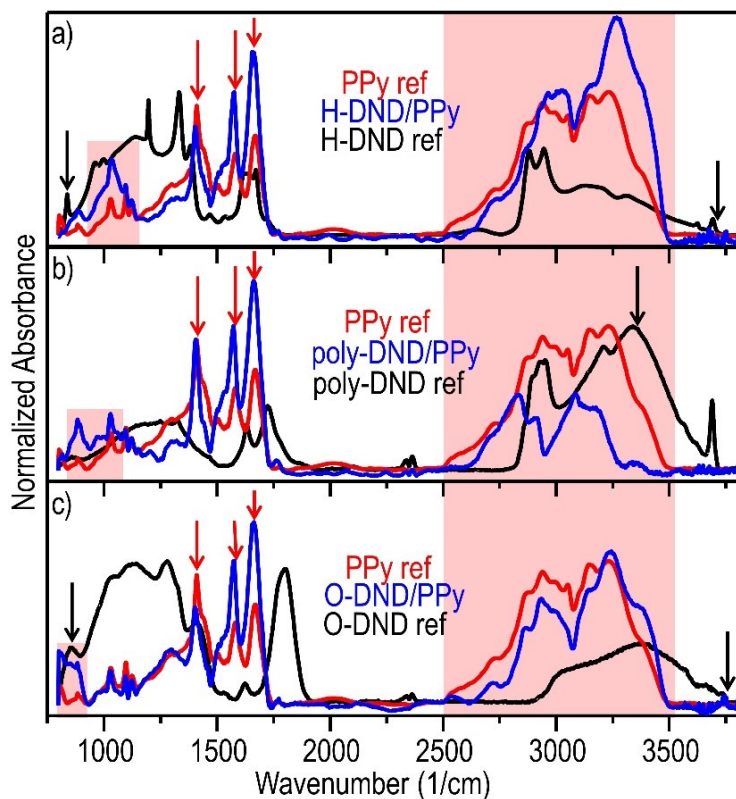

Figure 7. FTIR spectra of polyfunctional-DND/PPy and O-DND/PPy composites are compared to the reference DNDs and PPy spectra

In H-DND/PPy, the shape of 1034 cm^{-1} peak differs from the one of PPy reference, it is broadened and with the shoulder of C-C out of plane vibrations as in poly-DND/PPy. In O-DND/PPy, the region in 800-930 cm^{-1} seem to be a superposition of DND (850 cm^{-1} peak can be attributed to C-Cl in diamond particle[78] and thus it indicates possible partial chlorination of O-DND surface after interaction with HCl solution) and PPy vibrations (880 cm^{-1} peak can be attributed to C-H out of PPy ring plane deformations[76]).

The range in 2250-3770 cm^{-1} represents a complex mixture of OH, NH and O-H···Cl and N-H···Cl vibrations.[74,78,79] There is a noticeable redshift of the poly-DND/PPy bands in 2250-3770 cm^{-1} region compared to other composites and PPy ref. The shape of poly-DND/PPy spectrum in this region differs from the

spectrum shape of the other materials. It might be due to the largest amount of O-H bonds on the poly-DND surface compared to H-DND and O-DND (carbonyl and carboxyl groups dominate in O-DNDs) particles. Thus, O-H···Cl dominates in poly-DND/PPy in the 2250-3770 cm^{-1} region while spectra of the other composites in this range are dominated by N-H···Cl or NH vibrations and they are blueshifted.

FTIR, measuring the averaged signal from the sample, does not enable us to distinguish between the signal from PPy on the particles and PPy on the substrate of the same sample. To overcome this limitation of FTIR and further elucidate the differences in the composites structure, we performed SNOM-IR spectroscopy with a nanoscale resolution.

In Figure 8, SNOM-IR spectra of poly-DND/PPy, O-DND/PPy and PPy reference are presented. Topography images of the samples (by AFM) are shown as well. The spectra of given colour correspond to the place on the topography image marked by the rectangle of the same colour.

Figure 8a shows PPy reference spectra at 5 different locations on the substrate, including both plains and hillocks, which all match well with each other. Figure 8b shows the spectra of PPy on O-DND particles (orange line) and their surroundings (blue line). Several spectra taken on O-DND/PPy particles match with each other and reveal distinct peak at 1408 cm^{-1} not found in the spectra of the surroundings. Figure 8c shows spectra taken on the poly-DND/PPy particles (red lines) and on the substrate (blue line). The spectra are well reproducible. Spectra taken on the substrate differ from the ones on poly-DND/PPy particles by the more pronounced intensity of the peak at 1671cm^{-1}, while in the rest of the spectral region the spectra match well.

The new peak at 1408 cm^{-1} in O-DND/PPy compared to PPy reference can be attributed to C-N vibrations which became asymmetrical (due to electrostatic interactions of O-DND and PPy) and subsequently visible in SNOM-IR spectrum. The peak at 1671 cm^{-1} presented in all SNOM-IR spectra is most likely attributed to N-H vibrations. The intensity of the peak does not depend on the thickness of PPy layer (spectra on PPy references taken on PPy micron-size agglomerate and PPy thin film of about 20 nm thickness are comparable, see Figure 8a). Interaction of PPy with O-DND does not influence 1671 cm^{-1} peak intensity since it can be of the same electrostatic nature as the interaction between PPy and silicon (with native silicon oxide) substrate. Thus, the difference in 1671 cm^{-1} peak intensity in poly-DND/PPy composite suggests different bonding nature with a different arrangement of PPy on Si substrate (e.g., PPy

overlaying the substrate) and on the poly-DND particle (e.g., upright alignment of PPy chain relatively to poly-DND[68]). In this way, differently aligned PPy will interact in a different way with SNOM-IR polarised light resulting in different peak intensities.
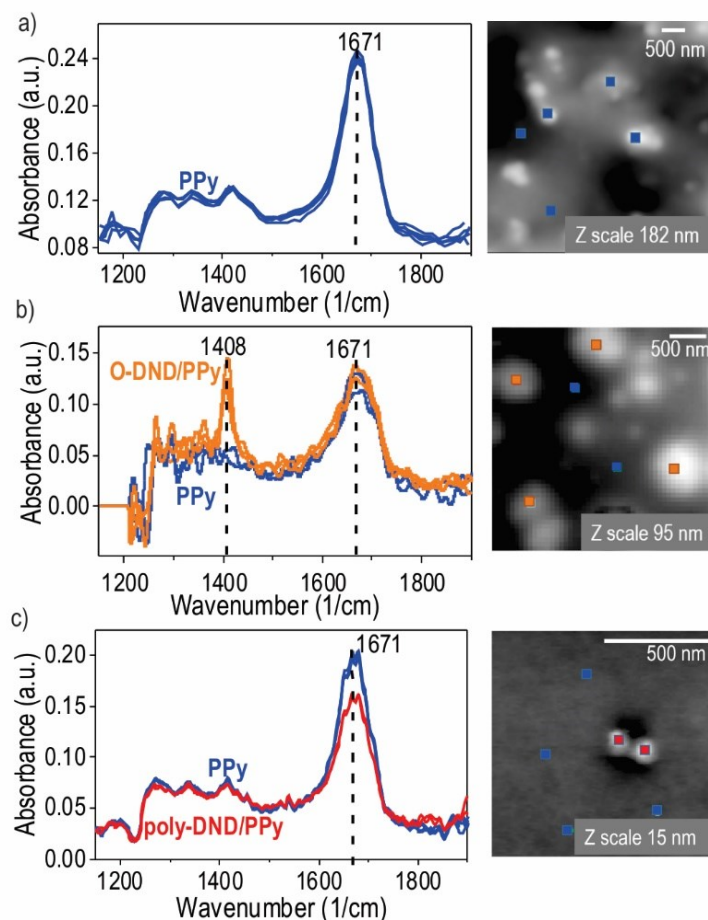

Figure 8. AFM maps with indicated locations of SNOM-IR spectra of a) PPy reference b) O-DND/PPy c) poly-DND/PPy. The lateral size of the particles' and PPy agglomerates could be deduced from the scale bars on AFM images. Characteristic PPy peaks at 1671 (N-H vibration) and 1408 (C-N vibration) cm^{-1} are indicated at SNOM-IR spectra.

The possibility of revealing the arrangement of the molecules by the different intensity of SNOM-IR response signal was already shown by Amenabar I. et al.[80] and is revealed again in this work. Thus, SNOM-IR clearly shows tight interaction between DNDs and PPy confirming O-DND/PPy and poly-DND/PPy composites formation. Also based on SNOM-IR results, different types of bonding with subsequent different PPy arrangement relatively to O-DND and poly-DND can be suggested.

Results of AFM measurements corroborate FTIR and SNOM-IR conclusions. Figure 9 shows representative topography images obtained by AFM. Planar images show particles distribution and height enlargement. 3D images visualise overall size enlargement after processing of the DNDs with Py.
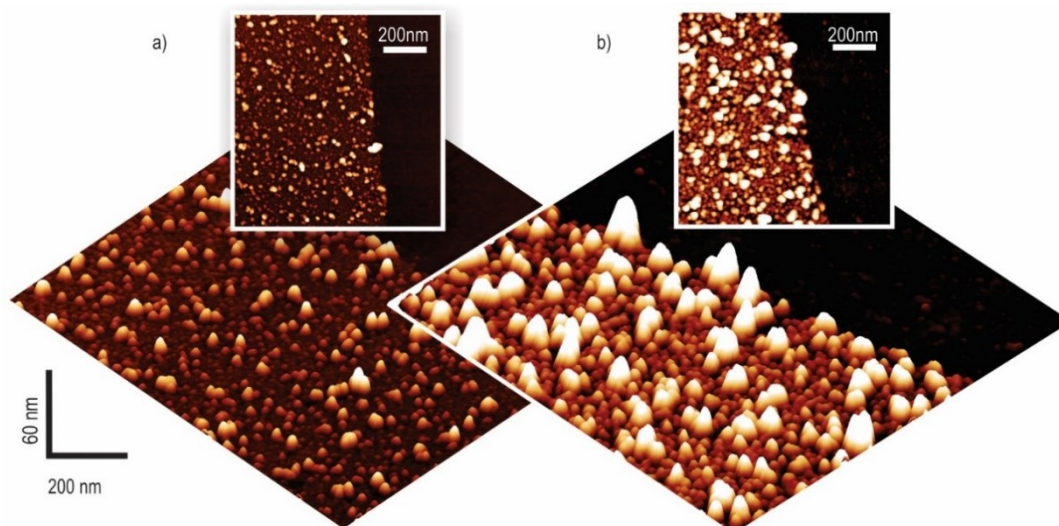

Figure 9. AFM 2D and 3D topography images of a) H-DND ref and b) H-DND/PPy.

As can be seen from the AFM images, already reference DND particles (Figure 9a) form aggregates of different sizes on the substrate. To understand how surface chemistry influences DNDs interaction with the PPy dye we processed AFM scans and selected the sizes that correspond to primary particles (for poly-DND and O-DND it is 4.5-5.0 nm and for H-DND it is 3 nm) or 2-particle aggregates. Larger aggregates introduce uncertainties in the PPy thickness interpretation due to e.g. different surface chemistry of aggregates compared to the primary particles. Evaluated mean particle sizes are summarized in Table 1. Mean sizes of poly-DND (4.8 ± 0.2 nm) and O-DND (5.1 ± 0.4 nm) are similar. This confirms that the annealing does not reduce the particle size but modifies the surface groups only. H-DND mean size is somewhat smaller, 2.9 ± 0.1 nm, as a result of the hydrogenation process.[81]

After pyrrole was polymerized on DNDs, there is an enlargement in DND particles height, which can be seen from Figure 9b. After processing AFM scans the mean height of DNDs/PPy particles was defined and PPy thickness was calculated using equation (1). The results are summarized in Table 1. The thickness of PPy is dependent on particle initial surface chemistry. The thickest PPy layer is formed on

poly-DND (4.2 ± 0.4 nm), and the minimum PPy thickness is observed on O-DND (1.4 ± 0.7 nm). PPy layer on H-DND (3.8 ± 0.1 nm) is of similar thickness as on poly-DND. PPy thicknesses on O-DND and poly-DND appeared to be smaller than estimated in our previous work.[68] This might be due to the more accurate particle height evaluation procedure in this work by grain analysis using the watershed method compared to the particle height estimation via roughness analysis.[68] However, different particle height evaluation methods lead to the same trend in PPy thickness, which is maximum on poly-DND and 2 - 3 times less on O-DND.

Sample name	Mean Particle Height, nm	PPy thickness, nm
poly-DND	4.8 ± 0.2	4.2 ± 0.4
poly-DND/PPy	9.0 ± 0.3	
H-DND	2.9 ± 0.1	3.8 ± 0.1
H-DND/PPy	6.7 ± 0.1	
O-DND	5.1 ± 0.4	1.4 ± 0.7
O-DND/PPy	6.5 ± 0.6	

Table 1. Mean height of DND particles and the composites established from AFM topography data and calculated PPy thicknesses.

Considering the same Py polymerisation conditions for all types of DND particles different PPy thickness on poly-, H- and O-DND can be explained by the different PPy chains arrangement relative to the different types of DNDs, namely the upright position of PPy chains relative to poly-DND and H-DND and PPy chains overlaying O-DND particle. The proposed arrangement of PPy relatively to DNDs is presented in Figure 10. The scheme takes into account similar roughness of DND nucleated samples before and after PPy processing[68].
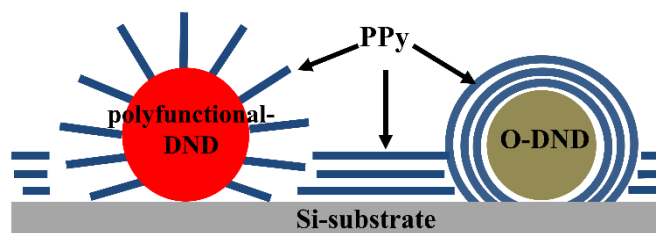

Figure 10. The scheme of PPy binding to polyfunctional-DND, O-DND and the Si substrate.

After the clarification of the chemical structure and morphology of the composites, we investigated their optoelectronic properties and applicability in photovoltaics.

3.2 Optoelectronic properties of DND/PPy composites

Optical absorption of the composites was estimated by PDS technique. PDS spectra of neat PPy, as well as DND/PPy composites, reveal optical absorption in a broad visible spectral range (see Figure 11a). Picture of a sample during PDS measurement is shown in Figure 11b.
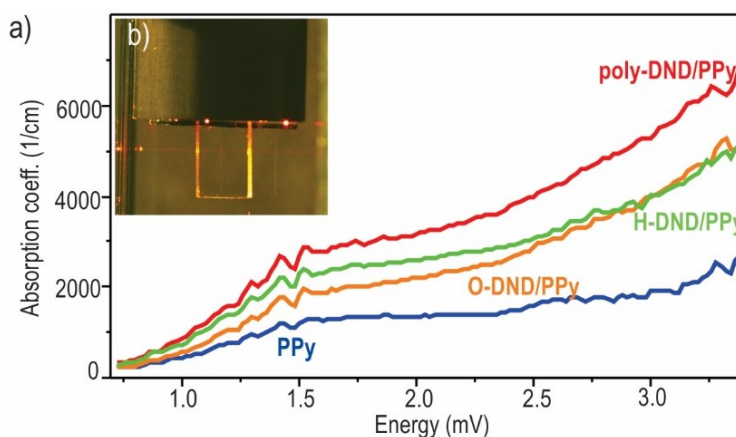

Figure 11. a) Absorption coefficient spectra of composites and PPy reference b) poly-DND/PPy sample during PDS measurement.

Poly-DND/PPy composite absorbs the most while neat PPy absorbs the least. O-DND/PPy and H-DND/PPy composites have an absorption coefficient similar to each other and both are well below the absorption coefficient of poly-DND/PPy composite. Although superior optical absorption of poly-DND/PPy composite seems obvious; various factors should be considered before making such a conclusion.

DND particles carry a larger amount of light-absorbing dye since PPy thickness on glass substrates nucleated with DNDs of any kind is higher compared to PPy thickness on the bare glass substrate (see Table 1 and Figure 12). Even though the absorption coefficient is independent of material thickness, the actual amount of PPy can be different in the given thickness. However, PPy thickness on O-DND is smaller than in the neat PPy layer, and yet the O-DND/PPy has a larger absorption coefficient in the whole spectrum. There is also different PPy thickness on H-DND and O-DND, and yet the absorption coefficient spectra are similar. Contrary, the PPy thickness on H-DND and poly-DND is similar, and yet the absorption coefficient differs considerably. The pronounced difference in absorption cannot be only due to scattering effects though, as observed for instance, for Si quantum dots.[82] Otherwise, poly-DND/PPy and O-DND/PPy absorption would be similar due to similar DND density of these samples.
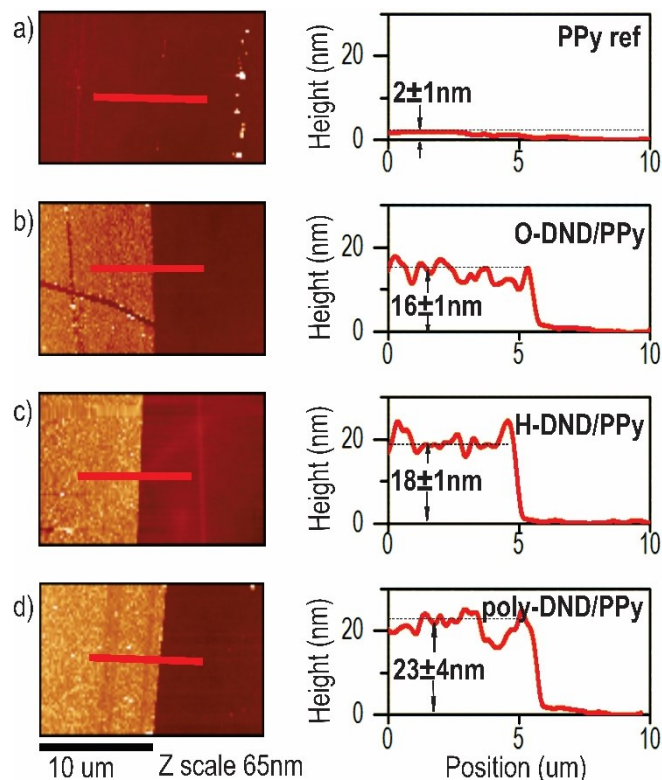
Figure 12. AFM images of the samples on the border with an exposed bare glass substrate and corresponding height cross-sections of a) PPy reference b) O-DND/PPy c) H-DND/PPy d) poly-DND/PPy.

Another factor of the different absorption coefficients of the composites and PPy ref can be different electronic states of PPy itself. Although the synthesis process (and chemicals) was the same for all samples, the PPy could be different due to DND surface effects on the synthesis. Two additional energy levels are introduced into PPy bandgap at mild PPy oxidation, which corresponds to bonding and anti-bonding polaron states.[83,84] With a large extent of PPy oxidation, the quantity of intra-bandgap levels increases, and they merge into bands (bipolaron bonding and anti-bonding bands). As a result, PPy oxidation promotes absorption in the infrared region and broadening of the bands in the absorption spectrum due to more possibilities of charge transfer between intra-bandgap bands. Thus, more pronounced absorption in composites compared to pristine PPy can be explained by the larger extent of PPy oxidation in composites due to charge exchange between PPy and DNDs. Poly-DND/PPy with maximum absorption compared to O-DND/PPy and H-DND/PPy might be consisted of PPy in the largest oxidation state due to the most pronounced charge exchange between poly-DND and PPy.

The last but not least factor behind the enhanced absorption coefficient of the nanocomposites may be the favourable optoelectronic properties arising at the DND/PPy junction. Theoretical computing[85,86] (described further below) indicated large variations of energetic bandgap (0.3 - 3.5 eV) at the junction of DND/PPy depending on facet crystallographic orientation, surface chemistry and way of PPy attachment. In our opinion, it is probably the dominating effect behind the enhanced absorption coefficient as it is well correlated with photovoltage measurements by SKP.

The photograph of the SKP setup is shown in Figure 13a. Each sample was contacted sideways by a ball-shaped electrode. SKP probing tip is above the sample. Illumination, when it is necessary, is introduced under an angle from the side.
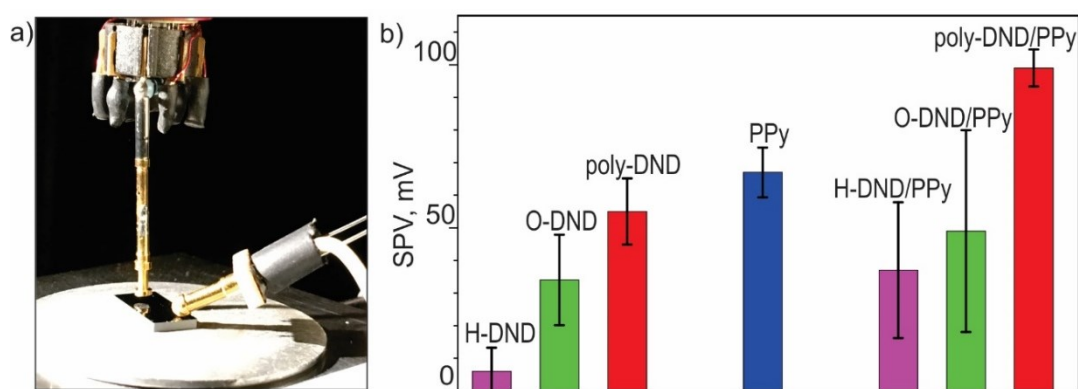

Figure 13. a) Photo of the SKP measurement setup b) SPV of the composites and their references.

Surface potentials of poly-DND/PPy, O-DND/PPy and H-DND/PPy composites, their references and bare substrates were measured in the dark and under illumination. Surface photovoltages of the samples were then calculated. The highest SPV of the DND/PPy composites was detected on the samples with the p-Si substrate. The SPV values for the reference and composite samples are summarized in Figure 13b. Maximum photovoltage is observed on poly-DND/PPy composite (99±6 mV) compared to O-DND/PPy (49±31 mV) and H-DND/PPy (37 ± 21 mV). SPV of poly-DND/PPy is also larger compared to SPV of pristine PPy (67±8 mV) and pristine poly-DNDs (55±10 mV). H-DND reference sample shows negligible SPV (6±7 mV), and O-DND reference has SPV values of 34±14 mV. The difference between H-DND and O-DND may be explained by cleaning of sp^2 components and by passivation of surface states during hydrogenation annealing. The largest positive surface photovoltage detected in poly-DND/PPy compared to all other samples might indicate the largest

extent of PPy oxidation by poly-DNDs via withdrawing electrons from PPy chain (in agreement with PDS interpretation above). Noteworthy, SPV of the composites cannot be due to the substrate, because the annealed p-Si has SPV of the opposite sign (-87±31 mV) compared to the nanocomposites and other reference samples.

Theoretical calculations[85,86] support the experimental results and help us propose a photovoltage generation mechanism in the DND/PPy composites. In the model configuration of poly-DND/PPy composites, where PPy chain grafted covalently to DND and surrounded by oxygen-containing groups, it was observed that HOMO is fully localised on PPy and LUMO fully localised on DND (Figure 14a), that indicates favourable conditions for electron extraction from PPy to poly-DND upon extra energy intake, for example, from the illumination.
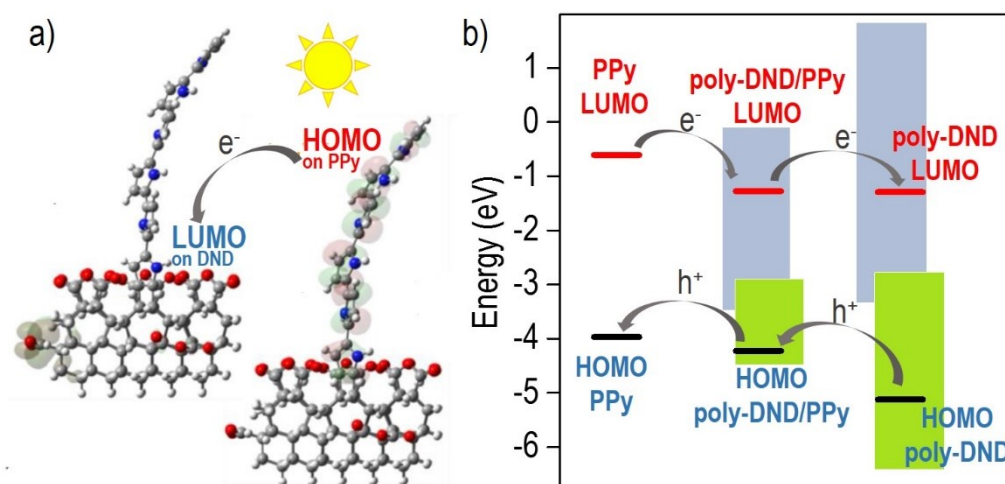
Figure 14. a) Example of spatial separation of PPy HOMO and DND LUMO. Based on DFT calculations. b) Scheme of HOMO and LUMO energetic levels composite of separate materials and their interface with the most probable charge transfer due to level alignment.

In addition, for various oxygen moieties in the poly-DND/PPy models, the energetic levels of PPy, DND and DND-PPy interface are aligned in such a way that it is energetically beneficial[30,87] for the electrons to be transferred from PPy into DND (Figure 14b). Thus, the maximum and positive SPV observed in the poly-DND/PPy composite is theoretically explained. The calculations also elucidate the role of hydrogen- and oxygen-containing groups on poly-DND surface, namely PPy grafts via CH groups to poly-DND and hydrogen-bond interaction of the grafted PPy with surrounding CO groups results in the alignment of energy levels of PPy and poly-DND

and in the spatial separation of HOMO on PPy and LUMO on poly-DND that favours charge carriers separation between PPy and poly-DND.

Poly-DND/PPy as the nanocomposite with the most enhanced absorption coefficient and the highest SPV among all the samples was embedded as an active material into a simple solar cell structure with p-Si as the back electrode and Al as the top electrode. Figure 15a shows IV characteristic curves in the dark and under the illumination of such a solar cell. The inset image (Figure 15b) shows how the IV characteristics of the solar cell with poly-DND/PPy were measured. The characteristics show that the solar cell is indeed functional.

Figure 15. a) IV curves in the dark (black) and under solar simulator irradiation (red) of a solar cell with poly-DND/PPy composite as an active material b) Test solar cell picture with connected microelectrodes for IV characterisation.

The open-circuit voltage V_{oc} is 0.05V and the short circuit current I_{sc} is 0.6 uA/cm^2. The calculated fill factor of the solar cell is 0.3 and power conversion efficiency η reaches 1E-5%. They may seem quite low, but it noteworthy the device was not optimised. Nevertheless, the performance of solar cell with the poly-DND/PPy composite as an active material is better than with the neat PPy layer which has two times lower efficiency (see Figure 16).
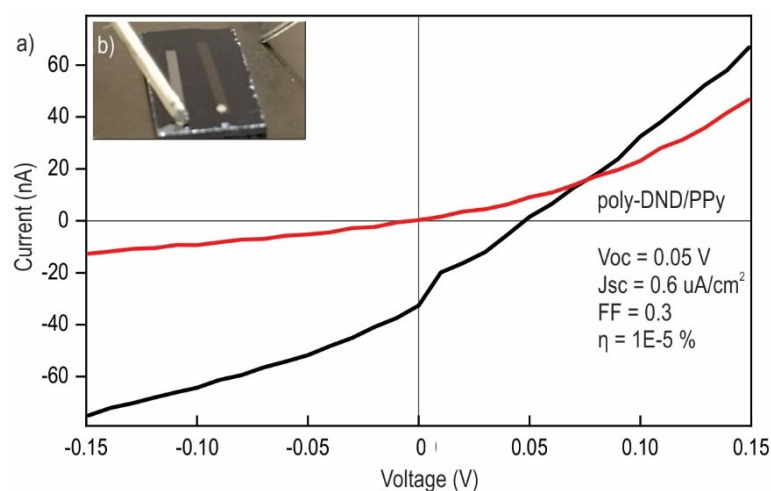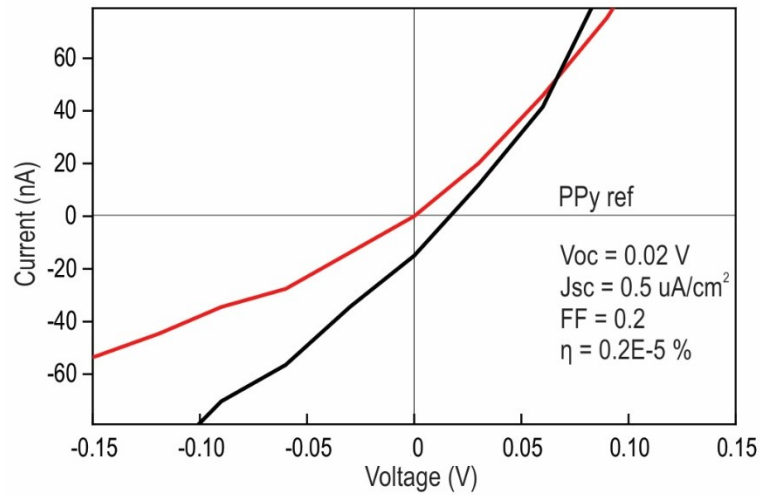
Figure 16. IV curves in the dark (black) and under solar simulator irradiation (red) of a solar cell with PPy reference as an active material.

Thus, the prototype solar cell with poly-DND/PPy composite demonstrates proof-of-principle as well as provides opportunities for further optimisations (by variation of materials for the top/back electrode, finding the optimum thickness of the nanocomposite, interface optimisation, etc).

3.3 Stability of DND/PPy composites

Figure 17 shows the results of surface potential measurements in the short-term. All surface potentials are stable (within 6 mV of standard deviation) and regularly reproducible during light switching in each measurement. Thus, the whole surface potential measurement data in the dark and under illumination were averaged for each material. The averaged surface potentials with standard deviation in dark and under illumination were: pSi (-101 ± 6 mV and -272 ± 5 mV), PPy (-189 ± 3 mV and -311 ± 5 mV), poly-DND (-34 ± 4 mV and -230 ± 6 mV), and poly-DND/PPy composite (-202 ± 4 mV and -69 ± 3 mV).
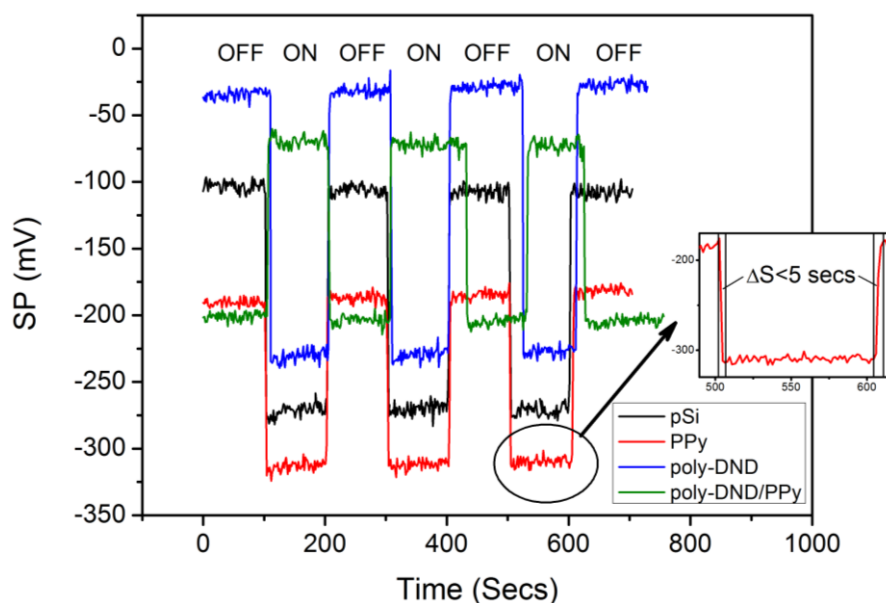
Figure 17. The surface potential of pSi, PPy, poly-DND, poly-DND/PPy as a function of time and visible light illumination in the short-term (0 – 12 min). The potential profiles correspond to measurements after seven weeks. The inset shows the rise and fall edge when the illumination changes.

Then the short-term measurements were repeated every week for eight subsequent weeks to investigate the long-term stability. The shape of the short-term profiles with the fast rise and fall edges was the same for the whole eight weeks. Thus, we averaged Kelvin Probe data in the dark and under illumination each week. The averaged potential in the dark and under illumination is plotted in Figure 18. The standard deviation of the average value is used as the error bar. From Figure 18 it is seen that in the long-term (for eight weeks), the potentials in the dark and under illumination are slowly fluctuating. The potential fluctuations are qualitatively very similar for all the studied materials, hence they are most likely related to some external factors.
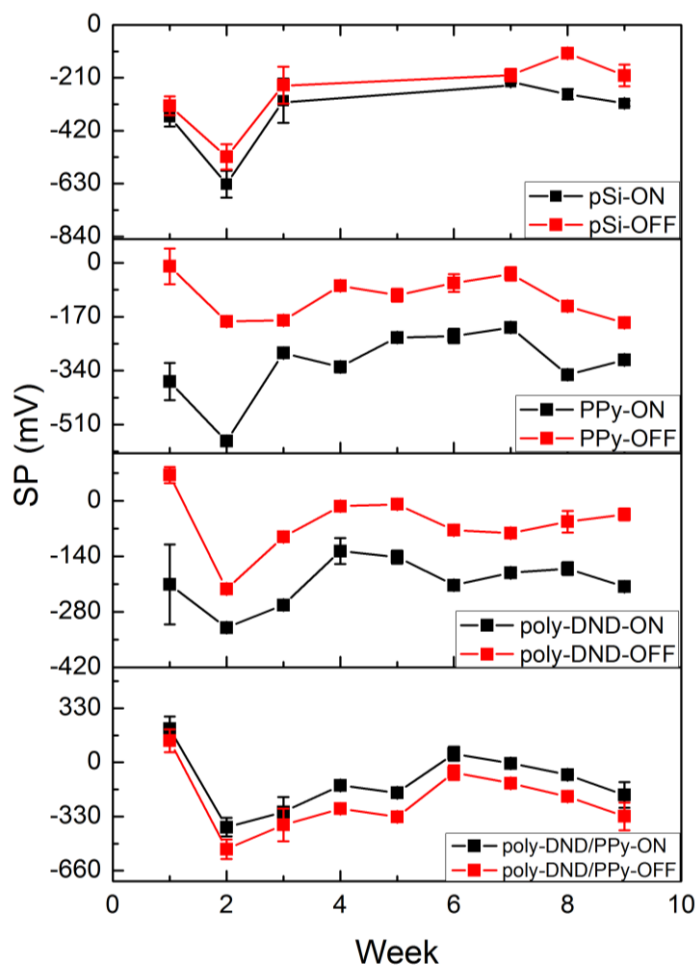
Figure 18. The average value of surface potential in the dark and under illumination plotted as a function of time for the long-term stability evaluation.

The surface potentials exhibit similar fluctuation in dark and under illumination. Evaluation of surface photovoltage was thus used to observe actual material (in)stability despite the overall potential fluctuations. Figure 19a presents surface photovoltage (SPV) at each of eight weeks.

SPV exhibits the most pronounced changes for the first three weeks (an area I), then for the remaining six weeks, it seems to fluctuate around a stabilised value (area II). To characterise this (in)stability, we calculated average SPV and its standard deviation in each area (values at the boundary were accounted for in both areas). The averaged SPV values with standard deviation in the area I and area II are: pSi (-85 ± 33 mV and -91 ± 59mV), PPy (-281 ± 155 mV and -166 ± 55 mV), poly-DND (-182 ± 90 mV and -137 ± 30 mV), and poly-DND/PPy (95 ± 33 mV and 124 ± 22 mV). Different

values of surface photovoltage for the reference PPy and poly-DND reported in our different works[70,69] can be due to the different time point of SPs measurement, and thus, SPV values reported in [69] were taken more than eight weeks after sample preparation. Noteworthy, SPV of the composite is very similar in both works that highlight its stability.

Figure 19b shows in the form of a bar graph the standard deviation as a measure of SPV (in)stability. We can see the standard deviation difference of the averaged SPV between area I and area II on pSi (33 mV and 59 mV), PPy (155 mV and 55 mV), poly-DND (90 mV and 30 mV), and poly-DND/PPy (33 mV and 22 mV). The minimum standard deviation is observed on poly-DND/PPy composite for the whole eight weeks.
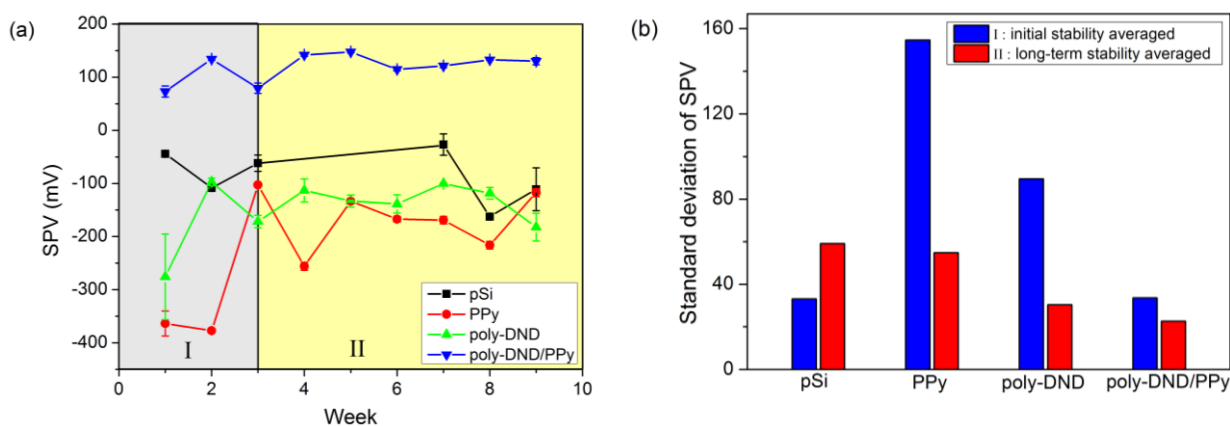
Figure 19. (a) Surface photovoltage (SPV) of all the materials for eight weeks. The area I is defined as initial stability and area II as long-term stability. (b) The standard deviation of the averaged SPV value.

Thus, the SPV of the poly-DND/PPy composite was the most stable from the very beginning after fabrication until the last measurement after eight weeks. The material interaction in poly-DND/PPy composites thus contributes to photovoltage stability. Note in this respect that surface photovoltage of poly-DND/PPy composite has the opposite (positive) sign compared to the SP of pSi, PPy and poly-DND. Such positive charging of the DND/PPy composite surface, i.e. polypyrrole, is in agreement with the theoretical atomic-scale calculations[83] and indicates the role of nanodiamonds as electron acceptors. This effect, together with polypyrrole tight binding to nanodiamond shown previously, may explain the improved stability of the composite.

Conclusions

The present work showed that detonation nanodiamonds with various surface chemical groups can be combined with polypyrrole into the novel nanocomposite material. We demonstrated a layer-by-layer fabrication technology that is well-scalable and inexpensive. Formation of the nanocomposite and pronounced interaction between polypyrrole and nanodiamond in such composite were evidenced by changes and new vibrational bands in infrared spectroscopy performed both macroscopically and locally with nanoscale resolution and supported by atomic force microscopy.

Moreover, AFM indicated that DNDs with different surface chemical groups assemble PPy oligomers in different ways: PPy chains are aligned uprightly relative to poly-DND and H-DND surfaces due to assumed covalent bond in poly-DND/PPy and H-DND/PPy; while PPy overlays the surface of O-DND due to physisorption of PPy on O-DND surface. Different PPy arrangements relative to the DNDs contributed to the different optoelectronic effects of the composites. Study of the optical absorption and photovoltage generation revealed that all DND/PPy composites exhibit a highly enhanced absorption coefficient compared to the pristine PPy and DNDs. The optical absorption of the composites is broad, covering well the visible spectrum from infrared to near UV (from 1 eV to 3.5 eV). The most pronounced absorption coefficient was observed in poly-DND/PPy compared to O-DND/PPy and H-DND/PPy. Also, the surface photovoltage in PPy grafted to poly-DND was doubled compared to the pristine PPy. The positive polarity of SPV in DND/PPy composites shows that DND acts as an electron acceptor and leaves the positive charge on PPy molecules. This fact is confirmed by the theoretical atomic-scale DFT calculations.

Noteworthy, poly-DND/PPy exhibits long-term stability of the optoelectronic properties. For eight weeks the surface potential of the composite under illumination and in the dark remained almost constant, and surface photovoltage possessed the least deviations compared to the pristine reference materials and the substrate. Thus, polyfunctional nanodiamond with both oxygen and hydrogen surface groups appeared the most favourable for photovoltaics. The assembled prototype solar cell with poly-DND/PPy as an active material proved the functionality of the concept. Due to the general non-toxicity of nanodiamond, its chemical stability and availability in large quantities, these results may open prospects for a breakthrough in the field of organic photovoltaics.

34

References

1. Hayat M. B., Ali D., Monyake K. C., Alagha L. & Ahmed N. Solar energy—A look into power generation, challenges, and a solar-powered future. *Int. J. Energy Res.* **43**, 1049–1067 (2019).

2. Lee J., Lee S. M., Chen S., Kumari T., Kang S.-H., Cho Y. & Yang C. Organic Photovoltaics with Multiple Donor–Acceptor Pairs. *Adv. Mater.* **31**, 1804762 (2019).

3. Fan B., Zhang D., Li M., Zhong W., Zeng Z., Ying L., Huang F. & Cao Y. Achieving over 16% efficiency for single-junction organic solar cells. *Sci. China Chem.* **62**, 746–752 (2019).

4. Cui Y., Yao H., Zhang J., Zhang T., Wang Y., Hong L., Xian K., Xu B., Zhang S., Peng J., Wei Z., Gao F. & Hou J. Over 16% efficiency organic photovoltaic cells enabled by a chlorinated acceptor with increased open-circuit voltages. *Nat. Commun.* **10**, 2515 (2019).

5. Zhang S., Qin Y., Zhu J. & Hou J. Over 14% Efficiency in Polymer Solar Cells Enabled by a Chlorinated Polymer Donor. *Adv. Mater. Deerfield Beach Fla* **30**, e1800868 (2018).

6. Cui Y., Yao H., Hong L., Zhang T., Xu Y., Xian K., Gao B., Qin J., Zhang J., Wei Z. & Hou J. Achieving Over 15% Efficiency in Organic Photovoltaic Cells via Copolymer Design. *Adv. Mater. Deerfield Beach Fla* **31**, e1808356 (2019).

7. Meng L., Zhang Y., Wan X., Li C., Zhang X., Wang Y., Ke X., Xiao Z., Ding L., Xia R., Yip H.-L., Cao Y. & Chen Y. Organic and solution-processed tandem solar cells with 17.3% efficiency. *Science* **361**, 1094–1098 (2018).

8.   Li N., McCulloch I. & Brabec C. J. Analyzing the efficiency, stability and cost potential for fullerene-free organic photovoltaics in one figure of merit. *Energy Environ. Sci.* **11**, 1355–1361 (2018).

9.   Speller E. M., Clarke A. J., Luke J., Lee H. K. H., Durrant J. R., Li N., Wang T., Wong H. C., Kim J.-S., Tsoi W. C. & Li Z. From fullerene acceptors to non-fullerene acceptors: prospects and challenges in the stability of organic solar cells. *J. Mater. Chem. A* 10.1039.C9TA05235F (2019). doi:10.1039/C9TA05235F

10. Dimroth F., Grave M., Beutel P., Fiedeler U., Karcher C., Tibbits T. N. D., Oliva E., Siefer G., Schachtner M., Wekkeli A., Bett A. W., Krause R., Piccin M., Blanc N., Drazek C., Guiot E., Ghyselen B., Salvetat T., Tauzin A., Signamarcheix T., Dobrich A., Hannappel T. & Schwarzburg K. Wafer bonded four-junction GaInP/GaAs//GaInAsP/GaInAs concentrator solar cells with 44.7% efficiency. *Prog. Photovolt. Res. Appl.* **22**, 277–282 (2014).

11. Yoshikawa K., Kawasaki H., Yoshida W., Irie T., Konishi K., Nakano K., Uto T., Adachi D., Kanematsu M., Uzu H. & Yamamoto K. Silicon heterojunction solar cell with interdigitated back contacts for a photoconversion efficiency over 26%. *Nat. Energy* **2**, 17032 (2017).

12. Uzu H., Ichikawa M., Hino M., Nakano K., Meguro T., Hernández J. L., Kim H.-S., Park N.-G. & Yamamoto K. High efficiency solar cells combining a perovskite and a silicon heterojunction solar cells via an optical splitting system. *Appl. Phys. Lett.* **106**, 013506 (2015).

13. Akaike K. & Kubozono Y. Correlation between energy level alignment and device performance in planar heterojunction organic photovoltaics. *Org. Electron.* **14**, 1–7 (2013).

14. Yu G., Gao J., Hummelen J. C., Wudl F. & Heeger A. J. Polymer Photovoltaic Cells: Enhanced Efficiencies via a Network of Internal Donor-Acceptor Heterojunctions. *Science* **270**, 1789–1791 (1995).

15. Rezek B., Čermák J., Kromka A., Ledinskỳ M., Hubík P., Mareš J. J., Purkrt A., Cimrová V., Fejfar A. & Kočka J. Synthesis, structure, and opto-electronic properties of organic-based nanoscale heterojunctions. *Nanoscale Res. Lett.* **6**, 238 (2011).

16. Brandão L., Viana J., Bucknall D. G. & Bernardo G. Solventless processing of conjugated polymers—A review. *Synth. Met.* **197**, 23–33 (2014).

17. Dhanabalan A., van Duren J. K. J., van Hal P. A., van Dongen J. L. J. & Janssen R. a. J. Synthesis and Characterization of a Low Bandgap Conjugated Polymer for Bulk Heterojunction Photovoltaic Cells. *Adv. Funct. Mater.* **11**, 255–262 (2001).

18. Price S. C., Stuart A. C., Yang L., Zhou H. & You W. Fluorine Substituted Conjugated Polymer of Medium Band Gap Yields 7% Efficiency in Polymer–Fullerene Solar Cells. *J. Am. Chem. Soc.* **133**, 4625–4631 (2011).

19. Brabec C. J., Padinger F., Hummelen J. C., Janssen R. A. J. & Sariciftci N. S. Realization of large area flexible fullerene — conjugated polymer photocells: A route to plastic solar cells. *Synth. Met.* **102**, 861–864 (1999).

20. Gao Y., Liu M., Zhang Y., Liu Z., Yang Y. & Zhao L. Recent Development on Narrow Bandgap Conjugated Polymers for Polymer Solar Cells. *Polymers* **9**, 39 (2017).

21. Berger P. R. & Kim M. Polymer solar cells: P3HT:PCBM and beyond. *J. Renew. Sustain. Energy* **10**, 013508 (2018).

22. Jin Y., Chen Z., Dong S., Zheng N., Ying L., Jiang X.-F., Liu F., Huang F. & Cao Y. A Novel Naphtho[1,2-c:5,6-c']Bis([1,2,5]Thiadiazole)-Based Narrow-Bandgap π-

Conjugated Polymer with Power Conversion Efficiency Over 10. *Adv. Mater. Deerfield Beach Fla* **28**, 9811–9818 (2016).

23. Lukina E. A., Popov A. A., Uvarov M. N., Suturina E. A., Reijerse E. J. & Kulik L. V. Light-induced charge separation in a P3HT/PC70BM composite as studied by out-of-phase electron spin echo spectroscopy. *Phys. Chem. Chem. Phys.* **18**, 28585–28593 (2016).

24. Dang M. T., Hirsch L. & Wantz G. P3HT:PCBM, Best Seller in Polymer Photovoltaic Research. *Adv. Mater.* **23**, 3597–3602 (2011).

25. Guo X., Cui C., Zhang M., Huo L., Huang Y., Hou J. & Li Y. High efficiency polymer solar cells based on poly(3-hexylthiophene)/indene-C70 bisadduct with solvent additive. *Energy Environ. Sci.* **5**, 7943–7949 (2012).

26. Holliday S., Ashraf R. S., Wadsworth A., Baran D., Yousaf S. A., Nielsen C. B., Tan C.-H., Dimitrov S. D., Shang Z., Gasparini N., Alamoudi M., Laquai F., Brabec C. J., Salleo A., Durrant J. R. & McCulloch I. High-efficiency and air-stable P3HT-based polymer solar cells with a new non-fullerene acceptor. *Nat. Commun.* **7**, 11585 (2016).

27. Liu D., Zhang K., Zhong Y., Gu C., Li Y. & Yang R. An effective strategy for controlling the morphology of high-performance non-fullerene polymer solar cells without post-treatment: employing bare rigid aryl rings as lever arms in new asymmetric benzodithiophene. *J. Mater. Chem. A* **6**, 18125–18132 (2018).

28. Fan Q., Xu Z., Guo X., Meng X., Li W., Su W., Ou X., Ma W., Zhang M. & Li Y. High-performance nonfullerene polymer solar cells with open-circuit voltage over 1 V and energy loss as low as 0.54 eV. *Nano Energy* **40**, 20–26 (2017).

29. Yan C., Barlow S., Wang Z., Yan H., Jen A. K.-Y., Marder S.R. & Zhan X. Non-fullerene acceptors for organic solar cells. *Nat. Rev. Mater.* **3**, 18003 (2018).

30. Wright M. & Uddin A. Organic—inorganic hybrid solar cells: A comparative review. *Sol. Energy Mater. Sol. Cells* **107**, 87–111 (2012).

31. Huang J., Huang Z., Yang Y., Zhu H. & Lian T. Multiple Exciton Dissociation in CdSe Quantum Dots by Ultrafast Electron Transfer to Adsorbed Methylene Blue. *J. Am. Chem. Soc.* **132**, 4858–4864 (2010).

32. Saini P. *Fundamentals of Conjugated Polymer Blends, Copolymers and Composites: Synthesis, Properties, and Applications*. (John Wiley & Sons, 2015).

33. Ren S., Bernardi M., Lunt R. R., Bulovic V., Grossman J. C. & Gradečak S. Toward efficient carbon nanotube/P3HT solar cells: active layer morphology, electrical, and optical properties. *Nano Lett.* **11**, 5316–5321 (2011).

34. Liu Q., Liu Z., Zhang X., Yang L., Zhang N., Pan G., Yin S., Chen Y. & Wei J. Polymer Photovoltaic Cells Based on Solution-Processable Graphene and P3HT. *Adv. Funct. Mater.* **19**, 894–904 (2009).

35. Rezek B., Čermák J., Kromka A., Ledinský M. & Kočka J. Photovoltage effects in polypyrrole–diamond nanosystem. *Diam. Relat. Mater.* **18**, 249–252 (2009).

36. Vernitskaya T. V. & Efimov O. N. Polypyrrole: a conducting polymer; its synthesis, properties and applications. *Russ. Chem. Rev.* **66**, 443–457 (1997).

37. Abthagir P. S. & Saraswathi R. Junction properties of metal/polypyrrole Schottky barriers. *J. Appl. Polym. Sci.* **81**, 2127–2135 (2001).

38. Ukraintsev E., Kromka A., Janssen W., Haenen K. & Rezek B. Controlling physical and chemical bonding of polypyrrole to boron doped diamond by surface termination. *Int J Electrochem Sci* **8**, 17–26 (2013).

39. Hsu M.-H., Chuang H., Cheng F.-Y., Huang Y.-P., Han C.-C., Chen J.-Y., Huang S.-C., Chen J.-K., Wu D.-S., Chu H.-L. & Chang C.-C. Directly Thiolated Modification onto

the Surface of Detonation Nanodiamonds. *ACS Appl. Mater. Interfaces* **6**, 7198–7203 (2014).

40. Stehlik S., Varga M., Ledinsky M., Miliaieva D., Kozak H., Skakalova V., Mangler C., Pennycook T. J., Meyer J. C., Kromka A. & Rezek B. High-yield fabrication and properties of 1.4 nm nanodiamonds with narrow size distribution. *Sci. Rep.* **6**, srep38419 (2016).

41. Arnault J.-C. *Nanodiamonds: advanced material analysis, properties and applications*. (Elsevier, 2017).

42. Turcheniuk K., Trecazzi C., Deeleepojananan C. & Mochalin V. N. Salt-Assisted Ultrasonic Deaggregation of Nanodiamond. *ACS Appl. Mater. Interfaces* **8**, 25461–25468 (2016).

43. Krueger A. & Lang D. Functionality is Key: Recent Progress in the Surface Modification of Nanodiamond. *Adv. Funct. Mater.* **22**, 890–906 (2012).

44. Shenderova O. A. & McGuire G. E. Science and engineering of nanodiamond particle surfaces for biological applications (Review). *Biointerphases* **10**, 030802 (2015).

45. Williams O. A., Hees J., Dieker C., Jäger W., Kirste L. & Nebel C. E. Size-dependent reactivity of diamond nanoparticles. *ACS Nano* **4**, 4824–4830 (2010).

46. Yeap W. S., Chen S. & Loh K. P. Detonation Nanodiamond: An Organic Platform for the Suzuki Coupling of Organic Molecules. *Langmuir* **25**, 185–191 (2009).

47. Mochalin V. N., Shenderova O., Ho D. & Gogotsi Y. The properties and applications of nanodiamonds. *Nat. Nanotechnol.* **7**, 11–23 (2012).

48. Stehlik S., Glatzel T., Pichot V., Pawlak R., Meyer E., Spitzer D. & Rezek B. Water interaction with hydrogenated and oxidized detonation nanodiamonds — Microscopic and spectroscopic analyses. *Diam. Relat. Mater.* **63**, 97–102 (2016).

49. Čermák J., Kozak H., Stehlík Š., Švrček V., Pichot V., Spitzer D., Kromka A. & Rezek B. Microscopic Electrical Conductivity of Nanodiamonds after Thermal and Plasma Treatments. *MRS Adv.* **1**, 1105–1111 (2016).

50. Krüger A., Liang Y., Jarre G. & Stegk J. Surface functionalisation of detonation diamond suitable for biological applications. *J. Mater. Chem.* **16**, 2322–2328 (2006).

51. Rojas S., Gispert J. D., Martín R., Abad S., Menchón C., Pareto D., Víctor V. M., Álvaro M., García H. & Herance J. R. Biodistribution of Amino-Functionalized Diamond Nanoparticles. In Vivo Studies Based on 18F Radionuclide Emission. *ACS Nano* **5**, 5552–5559 (2011).

52. Cheung K. M., Bloor D. & Stevens G. C. The influence of unusual counterions on the electrochemistry and physical properties of polypyrrole. *J. Mater. Sci.* **25**, 3814–3837 (1990).

53. John R. & Wallace G. G. The use of microelectrodes to probe the electropolymerization mechanism of heterocyclic conducting polymers. *J. Electroanal. Chem. Interfacial Electrochem.* **306**, 157–167 (1991).

54. Wang P.-C. & Yu J.-Y. Dopant-dependent variation in the distribution of polarons and bipolarons as charge-carriers in polypyrrole thin films synthesized by oxidative chemical polymerization. *React. Funct. Polym.* **72**, 311–316 (2012).

55. Fermín D. J., Teruel H. & Scharifker B. R. Changes in the population of neutral species and charge carriers during electrochemical oxidation of polypyrrole. *J. Electroanal. Chem.* **401**, 207–214 (1996).

56. Saunders B. R., Fleming R. J. & Murray K. S. Recent Advances in the Physical and Spectroscopic Properties of Polypyrrole Films, Particularly Those Containing

Transition-Metal Complexes as Counteranions. *Chem. Mater.* **7**, 1082–1094 (1995).

57. Stehlik S., Varga M., Ledinsky M., Jirasek V., Artemenko A., Kozak H., Ondic L., Skakalova V., Argentero G., Pennycook T., Meyer J. C., Fejfar A., Kromka A. & Rezek B. Size and Purity Control of HPHT Nanodiamonds down to 1 nm. *J. Phys. Chem. C* **119**, 27708–27720 (2015).

58. Smith B. Fundamentals of Fourier Transform Infrared Spectroscopy. *Taylor & Francis Group,* 19-54 (2011).

59. Binnig G., Quate C. F. & Gerber Ch. Atomic Force Microscope. *Phys. Rev. Lett.* **56**, 930–933 (1986).

60. Nečas D. & Klapetek P. Gwyddion: an open-source software for SPM data analysis. *Open Phys.* **10**, 181–188 (2011).

61. Huth F., Schnell M., Wittborn J., Ocelic N. & Hillenbrand R. Infrared-spectroscopic nanoimaging with a thermal source. *Nat. Mater.* **10**, 352–356 (2011).

62. Keilmann F. & Hillenbrand R. Near-field microscopy by elastic light scattering from a tip. *Philos. Transact. A Math. Phys. Eng. Sci.* **362**, 787–805 (2004).

63. Huth F., Govyadinov A., Amarie S., Nuansing W., Keilmann F. & Hillenbrand R. Nano-FTIR Absorption Spectroscopy of Molecular Fingerprints at 20 nm Spatial Resolution. *Nano Lett.* **12**, 3973–3978 (2012).

64. Westermeier C., Cernescu A., Amarie S., Liewald C., Keilmann F. & Nickel B. Sub-micron phase coexistence in small-molecule organic thin films revealed by infrared nano-imaging. *Nat. Commun.* **5**, (2014).

65. Remes Z., Babchenko O., Varga M., Stuchlik J., Jirasek V., Prajzler V., Nekvindova P. & Kromka A. Preparation and optical properties of nanocrystalline diamond coatings for infrared planar waveguides. *Thin Solid Films* **618**, 130–133 (2016).

66. Kaur N., Singh M., Pathak D., Wagner T. & Nunzi J. M. Organic materials for photovoltaic applications: Review and mechanism. *Synth. Met.* **190**, 20–26 (2014).

67. Bartesaghi D., Pérez I. del C., Kniepert J., Roland S., Turbiez M., Neher D. & Koster L. J. A. Competition between recombination and extraction of free charges determines the fill factor of organic solar cells. *Nat. Commun.* **6**, 7083 (2015).

68. Miliaieva D., Stehlik S., Stenclova P. & Rezek B. Synthesis of polypyrrole on nanodiamonds with hydrogenated and oxidized surfaces: Synthesis of polypyrrole on nanodiamonds. *Phys. Status Solidi A* **213**, 2687–2692 (2016).

69. Miliaieva D, Stehlik S., Stenclova P. & Rezek B. Nanodiamonds improve charge carrier generation from organic dye. Submitted in *J. Mater. Chem. A* (June 2019).

70. Chang Y.-C., Miliaieva D. & Rezek B. Study of photovoltage stability on nanodiamond-polypyrrole composites by Kelvin probe method. Proc. of the 10th International Conference Nanocon, 164–168 (2018).

71. Stehlik S., Varga M., Ledinsky M., Miliaieva D., Kozak H., Skakalova V., Mangler C., Pennycook T. J., Meyer J. C., Kromka A. & Rezek B. High-yield fabrication and properties of 1.4 nm nanodiamonds with narrow size distribution. *Sci. Rep.* **6**, (2016).

72. Stehlik S., Miliaieva D., Varga M., Kromka A. & Rezek B. Size decrease of detonation nanodiamonds by air annealing investigated by AFM. *MRS Adv.* **1**, 1067–1073 (2016).

73. Čermák J., Kozak H., Stehlík Š., Švrček V., Pichot V., Spitzer D., Kromka A. & Rezek B. Microscopic Electrical Conductivity of Nanodiamonds after Thermal and Plasma Treatments. *MRS Adv.* **1**, 1105–1111 (2016).

74. Chiesa S. & Rossi M. J. The metastable HCl · 6H$_2$O phase - IR spectroscopy, phase transitions and kinetic/thermodynamic properties in the range 170-205 K. *Atmospheric Chem. Phys.* **13**, 11905–11923 (2013).

75. P. Beck J., Gaigeot M.-P. & M. Lisy J. Anharmonic vibrations of N–H in Cl − (N - methylacetamide) 1 (H 2 O) 0–2 Ar 2 cluster ions. Combined IRPD experiments and BOMD simulations. *Phys. Chem. Chem. Phys.* **15**, 16736–16745 (2013).

76. Valtera S., Prokeš J., Kopecká J., Vrňata M., Trchová M., Varga M., Stejskal J. & Kopecký D. Dye-stimulated control of conducting polypyrrole morphology. *RSC Adv.* **7**, 51495–51505 (2017).

77. Cordeiro E. R., Fernandes A. W. C., Pereira A. F. C., Costa M. M. da, Nascimento M. L. F., Oliveira H. P. de, Cordeiro E. R., Fernandes A. W. C., Pereira A. F. C., Costa M. M. da, Nascimento M. L. F. & Oliveira H. P. de. Staphylococcus aureus biofilm formation on polypyrrole: an electrical overview. *Quím. Nova* **38**, 1075–1079 (2015).

78. Petit T. & Puskar L. FTIR spectroscopy of nanodiamonds: Methods and interpretation. *Diam. Relat. Mater.* **89**, 52–66 (2018).

79. Valtera S., Prokeš J., Kopecká J., Vrňata M., Trchová M., Varga M., Stejskal J. & Kopecký D. Dye-stimulated control of conducting polypyrrole morphology. *RSC Adv.* **7**, 51495–51505 (2017).

80. Amenabar I., Poly S., Nuansing W., Hubrich E. H., Govyadinov A. A., Huth F., Krutokhvostov R., Zhang L., Knez M., Heberle J., Bittner A. M. & Hillenbrand R. Structural analysis and mapping of individual protein complexes by infrared nanospectroscopy. *Nat. Commun.* **4**, 2890 (2013).

81. Stehlik S., Varga M., Stenclova P., Ondic L., Ledinsky M., Pangrac J., Vanek O., Lipov J., Kromka A. & Rezek B. Ultrathin Nanocrystalline Diamond Films with

Silicon Vacancy Color Centers via Seeding by 2 nm Detonation Nanodiamonds. *ACS Appl. Mater. Interfaces* **9**, 38842–38853 (2017).

82. Sugimoto H., Ozaki Y. & Fujii M. Silicon Quantum Dots in Dielectric Scattering Media: Broadband Enhancement of Effective Absorption Cross Section by Light Trapping. *ACS Appl. Mater. Interfaces* **9**, 19135–19142 (2017).

83. Brédas J. L., Themans B. & Andre J. M. Bipolarons in polypyrrole chains. *Phys. Rev. B* **27**, 7827 (1983).

84. Bredas J. & Street G. Polarons, Bipolarons and Solitons in Conducting Polymers. *Acc. Chem. Res.* **18**, 309-315 (1985).

85. Matunová P., Jirásek V. & Rezek B. Structural and Electronic Properties of Oxidized and Amorphous Nanodiamond Surfaces with Covalently Grafted Polypyrrole. *Phys. Status Solidi B*, DOI 10.1002/pssb.201900176 (2019).

86. Matunová P., Jirásek V. & Rezek B. Computational study of physisorption and chemisorption of polypyrrole on H-terminated (111) and (100) nanodiamond facets. *Phys. Status Solidi A* **213**, 2672–2679 (2016).

87. Gregg B. A. & Hanna M. C. Comparing organic to inorganic photovoltaic cells: Theory, experiment, and simulation. *J. Appl. Phys.* **93**, 3605–3614 (2003).

List of Abbreviations

OPV - organic photovoltaics

NFA - non-fullerene acceptors

ND - nanodiamond

DND - detonation nanodiamond

poly-DND - polyfunctional nanodiamond

O-DND - oxidised nanodiamond

H-DND - hydrogenated nanodiamond

PPy - polypyrrole

AFM - atomic force microscopy

FTIR - Fourier transform infrared spectroscopy

SNOM-IR - scattering-type near-field optical microscope combined with the infrared spectrometer

PDS - photothermal deflection spectroscopy

SKP - scanning Kelvin probe

SP - surface potential

SPV - surface photovoltage

DFT - density functional theory

HOMO - highest occupied molecular orbital

LUMO - lowest unoccupied molecular orbital

I-V (characterisation) - current-voltage (characterisation)

V_{oc} – open-circuit voltage

I_{sc} – short-circuit current

FF – fill factor

Publications

Own contribution of the author

In the publications related to the thesis the author, Daria Miliaieva, developed the fabrication procedure of the nanodiamond-polypyrrole composites, performed AFM, KPFM, SKP and DLS measurements, processed the data from the measurements, and interpreted the results of the measurements. Also, she fabricated solar cells and checked their IV characteristics. The author created all the figures and tables related to the experimental results presented in the publications and supplementary information, where she is the first author. The author wrote all the texts in all the publications where she is the first author. The texts were further reshaped by the co-authors. Also, the co-authors were in charge of the experimental techniques like FTIR, SNOM-IR and PDS used to investigate the DND/PPy materials and took part in the preliminary discussions on the experiments.

Publications of Ing. Daria Miliaieva related to the thesis

In the cases of the unequal authors' contributions, the contributions are stated in the brackets.

Impact factor journals of WoS SCI:

1. D. Miliaieva (55%), P. Matunova (10%), J. Cermak (5%), S. Stehlik (5%), A. Cernescu (5%), Z. Remes (5%), P. Stenclova (5%), B. Rezek (10%), *Nanodiamonds improve charge carrier generation from organic dye,* submitted in Journal of Materials Chemistry A (2019).

2. D. Miliaieva (60%), S. Stehlik (15%), P. Stenclova (10%), B. Rezek (10%), *Synthesis of polypyrrole on nanodiamonds with hydrogenated and oxidised surfaces,* Physica status solidi (a) 213 (2016), 2687-2692, DOI:10.1002/pssa.201600278.

   Citations: 5

3. Š. Stehlík, M. Varga, M. Ledinský, D. Miliaieva, H. Kozak, V. Skákalová, C. Mangler, T. J. Pennycook, J. C. Meyer, A. Kromka, B. Rezek, *High-yield*

fabrication and properties of 1.4 nm nanodiamonds with narrow size distribution, Sci. Rep. 6 (2016), 38419(1)-38419(8), DOI: 10.1038/srep38419.

Citations: 22

Publications in other peer-reviewed journals:

1. Š. Stehlík (45%), D. Miliaieva (35%), M. Varga (5%), A. Kromka (5%), B. Rezek (10%), *Size decrease of detonation nanodiamonds by air annealing investigated by AFM,* MRS Advances 1 (2016), 1067-1073, DOI: 10.1557/adv.2016.36.

Citations: 5

Conference papers:

1. Y.-C. Chang (50%), D. Miliaieva (40%), B. Rezek (10%), *Study of photovoltage stability on nano diamond-polypyrrole composites by Kelvin probe method,* Proc. of the 10th International Conference Nanocon (2018) 164–168, ISBN 978-80-87294-89-5.
2. J. Cermak (40%), D. Miliaieva (40%), H. Hoppe (10%), B. Rezek (10%), *Back electrode influence on optoelectronic properties of organic photovoltaic blend characterised by Kelvin probe force microscopy,* Proc. of the 8th International Conference Nanocon (2017) 291-295, ISBN 978-80-87294-71-0.

Other publication of Ing. Daria Miliaieva

Impact factor journal of WoS SCI:

1. A. Larin, D. Milyaeva, A. Rybakov, D. Bezrukov, D. Trubnikov, *Internal (SiH)X groups, X = 1 - 4, in microcrystalline hydrogenated silicon and their IR spectra based on periodic DFT modelling,* Molecular Physics 112 (2014), 956-962, DOI:10.1080/00268976.2013.817621.

Citations: 4

List of Activities

Oral Presentations

5th International Conference on Multifunctional, Hybrid and Nanomaterials (March 2017), Lisbon, Portugal. Title of the presentation: 'Modification of nanodiamond particles with polypyrrole: theoretical and experimental study'.

9th International Conference on Nanomaterials NANOCON (October 2017), Brno, Czech Republic. Title of the presentation: 'Influence of Annealing on Optoelectronic Properties of Nanodiamond'.

10th International Conference on Nanomaterials NANOCON (October 2018), Brno, Czech Republic. Title of the presentation: 'Nanodiamonds improve charge carrier generation from organic dyes'.

The 2019 E-MRS Fall Meeting and Exhibition at Warsaw University of Technology (September 2019), Warsaw, Poland. Title of the presentation: 'Nanodiamond surface chemistry controls assembly of organic dyes and photovoltage'.

Poster Presentations

21st Hasselt Diamond Workshop (March 2016), Hasselt, Belgium 21st Hasselt Diamond Workshop (March 2016), Hasselt, Belgium. Title of the presentation: 'Synthesis of Polypyrrole on Nanodiamonds With Hydrogenated and Oxidised Surfaces'.

8th International Conference on Nanomaterials - Research & Application (NANOCON, October 2016), Brno, Czech Republic. Title of the presentation: 'Influence of Annealing in Surface Photovoltage of Detonation Nanodiamond Particles'.

16th IUVSTA International Summer School on Physics at Nanoscale (June 2017), Devet Skal, Czech Republic. Title of the presentation: 'Bonding and optoelectronic properties in detonation nanodiamond-dye composites'.

Cena Nadace ČEZ 2017 (June 2017), Prague, Czech Republic. Title of the presentation: 'Bonding and optoelectronic properties in a nanodiamond-dye composite'.

Grant investigator

The principal investigator of the grant SGS16/222/OHK4/3T/13 (01/2016 – 01/2018) on 'Study of diamond surface functionalization by polypyrrole using experimental and computational methods'.

Awards

Awarded in competition 'Cena Nadace ČEZ 2017' for the 3rd place in a category 'Electrotechnology and measurements' for a project 'Bonding and optoelectronic properties in a nanodiamond-dye composite'.

Second place in a national round of 'Present Around the World Competition' organised by the Czech Centre of EIT (Institute of Engineering and Technology), May 2019.

Attached Publications

Nanodiamond surface chemistry controls assembly of organic dye and photovoltage

Daria Miliaieva,*[a,b] Petra Matunova,[a,b] Jan Cermak,[a] Stepan Stehlik,[a] Adrian Cernescu,[c] Zdenek Remes,[a] Pavla Stenclova,[a] and Bohuslav Rezek[a,b]

Nanoscale composite of detonation nanodiamond (DND) and polypyrrole (PPy) as an organic dye is explored as a novel concept for energy generation, using nanodiamond as an inorganic electron acceptor. We present a technology for the composite layer-by-layer synthesis that is suitable for solar cell fabrication. The formation, pronounced material interaction, and photovoltaic properties of DND-PPy composites are characterized down to nanoscale by atomic force microscopy, infrared spectroscopy, Kelvin probe and electronic transport measurements. The data show that DNDs with different surface terminations (hydrogenated, oxidized, poly-functional) assemble PPy oligomers in different ways. This leads to composites with different optoelectronic properties. Tight material interaction results in significantly enhanced photovoltage and broadband (1 - 3.5 eV) optical absorption in DND/PPy composites compared to pristine materials. Combination of both oxygen and hydrogen functional groups on the nanodiamond surface appears to be the most favourable for the optoelectronic effects. Theoretical DFT calculations corroborate the experimental data. Prototype hybrid solar cell demonstrates the functionality of the concept.

1. Introduction

Renewable photovoltaic (PV) energy generation provides an increasing contribution to on-grid and off-grid electricity demands in many developed and developing countries worldwide.

Light energy conversion already covers a considerable part of energy requirements in many countries. Nowadays, the fabrication of PV solar cells is dominated by crystalline Si technology. Nevertheless, organic-based PV (OPV) envisioned many years ago has become a viable alternative with many real applications. The reason is that OPV can offer numerous advantages over Si technology. The main factors are: (i) shorter time to return the energy used for device fabrication, (ii) lower production and deployment costs and (iii) better output power under low-light or diffuse light conditions such as in hazy weather, building integration or indoor applications.[1] However, to be widely accepted OPV still needs improvements in terms of efficiency and in particular long-term stability of operation. Fullerene-based acceptors, which are still commonly used for OPV active layer production, add to OPV thermal and photochemical instabilities.[2]

Quantum dots and nanoparticles from various materials represent promising components in the thin film energy conversion and storage devices.[3] The reasons for the use of nanoparticles in photovoltaic conversion are quantum size effects that enable to tune absorption spectrum, inherent nanostructuring of interfaces with high surface-to-volume ratio, better electronic transport properties and higher durability. The nanoparticles, as shown in this work, may also contribute to the alignment of the polymer chains. Nowadays the ordering of polymers in OPV blends is a matter of concern since the proper polymer structuring improves the performance and the stability of solar cells.[4] When the nanoparticles are mixed with organic materials, such nanocomposites are solution processable and they should thus enable inexpensive large-scale solar cell manufacturing. Carbon nanomaterials like graphene or carbon nanotubes have also been characterized in such systems.[5] The research field of such organic-based photovoltaics is very broad.[6] Yet the potential of nanodiamond (i.e. diamond nanoparticles) for energy conversion remains virtually unexplored[7] even though they represent highly promising material in this respect.

Nanodiamonds (ND) provide many unique qualities that are highly advantageous for energy conversion applications in comparison to other materials (Si, TiO_2, etc.[8–10]). Except for specific surface reactions, NDs and their structural as well as electronic properties are very stable under various conditions for a long time.[11] Diamond nanoparticles are merely carbon and they are completely non-toxic in environment and organisms.[12,13]
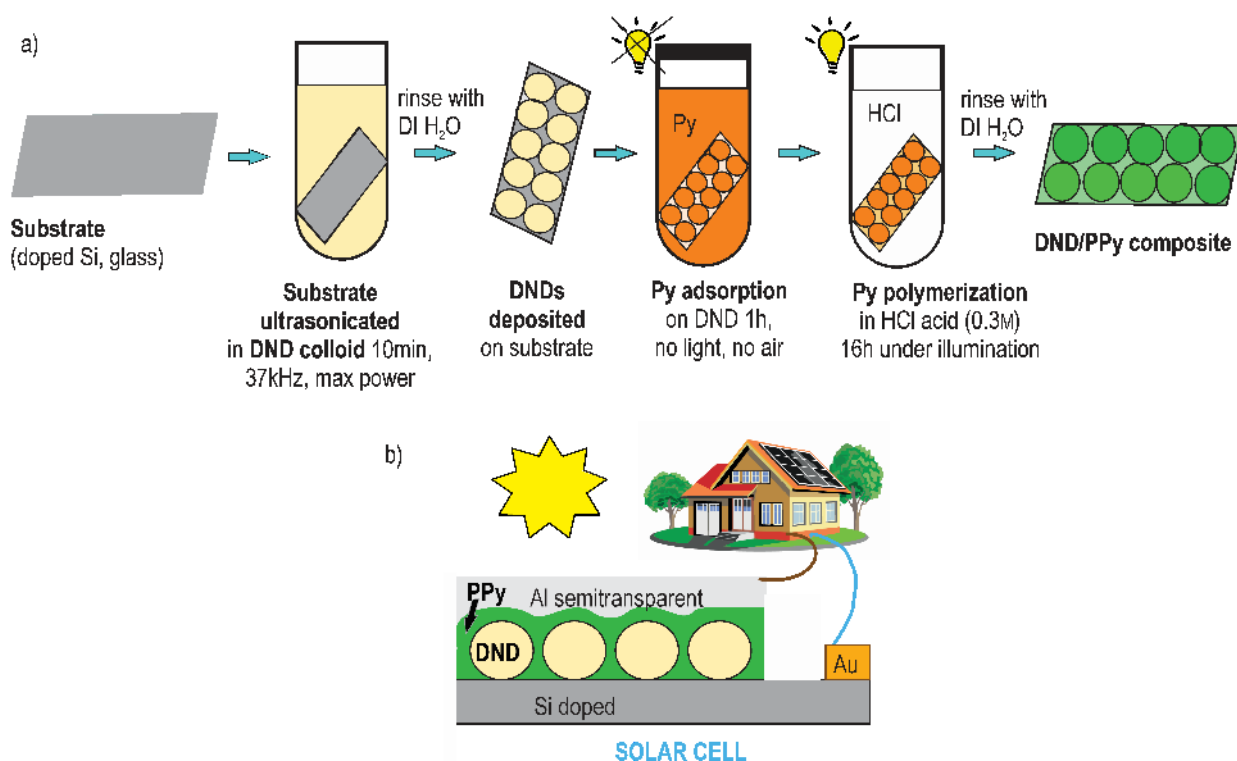
Figure 1. Scheme of a) fabrication process of DND/PPy composite and b) test solar cell with DND/PPy composite as active material.

As a waste, they can be stored indefinitely or burnt into CO_2, and they do not need any specific disposal procedures. Covalent chemistry works similarly on NDs as for organics. Various chemical moieties can be thus grafted on NDs surfaces.[14] Colloidal chemistry of NDs is also well established. It enables mixing of NDs with polymers without clustering or segregation. Unwanted phase segregation is one of the crucial problems in the development of organic PV cells.[15] The NDs are also available in large quantities at reasonable prices (1 $/g). These features enable possible large-scale use of NDs without problems.

For energy conversion applications, preliminary research on bulk diamond already showed that merging diamond and organics, namely polypyrrole (PPy) can provide an efficient interface for exciton dissociation and electron transfer.[16,17] PPy is a well-investigated organic dye. It absorbs visible light[18], shows good conductivity[19] and can be obtained by various fabrication techniques.[20–26] Optoelectronic properties of PPy can be tuned by oxidation/reduction of the polymer and by using different electrolytes in the polymerization solution.[27] By increasing the oxidation state of PPy the number of positively charged units (polarons and bipolarons) in the polymer chain increases[27–30] which introduces energy levels (bands in case of pronouncing oxidation) into PPy bandgap.[31,32] This enhances PPy light absorption in the infrared region.

In work here, we, therefore, merge NDs and PPy together. We present a novel fabrication technology and optoelectronic characterization of nanocomposites based on detonation nanodiamonds (DNDs) and PPy. We revealed a tight interaction between DNDs and PPy in the composites, which leads to enhanced optical absorption and more efficient charge generation. We provide theoretical calculations of the structure and electronic properties of DND/PPy composites, which are in a good agreement with the experimental data and which help elucidate the mechanism of exciton dissociation in DND/PPy composite. Preliminary simple solar cell with DND/PPy composite as an active material is fabricated as a proof of principle.

2. Experimental part

2.1 Materials

Original DNDs were manufactured by Lingyun Granda Nano (China) and distributed by New Metals and Chemicals (Japan). Fourier-transform infrared spectroscopy (FTIR) of the purchased DNDs showed in the as-received state pronounced peaks at 2800-3000 cm^{-1} that correspond to C-H surface groups as well as peaks at 1800 cm^{-1} due to carbonyl C=O groups. Therefore, to emphasize the presence of multiple types of surface moieties (related to both oxygen and hydrogen) we will refer to the as-received DNDs as polyfunctional-DNDs (poly-DND) in the further text. The average size of poly-DND claimed by the manufacturer is around 5 nm. Zeta potential of polyfunctional-DNDs is positive, +41 mV (measured by Malvern Zetasizer). Oxidized DNDs (O-DND) were obtained from polyfunctional-DNDs by annealing in air at 450 °C for 30 minutes. Such oxidation conditions do not lead to poly-DND size reduction.[32] Zeta potential of such annealed DNDs is -39 mV. Hydrogenated DNDs (H-DND) were obtained from O-DNDs by treatment in a hydrogen plasma at 600 °C for 6 hours.[33] Our preliminary DLS measurements reveal H-DND size to be around 3nm. Zeta potential of H-DND is + 40 mV, thus similar to poly-

DNDs yet the FTIR spectra are considerably different (see Figure 1S in ESI). Hydrochloric acid (HCl, 37%) and pyrrole (98%) for polypyrrole synthesis were purchased from Sigma-Aldrich (USA) and used in the as-received state.

2.2 Nanocomposite fabrication

Figure 1a shows a scheme of the layer-by-layer technological procedure developed for the preparation of DND/PPy nanocomposite layers on substrates. The substrates (silicon or glass) were nucleated with DND particles by sonication for 1 hour in colloidal DND solution (prepared according to the established protocol[32]) and then they were rinsed with deionized water. Nucleation of the substrates by DND resulted in 10% and 40% coverage of the substrates by poly-DND or H-DND respectively.[33] Direct nucleation of the substrates by O-DND, in the same way, was complicated due to electrostatic repulsion between oxidized DNDs and oxidized silicon or glass surface. Thus, to get similar Si and glass nucleation with O-DNDs we nucleated the substrate with poly-DND at first and then annealed the substrates in the air at 450 ^{0}C for 30 minutes. The morphology of DND nucleated substrates was characterized by AFM and it is shown in Figure S2.

Substrates with a low density of DND agglomerates (about 30 agglomerates per 1 μm^2) were prepared to obtain nanoscale spectroscopic data on the particles and the surrounding substrate separately. Mean size of agglomerates was selected around 30 nm for facilitating the SNOM-IR measurements with high enough signal on DNDs without substrate influence. To get 30 nm fraction of DND particles, their stock colloidal solution was centrifuged at 14000 rpm (13124x g) for 1 minute to get rid of micrometre-sized agglomerates. Then it was poured into the clean flask and further centrifuged for 1 hour. The sediment after 1-hour centrifugation was re-dispersed in 1 ml of water and then further diluted 20 times. The substrates were nucleated with this solution. See Figure S3 in ESI for the resulting surface morphology with uniformly distributed DND clusters.

After nucleation with DNDs, the substrates were soaked in Py monomer for 1 hour to let Py monomers adsorb (see again the scheme in Figure 1a). Then the substrate with adsorbed Py was immersed into HCl acid (0.3 M) for 16 hours under indoor illumination to promote Py polymerization. The substrate was then taken out of HCl, rinsed with deionized water, and dried with N_2. Substrates processed in the same way, but without DNDs, were used as PPy reference substrates. Substrates nucleated with DND particles without further Py processing were used as DND reference substrates. PPy layer morphology and thickness were again investigated by AFM.

For preparation of the test solar cell (Figure 1b) a back electrode was covered with DND/PPy composite as an active material and a counter electrode was sputtered on top. Different materials were tested as back electrodes: metals (Au, Al), glass with ITO film (with and without PEDOT:PSS), silicon (Si) with different doping (p, p++, n, n++). As the top electrodes metallic (Al, Au) semi-transparent (18 nm thickness) stripes of approximate 0.05 cm^2 area were sputtered by thermal evaporation technique.

2.3 Experimental techniques

Atomic force microscopy (AFM, NTMDT Ntegra) was used in the tapping mode (Si cantilevers with 75 kHz resonance frequency) to characterize the morphology and thickness of the reference poly-DND, H-DND and O-DND nucleated substrates as well as the substrates after the composite formation. Part of the particles on each sample were carefully removed by a thin wood stick. The samples were scanned perpendicular to the interface between exposed and nucleated part of substrates. Height of the bare substrate was taken as the zero height. Height of each grain on the samples was determined by using a watershed algorithm[34] relative to the exposed substrate. Mean heights of composite and reference DNDs particles were calculated. The PPy layer thickness on DNDs was determined by the formula in [35].

Scanning electron microscopy (FE-SEM Tescan MAIA3) was used as a complementary tool to characterize surface morphology. Field-emission gun operating at 10 kV and in-beam secondary electron detector were used.

Formation of the DND/PPy composites was characterized by infrared spectroscopy: macroscopically by grazing angle reflectance Fourier-transform infrared spectroscopy (GAR-FTIR) and microscopically by scanning near-field optical microscopy in infrared region (SNOM-IR). GAR-FTIR spectra were measured using N_2-purged Thermo Nicolet 8700 spectrometer equipped with KBr beam splitter and MCT detector cooled by liquid nitrogen. Au mirrors were chosen as substrates for GAR-FTIR measurements to ensure high enough signal from the samples. The optical absorbance was calculated in the standard absorbance units as A = −log(R/R$_0$), where R is the spectrum of analyzed material and R$_0$ is the reference (background) spectrum recorded using clean Au mirror prior to the analyte application. In all cases, the spectra represent an average of 128 scans recorded with a resolution of 4 cm^{-1}. FTIR spectra were normalized to the intensity of the strongest peak in the spectrum.

SNOM-IR spectra were collected with ca. 20 nm spatial resolution using a scattering-type near-field optical microscope (neaSNOM, neaspec GmbH) equipped with a broadband Difference Frequency Generation (DFG) laser source (Toptica) and an asymmetric Michelson interferometer described elsewhere.[36] PtIr tip with ca. 20 nm diameter was used to probe the sample by operating in tapping mode (tapping amplitude ca. 40nm) at the frequency Ω of ca. 270 kHz, thus modulating the intensity of the scattered IR light at Ω and its higher harmonics. Individual spectra were recorded in ca. 3 minutes each, with a spectral resolution of 8.3 cm^{-1}. Demodulation of the scattered light signal at a higher harmonic nΩ was used to separate the contribution of the near-field optical signal from that of the background signal.[37] Removal of the instrumental response function from the SNOM-IR spectra was done by normalization of the measured spectra to a reference Si signal. Resulting SNOM-IR Absorption and Reflectivity spectra can be directly correlated with the standard far-field IR spectra.[38,39]

Scanning Kelvin Probe (SKP, KPTechnologies) method was used to determine the surface potentials of the samples and subsequently, by applying illumination surface photovoltages

were calculated. Its advantage compared to Kelvin Probe Force microscopy is possibility of "absolute" dark conditions of measurements as no laser is required for probe position detection in SKP. Scanning of each sample was conducted with a golden tip of 2 mm in diameter at 25 different points. The value of surface potential (SP) for the specified sample at specified conditions (dark/illumination) was taken as the average value of SPs at these 25 points. SP was measured on one and the same area in the dark and under illumination. As the light source halogen lamp was used with a light intensity of about 200 W/m². The reported value of surface photovoltage (SPV) was calculated as $SPV = SP\ (under\ illumination) - SP\ (dark)$.

Photothermal deflection spectroscopy (PDS) was used to characterize optical transmittance, reflectance and absorbance spectra in the broad spectral range from UV to near IR (250–1700 nm). The absorption coefficient (1/cm) at each wavelength was calculated from absorptance spectra and the thickness of the samples as

$$Absorption\ coefficient = \frac{-ln(1-Absorptance)}{Sample\ thickness}.$$

The thickness of the PDS samples prepared on glass was evaluated by AFM. Figure S4 shows the thickness evaluation from AFM images on the DND-PPy composite samples. During PDS measurements the samples were immersed into transparent liquid FC72 and their absorptance spectra were normalized via absorptance spectrum of the highly absorbing black coating.[40]

Current-voltage (IV) characteristics were measured by needle probes in a measurement setup using a source-measure unit (Keithley). One of the microelectrodes was in contact with a steel carrier disk. The solar cell back electrode was fixed to the steel disk by a gold paste. The other microelectrode is in contact with the solar cell top electrode through a silver paste. The current was measured in voltage range ± 0.4 V with the sweep rate 50 mV/s. IV curves were measured in the dark and under solar simulator illumination (light intensity 1000 W/m²). Power conversion efficiency (PCE) of the cell was calculated as

$$PCE\% = \frac{P_{max} \times 100\%}{P_{incident}},$$

where $P_{incident} = Light\ intesity\ of\ solar\ simulator \times Area\ under\ illumination$ is power of incident light and Pmax is maximum output power of solar cell which is defined by the maximum product of input voltage and corresponding current. Area under illumination is equal to the area of top electrode.

2.4 Theoretical computing procedures

The first-principles density functional theory (DFT) method implemented in Gaussian 09 software[41] was used for optimizations of all the structures in order to obtain the ground state configurations. B3LYP hybrid functional,[42,43] one of the most widely used functionals in computations of organic molecules, was employed together with the 6-31G(d) basis set. Modelling whole ND with experimentally accessible size starting at 1.4 nm [44] would be computationally unfeasible at this level of theory. Therefore, we used (111) and (100) surface slabs consisting of 3 C double layers of 6 × 6 atoms, exceptionally 5 × 6 atoms if structurally needed. The slabs represent a corner of ND, hence always three "outer" surfaces of ND are functionalized with surface groups, and the remaining three "inner" surfaces representing the inner cut planes are saturated with H atoms in order to keep the sp³ hybridization of neighboring carbon atoms. These H atoms were fixed during further optimization. Further details on structure optimization and energy levels calculations can be found in [45,46].

4 | *J. Mater.*Chem. A, 2019, **00**, 1-10

This journal is © The Royal Society of Chemistry 20xx

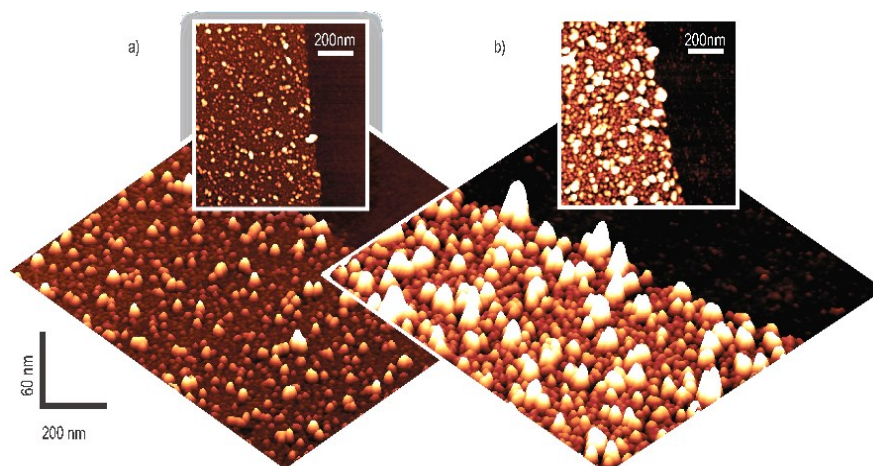# 3. Results and discussion

Figure 2. AFM images of a) H-DND reference b) H-DND/PPy

Figure 2 shows topography images obtained by AFM. Planar images show particles distribution and height enlargement. 3D images visualize overall size enlargement after processing of the DNDs with Py. As can be seen from the AFM images, already reference DND particles (Figure 2a) form aggregates of different sizes on the substrate. To understand how surface chemistry influences DNDs interaction with the PPy dye we selected the sizes that correspond to primary particles (for poly-DND and O-DND it is 4.5-5.0 nm and for H-DND it is 3 nm) or 2-particle aggregates. Larger aggregates introduce uncertainties in the PPy thickness interpretation due to e.g. different surface chemistry of aggregates compared to the primary particles. Evaluated mean particle sizes are summarized in Table 1. Mean sizes of poly-DND (4.8 ± 0.2 nm) and O-DND (5.1 ± 0.4 nm) are similar. This confirms that the annealing does not reduce the particle size but modifies the surface groups only. H-DND mean size is somewhat smaller, 2.9 ± 0.1 nm, as expected from the hydrogenation process.[33]

After the pyrrole processing, there is an enlargement in particles height (see Table 1) which is dependent on the particle's initial surface chemistry.

The thickest PPy layer is formed on poly-DND (4.2 ± 0.4 nm) and the minimum PPy thickness is observed on O-DND (1.4 ± 0.7

nm). PPy layer on H-DND (3.8 ± 0.1 nm) is of the similar thickness as on poly-DND. PPy thicknesses on O-DND and poly-DND appeared to be smaller than estimated in our previous work.[35] This might be due to the more accurate particle height evaluation procedure in this work by grain analysis using watershed method (see the Experimental section) compared to particle height estimation via roughness analysis in [35], where mean particle height was determined as the difference between roughness of nucleated and exposed parts of a substrate. However, different particle height evaluation methods lead to the same trend in PPy thickness which is maximum on poly-DND and 2 - 3 times less on O-DND. In view of the same Py polymerization conditions for all types of DND particles different PPy thickness on poly-, H- and O-DND, as was discussed in [35], can be explained by the different PPy chains arrangement relative to the different types of DNDs. The different PPy arrangement might be caused by the different bonding nature between PPy and DNDs of different surface terminations.

Interaction of DND and PPy in the composites were thus characterized by the IR spectroscopic techniques. Figure 3 shows FTIR spectra of DND/PPy, pristine DNDs and pristine PPy. The spectra indicate the formation of the nanocomposites. The remaining features of pristine DNDs (black arrows) and PPy (red arrows) can be seen in the spectra. At the same time some of the characteristic vibrations of DNDs are quenched by interaction with PPy. The band of C–H vibrations at 2800–3000 cm^{-1}, is clearly pronounced in the initial H-DNDs and poly-DNDs spectra. It is missing in poly-DND/PPy composite spectrum. It seems to be also missing in H-DND/PPy composite spectrum, yet some C-H vibrations may be hidden in the band of O-H···Cl and N-H···Cl vibrations at 2800–3000 cm^{-1}.[47,48] The peak of carbonyl group, which is present in the reference O-DND spectrum at 1800 cm^{-1} is completely missing in the O-DND/PPy composite spectrum. The regions of 800-1100 and 2250-3770 cm^{-1} (red background) reveal the new features in the DNDs/PPy composite compared to the pristine components. Moreover,

Table 1 Mean height of DND particles and the composites established from AFM topography data and calculated PPy thicknesses.

Sample name	Mean Particle Height, nm	PPy thickness, nm
poly-DND	4.8 ± 0.2	
poly-DND/PPy	9.0 ± 0.3	4.2 ± 0.4
H-DND	2.9 ± 0.1	
H-DND/PPy	6.7 ± 0.1	3.8 ± 0.1
O-DND	5.1 ± 0.4	
O-DND/PPy	6.5 ± 0.6	1.4 ± 0.7

This journal is © The Royal Society of Chemistry 20xx

J. Mater. Chem. A., 2019, **00**, 1-3 | **5**

the difference between the composites spectra in these regions suggests the different type of interaction between PPy and DND of different surface terminations. The peak at 1034 cm^{-1} of poly-DND/PPy composite has a distinct shoulder at 970 cm^{-1}, which is absent in PPy reference spectrum. This feature is attributed to C-C out-of-plane deformations of PPy ring. [49,50] In H-DND/PPy, the shape of 1034 cm^{-1} peak differs from the one of PPy reference, it is broadened and with the shoulder of C-C out of plane vibrations as in poly-DND/PPy. In O-DND/PPy, the region in 800-930 cm^{-1} seem to be a superposition of DND (850 cm^{-1} peak can be attributed to C-Cl in diamond particle[51] and thus it indicates possible partial chlorination of O-DND surface after interaction with HCl solution) and PPy vibrations (880 cm^{-1} peak can be attributed to C-H out of PPy ring plane deformations[49]).

The range in 2250-3770 cm^{-1} represents a complex mixture of OH, NH and O-H···Cl and N-H···Cl vibrations.[47,51,52] There is a noticeable redshift of the poly-DND/PPy bands in 2250-3770 cm^{-1} region compared to other composites and PPy ref. The shape of poly-DND/PPy spectrum in this region differs from the spectrum shape of the other materials. It might be due to the largest amount of O-H bonds on the poly-DND surface compared to H-DND and O-DND (carbonyl and carboxyl groups dominate in O-DNDs) particles. Thus, O-H···Cl dominates in poly-DND/PPy in the 2250-3770 cm^{-1} region while spectra of the other composites in this range are dominated by N-H···Cl or NH vibrations and they are blueshifted.

FTIR, measuring the averaged signal from the sample, does not enable us to distinguish between the signal from PPy on the particles and PPy on the substrate of the same sample. To overcome this limitation of FTIR and further elucidate the differences in the composites structure, we performed SNOM-IR spectroscopy with a nanoscale resolution.

In Figure 4, SNOM-IR spectra of poly-DND/PPy, O-DND/PPy and PPy reference are presented. Topography images of the samples (by AFM) are shown as well. The spectra of given colour correspond to the place on the topography image marked by the rectangle of the same colour. Figure 4a shows PPy reference spectra at 5 different locations on the substrate, including both plains and hillocks, which all match well with each other. Figure 4b shows the spectra of PPy on O-DND particles (orange line) and their surroundings (blue line). Several spectra taken on O-DND/PPy particles match with each other and reveal a distinct peak at 1408 cm^{-1} not found in the spectra of the surroundings. Figure 4c shows spectra taken on the poly-DND/PPy particles (red lines) and the substrate (blue line). The spectra are well reproducible. Spectra taken on the substrate differ from the ones on poly-DND/PPy particles by the more pronounced intensity of the peak at 1671 cm^{-1}, while in the rest of the spectral region the spectra match well.

A new peak at 1408 cm^{-1} in O-DND/PPy compared to PPy reference can be attributed to C-N vibrations which became asymmetrical (due to electrostatic interactions of O-DND and PPy) and subsequently visible in SNOM-IR spectrum. The peak at 1671 cm^{-1} presented in all SNOM-IR spectra is most likely attributed to N-H vibrations. The intensity of the peak does not depend on the thickness of PPy layer (the spectra on PPy references taken on PPy micron-size agglomerate and PPy thin film of about 20 nm thickness are comparable, see Figure 3a). Interaction of PPy with O-DND does not influence 1671 cm^{-1}
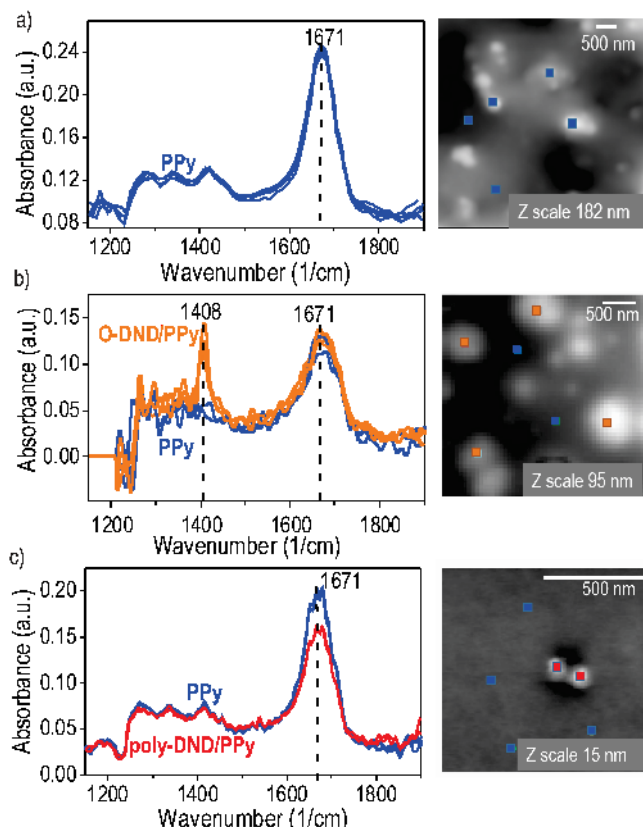

Figure 4. AFM maps with indicated locations of SNOM-IR spectra of a) PPy reference b) O-DND/PPy c) poly-DND/PPy. Lateral size of the particles' and PPy agglomerates could be deduced from the scale bars on AFM images. Characteristic PPy peaks at 1671 (N-H vibration) and 1408 (C-N vibration) cm^{-1} are indicated at SNOM-IR spectra.
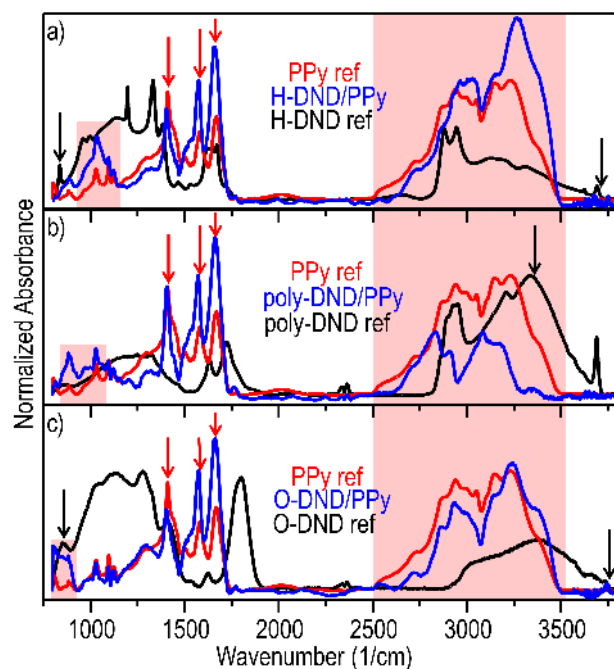

Figure 3. FTIR spectra of a) H-DND/PPy b) poly-DND/PPy and c) O-DND/PPy composites with the reference DNDs and PPy.

peak intensity since it can be of the same electrostatic nature as the interaction between PPy and silicon (with native silicon oxide) substrate. Thus, the difference in 1671 cm^{-1} peak intensity in poly-DND/PPy composite suggests different bonding nature with a different arrangement of PPy on Si substrate (e.g., PPy overlaying the substrate) and on the poly-DND particle (e.g., upright alignment of PPy chain relatively to poly-DND as was discussed in [35]). In this way, differently aligned PPy will interact in a different way with SNOM-IR polarized light resulting in different peak intensities. The possibility of revealing the arrangement of the molecules by the different intensity of SNOM-IR response signal was already shown in [53] and is revealed again in work. Thus, SNOM-IR clearly shows tight interaction between DNDs and PPy, providing confirmation of O-DND/PPy and poly-DND/PPy composites formation. Also, based on SNOM-IR results, different types of bonding with subsequent different PPy arrangement relatively to O-DND and poly-DND can be suggested.

PDS spectra of neat PPy as well as DND/PPy composites reveal optical absorption in a broad visible spectral range. Poly-DND/PPy composite absorbs the most while neat PPy absorbs the least. O-DND/PPy and H-DND/PPy composites have absorption coefficient similar to each other and both are well below absorption coefficient of poly-DND/PPy composite. Although superior optical absorption of poly-DND/PPy composite seems obvious, various factors should be considered before making such conclusion.

DND particles carry larger amount of light-absorbing dye since PPy thickness on substrates nucleated with DNDs of any kind is higher compared to PPy thickness on the bare substrate (see Table 1 and Figure S4 in Supplementary information). Even though the absorption coefficient is independent of material thickness the actual amount of PPy can be different in the given thickness. However, PPy thickness on O-DND is smaller than in the neat PPy layer and yet the O-DND/PPy has larger absorption coefficient in the whole spectrum. There is also different PPy thickness on H-DND and O-DND and yet the absorption coefficient spectra are similar. Contrary, the PPy thickness on H-DND and poly-DND is similar and yet the absorption coefficient
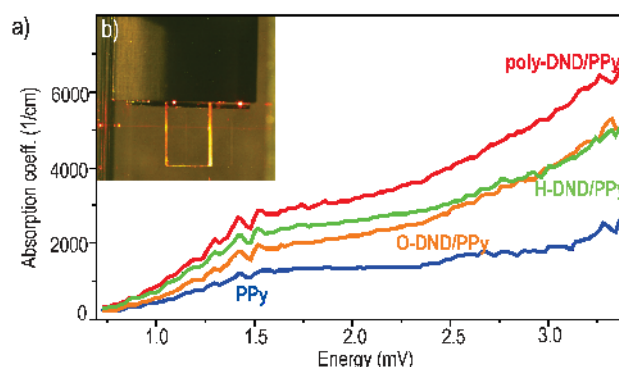

Figure 5. a) Absorption coefficient spectra of composites and PPy reference b) poly-DND/PPy sample during PDS measurement.

differs considerably. The pronounced difference in absorption cannot be only due to scattering effects though, as observed for instance for Si quantum dots.[54] Otherwise, poly-DND/PPy and O-DND/PPy absorption would be similar due to similar DND density of these samples.

Another factor of the different absorption coefficients of the composites and PPy ref can be different electronic states of PPy itself. Although the synthesis process (and chemicals) was the same for all samples, the PPy could be different due to DND effects on the synthesis. According to [31,32] two additional energy levels are introduced into PPy bandgap at mild PPy oxidation, which correspond to bonding and anti-bonding polaron states. With a large extent of PPy oxidation, the quantity of intra-bandgap levels increases and they merge into bands (bipolaron bonding and anti-bonding bands). As a result, PPy oxidation promotes absorption in the infrared region and broadening of the bands in the absorption spectrum due to more possibilities of charge transfer between intra-bandgap bands. Thus, more pronounced absorption in composites compared to pristine PPy can be explained by a larger extent of PPy oxidation in composites due to charge exchange between PPy and DNDs. Poly-DND/PPy with maximum absorption compared to O-DND/PPy and H-DND/PPy might be consisted of PPy in the
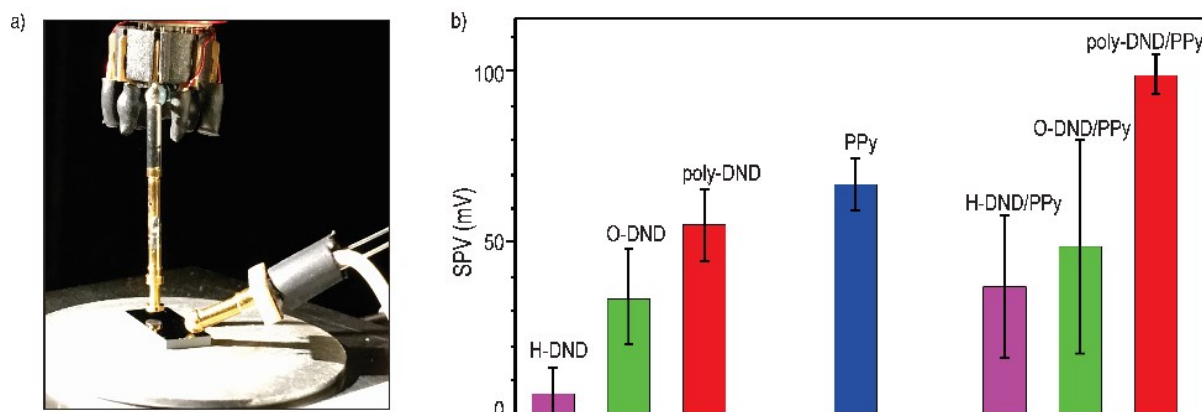

Figure 6. a) Photo of the SKP setup. b) Surface photovoltage of the composites and their references.
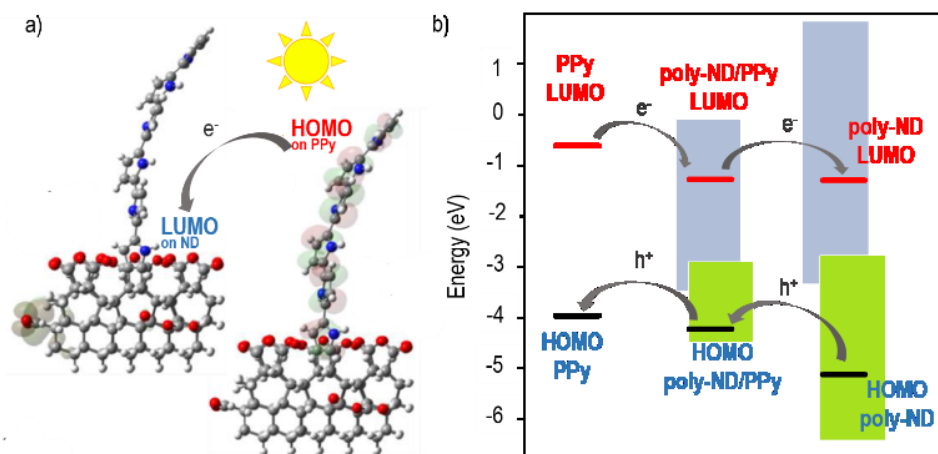
This journal is © The Royal Society of Chemistry 20xx

J. Mater. Chem. A., 2019, 00, 1-3 | 7

Figure7. a) Example of spatial separation of PPy HOMO and ND LUMO. Based on DFT calculations. b) Scheme of HOMO and LUMO energetic levels composite of separate materials and their interface with the most probable charge transfer due to level alignment.

largest oxidation state due to the most pronounced charge exchange between poly-DND and PPy.

The last but not least factor behind the enhanced absorption coefficient of the nanocomposites may be the favourable optoelectronic properties arising at the DND/PPy junction. Theoretical computing (described further below) indicated large variations of energetic bandgap (0.3 - 3.5 eV) at the junction of DND/PPy depending on facet crystallographic orientation, surface chemistry and way of PPy attachment. In our opinion, it is probably the dominating effect behind the enhanced absorption coefficient as it is well correlated with photovoltage measurements by SKP.

The photograph of the SKP setup is shown in Figure 6a. Each sample was contacted sideways by a ball-shaped electrode. SKP probing tip is above the sample. Illumination, when it is necessary, is introduced under an angle from the side. Surface potentials of poly-DND/PPy, O-DND/PPy and H-DND/PPy composites, their references and bare substrates were measured in the dark and under illumination. Surface photovoltages of the samples were then calculated. The highest SPV of the DND/PPy composites was detected on the samples with the p-Si substrate. The SPV values for the reference and composite samples are summarized in Figure 6b. Maximum photovoltage is observed on poly-DND/PPy composite (99±6 mV) compared to O-DND/PPy (49±31 mV) and H-DND/PPy (37 ± 21 mV). SPV of poly-DND/PPy is also larger compared to SPV of pristine PPy (67±8 mV) and pristine poly-DNDs (55±10 mV). H-DND reference sample shows negligible SPV (6±7 mV) and O-DND reference has SPV values of 34±14 mV. The difference between H-DND and O-DND may be explained by cleaning of sp² components and at by passivation of surface states during hydrogenation annealing. The largest positive surface photovoltage detected in poly-DND/PPy compared to all other samples might indicate the largest extent of PPy oxidation by poly-DNDs via withdrawing electrons from PPy chain (in agreement with PDS interpretation above). Noteworthy, SPV of the composites cannot be due to the substrate, because the

annealed p-Si has SPV of the opposite sign (-87±31 mV) compared to the nanocomposites and other reference samples. Theoretical calculations support the experimental results and help us propose a photovoltage generation mechanism in the DND/PPy composites. In the model configuration of poly-DND/PPy composites, where PPy chain grafted covalently to ND and surrounded by oxygen-containing groups, it was observed that HOMO is fully localized on PPy and LUMO fully localized on ND (Figure 7a). In addition, for various oxygen moieties in the poly-DND/PPy models, the energetic levels of PPy, ND and ND-PPy interface are aligned in such a way that it is energetically beneficial for the electrons to be transferred from PPy into ND (Figure 7b). Thus, the maximum and positive SPV observed in the poly-DND/PPy composite is theoretically explained. The calculations also elucidate the role of hydrogen- and oxygen-containing groups on poly-DND surface, namely: PPy grafts via CH groups to poly-DND and hydrogen-bond interaction of the grafted PPy with surrounding CO groups results in the alignment of energy levels of PPy and poly-DND and in the spatial separation of HOMO on PPy and LUMO on poly-DND that favours charge carriers separation between PPy and poly-DND. Poly-DND/PPy as the nanocomposite with the most enhanced absorption coefficient and the highest SPV among all the samples was embedded as an active material into a simple solar cell structure with p-Si as the back electrode and Al as the top electrode. Figure 8a shows IV characteristic curves in the dark and under the illumination of such a solar cell. The inset image (Figure 8b) shows how the IV characteristics of the solar cell with poly-DND/PPy were measured. The characteristics show that the solar cell is indeed functional. The following performance parameters were calculated: open-circuit voltage V_{oc} (0.05V), short circuit current I_{sc} (0.6 uA/cm²), fill factor FF (0.3) and power conversion efficiency η (1E-5%) presented in Figure 8a. They may seem quite low but it is not an optimized device. And yet the performance of solar cell with the poly-DND/PPy composite as active material is better than with the neat PPy layer having two times lower efficiency (see Figure S5 in ESI). Thus, the prototype solar cell with poly-DND/PPy
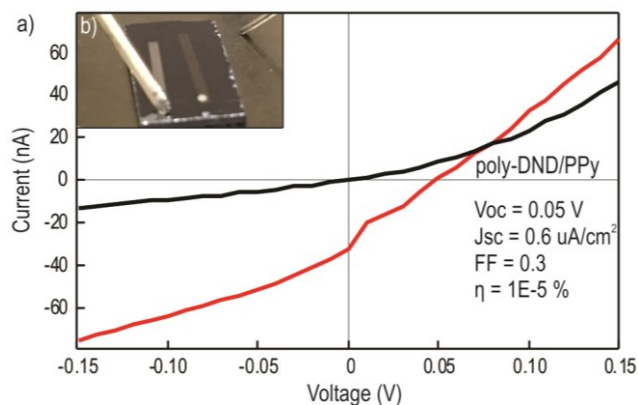
Figure 8. a) IV curves in dark (black) and under solar simulator irradiation (red) of solar cell with poly-DND/PPy composite as an active material. b) Test solar cell picture with connected microelectrodes for IV characterization.

composite demonstrates proof-of-principle as well as provides opportunities for further optimizations (by variation of materials for top/back electrode, finding the optimum thickness of the nanocomposite, interface optimization, etc).

Conclusions

The present work showed that detonation nanodiamonds with various surface chemical groups can be combined with polypyrrole into the novel nanocomposite material. We demonstrated layer-by-layer fabrication technology that is suitable for solar cell fabrication. Formation of the nanocomposite and pronounced interaction between polypyrrole and nanodiamond in such composite were evidenced by changes and new vibrational bands in infrared spectroscopy performed both macroscopically and locally with nanoscale resolution and supported by atomic force microscopy. Moreover, AFM indicated that DNDs with different surface terminations assemble PPy oligomers in different ways. Different PPy alignments relative to DNDs surface might contribute to the different light-harvesting effects of the composites. Study of optical absorption and photovoltage generation revealed that the nanocomposite exhibits a highly enhanced absorption coefficient. The optical absorption of the composite is broad, covering well the visible spectrum from infrared to near UV (1 eV to 3.5 eV). Also, the photovoltage was enhanced compared to pristine materials. The positive polarity of SPV shows that DNDs acts as an electron acceptor and leave the positive charge on PPy molecules. Theoretical atomic-scale DFT calculations elucidated the mechanism of the photovoltage generation by exciton dissociation where electrons are indeed transferred from PPy into nanodiamond. Polyfunctional nanodiamond with both oxygen and hydrogen surface groups appeared the most favourable for photovoltaics. The assembled prototype solar cell proved the functionality of the concept. Due to the general non-toxicity of nanodiamond, its chemical stability and availability in large quantities, these results may

open prospects for a breakthrough in the field of organic photovoltaics.

Conflicts of interest

There are no conflicts to declare.

Acknowledgements

References

1   A. Mahmood, J.-Y. Hu, B. Xiao, A. Tang, X. Wang and E. Zhou, *J. Mater. Chem. A*, 2018, **6**, 16769–16797.
2   P. Cheng and X. Zhan, *Chem. Soc. Rev.*, 2016, **45**, 2544–2582.
3   S. Liu, C. Li, X. Xu, P. You, N. Wang, J. Wang, Q. Miao and F. Yan, *J. Mater. Chem. A*, , DOI:10.1039/C9TA02636C.
4   D. Liu, K. Zhang, Y. Zhong, C. Gu, Y. Li and R. Yang, *J. Mater. Chem. A*, 2018, **6**, 18125–18132.
5   T. M. Barnes, J. D. Bergeson, R. C. Tenent, B. A. Larsen, G. Teeter, K. M. Jones, J. L. Blackburn and J. van de Lagemaat, *Appl. Phys. Lett.*, 2010, **96**, 243309.
6   S. Günes, H. Neugebauer and N. S. Sariciftci, *Chem. Rev.*, 2007, **107**, 1324–1338.
7   A. Nagata, O. K. U. Takeo, K. Kikuchi, A. Suzuki, Y. Yamasaki and E. Osawa, *Prog. Nat. Sci. Mater. Int.*, 2010, **20**, 38–43.
8   V. Švrček, D. Mariotti, T. Nagai, Y. Shibata, I. Turkevych and M. Kondo, *J. Phys. Chem. C*, 2011, **115**, 5084–5093.
9   C.-Y. Liu, Z. C. Holman and U. R. Kortshagen, *Nano Lett.*, 2009, **9**, 449–452.
10   M. Grätzel, *Nature*, 2001, **414**, 338–344.
11   H. Kozak, Z. Remes, J. Houdkova, S. Stehlik, A. Kromka and B. Rezek, *J. Nanoparticle Res.*, , DOI:10.1007/s11051-013-1568-7.
12   V. Vaijayanthimala, Y.-K. Tzeng, H.-C. Chang and C.-L. Li, *Nanotechnology*, 2009, **20**, 425103.
13   A. Schrand, S. A. C. Hens and O. Shenderova, *Crit. Rev. Solid State Mater. Sci.*, 2009, **34**, 18–74.
14   A. Krueger and D. Lang, *Adv. Funct. Mater.*, 2012, **22**, 890–906.
15   J. Čermák, B. Rezek, V. Cimrová, D. Výprachtický, M. Ledinský, T. Mates, A. Fejfar and J. Kočka, *Phys. Status Solidi RRL – Rapid Res. Lett.*, 2007, **1**, 193–195.
16   Y. L. Zhong, A. Midya, Z. Ng, Z.-K. Chen, M. Daenen, M. Nesladek and K. P. Loh, *J. Am. Chem. Soc.*, 2008, **130**, 17218–17219.
17   B. Rezek, J. Čermák, A. Kromka, M. Ledinský, P. Hubík, J. J. Mareš, A. Purkrt, V. Cimrová, A. Fejfar and J. Kočka, *Nanoscale Res. Lett.*, 2011, **6**, 238.
18   P. S. Abthagir and R. Saraswathi, *J. Appl. Polym. Sci.*, 2001, **81**, 2127–2135.
19   T. V. Vernitskaya and O. N. Efimov, *Russ. Chem. Rev.*, 1997, **66**, 443–457.

This journal is © The Royal Society of Chemistry 20xx

J. Mater. Chem. A., 2019, **00**, 1-3 | **9**

20 A. Kausaite-Minkstimiene, V. Mazeiko, A. Ramanaviciene and A. Ramanavicius, *Colloids Surf. Physicochem. Eng. Asp.*, 2015, **483**, 224–231.

21 K. Leonavicius, A. Ramanaviciene and A. Ramanavicius, *Langmuir*, 2011, **27**, 10970–10976.

22 S. P. Armes, *Synth. Met.*, 1987, **20**, 365–371.

23 T. H. Chao and J. March, *J. Polym. Sci. Part Polym. Chem.*, 1988, **26**, 743–753.

24 H. V. R. Dias, M. Fianchini and R. M. G. Rajapakse, *Polymer*, 2006, **47**, 7349–7354.

25 M. Satoh, K. Kaneto and K. Yoshino, *Synth. Met.*, 1986, **14**, 289–296.

26 J. M. Pringle, J. Efthimiadis, P. C. Howlett, J. Efthimiadis, D. R. MacFarlane, A. B. Chaplin, S. B. Hall, D. L. Officer, G. G. Wallace and M. Forsyth, *Polymer*, 2004, **45**, 1447–1453.

27 P.-C. Wang and J.-Y. Yu, *React. Funct. Polym.*, 2012, **72**, 311–316.

28 M. J. L. Santos, A. G. Brolo and E. M. Girotto, *Electrochimica Acta*, 2007, **52**, 6141–6145.

29 F. Genoud, M. Guglielmi, M. Nechtschein, E. Genies and M. Salmon, *Phys. Rev. Lett.*, 1985, **55**, 118–121.

30 J. Kaufman, N. Colaneri, C. Scott and G. B. Street, *Phys. Rev. Lett.*, 1984, **53**, 1005–1008.

31 J. L. Bredas, B. Themans and J. M. Andre, *Phys. Rev. B*, 1983, **27**, 7827.

32 S. Stehlik, M. Varga, M. Ledinsky, V. Jirasek, A. Artemenko, H. Kozak, L. Ondic, V. Skalova, G. Argentero, T. Pennycook, J. C. Meyer, A. Fejfar, A. Kromka and B. Rezek, *J. Phys. Chem. C*, 2015, **119**, 27708–27720.

33 S. Stehlik, M. Varga, P. Stenclova, L. Ondic, M. Ledinsky, J. Pangrac, O. Vanek, J. Lipov, A. Kromka and B. Rezek, *ACS Appl. Mater. Interfaces*, 2017, **9**, 38842–38853.

34 D. Nečas, P. Klapetek, Gwyddion: an open-source software for SPM data analysis, *Cent. Eur. J. Phys.*, 2012, **10(1)**, 181-188.

35 D. Miliaieva, S. Stehlik, P. Stenclova and B. Rezek, *Phys. Status Solidi A*, 2016, **213**, 2687–2692.

36 F. Huth, M. Schnell, J. Wittborn, N. Ocelic and R. Hillenbrand, *Nat. Mater.*, 2011, **10**, 352–356.

37 F. Keilmann and R. Hillenbrand, *Philos. Transact. A Math. Phys. Eng. Sci.*, 2004, **362**, 787–805.

38 F. Huth, A. Govyadinov, S. Amarie, W. Nuansing, F. Keilmann and R. Hillenbrand, *Nano Lett.*, 2012, **12**, 3973–3978.

39 C. Westermeier, A. Cernescu, S. Amarie, C. Liewald, F. Keilmann and B. Nickel, *Nat. Commun.*, , DOI:10.1038/ncomms5101.

40 Z. Remes, O. Babchenko, M. Varga, J. Stuchlik, V. Jirasek, V. Prajzler, P. Nekvindova and A. Kromka, *Thin Solid Films*, 2016, **618**, 130–133.

41 B. Dzurňák, F. Trojánek, J. Preclíková, A. Kromka, B. Rezek and P. Malý, *Diam. Relat. Mater.*, 2011, **20**, 1155–1159.

42 S. Zhao and K. Larsson, *J. Phys. Chem. C*, 2014, **118**, 1944–1957.

43 Y. Tian and K. Larsson, *J Material Sci Eng.*, 2019, **8(1)**, 506.

44 S. Stehlik, M. Varga, M. Ledinsky, D. Miliaieva, H. Kozak, V. Skalova, C. Mangler, T. J. Pennycook, J. C. Meyer, A. Kromka and B. Rezek, *Sci. Rep.*, 2016, **6**, srep38419.

45 P. Matunová, V. Jirásek and B. Rezek, *Phys. Status Solidi A*, 2016, **213**, 2672–2679.

46 P. Matunová, V. Jirásek and B. Rezek, *Phys. Chem. Chem. Phys.*, 2019, DOI:10.1039/C8CP07622G.

47 S. Chiesa and M. J. Rossi, *Atmospheric Chem. Phys.*, 2013, **13**, 11905–11923.

48 J. P. Beck, M.-P. Gaigeot and J. M. Lisy, *Phys. Chem. Chem. Phys.*, 2013, **15**, 16736–16745.

49 S. Valtera, J. Prokeš, J. Kopecká, M. Vrňata, M. Trchová, M. Varga, J. Stejskal and D. Kopecký, *RSC Adv.*, 2017, **7**, 51495–51505.

50 E. R. Cordeiro, A. W. C. Fernandes, A. F. C. Pereira, M. M. da Costa, M. L. F. Nascimento, H. P. de Oliveira, E. R. Cordeiro, A. W. C. Fernandes, A. F. C. Pereira, M. M. da Costa, M. L. F. Nascimento and H. P. de Oliveira, *Quím. Nova*, 2015, **38**, 1075–1079.

51 T. Petit and L. Puskar, *Diam. Relat. Mater.*, 2018, **89**, 52–66.

52 S. Valtera, J. Prokeš, J. Kopecká, M. Vrňata, M. Trchová, M. Varga, J. Stejskal and D. Kopecký, *RSC Adv.*, 2017, **7**, 51495–51505.

53 I. Amenabar, S. Poly, W. Nuansing, E. H. Hubrich, A. A. Govyadinov, F. Huth, R. Krutokhvostov, L. Zhang, M. Knez, J. Heberle, A. M. Bittner and R. Hillenbrand, *Nat. Commun.*, 2013, **4**, 2890.

54 H. Sugimoto, Y. Ozaki and M. Fujii, *ACS Appl. Mater. Interfaces*, 2017, **9**, 19135–19142.

Nanodiamond surface chemistry controls assembly of organic dye and photovoltage

Daria Miliaieva[a,b,*], Petra Matunova[a,b], Jan Cermak[a], Stepan Stehlik[a], Adrian Cernescu[c], Zdenek Remes[a], Pavla Stenclova[a] , Bohuslav Rezek[a,b]

[a] Institute of Physics, Czech Academy of Sciences, Cukrovarnická 10, Prague 6, Czech Republic
[b] Faculty of Electrical Engineering, Czech Technical University, Technická 2, Prague 6, Czech Republic
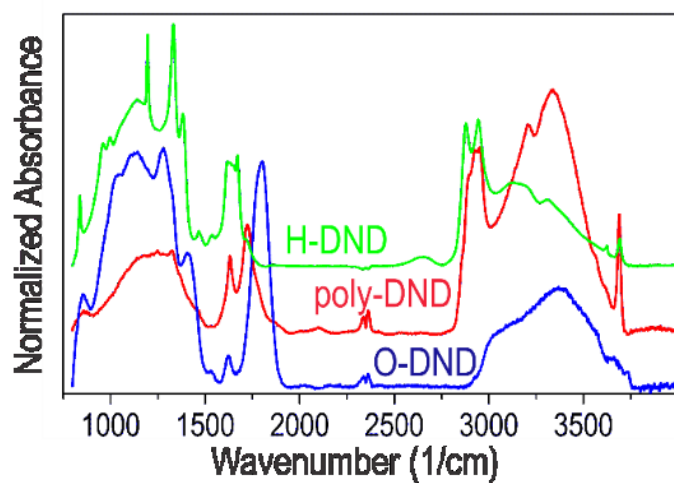[c] Neaspec GmbH,Bunsenstrasse 5,82152 Planegg,Germany

Figure S1. GAR-FTIR spectra of H-DND, poly-DND and O-DND references.

a)   poly-DND ref   poly-DND/PPy

Z scale   12 nm   Z scale   12 nm

b)   H-DND ref   H-DND/PPy

Z scale   12 nm   Z scale   12 nm

c)   O-DND ref   O-DND/PPy
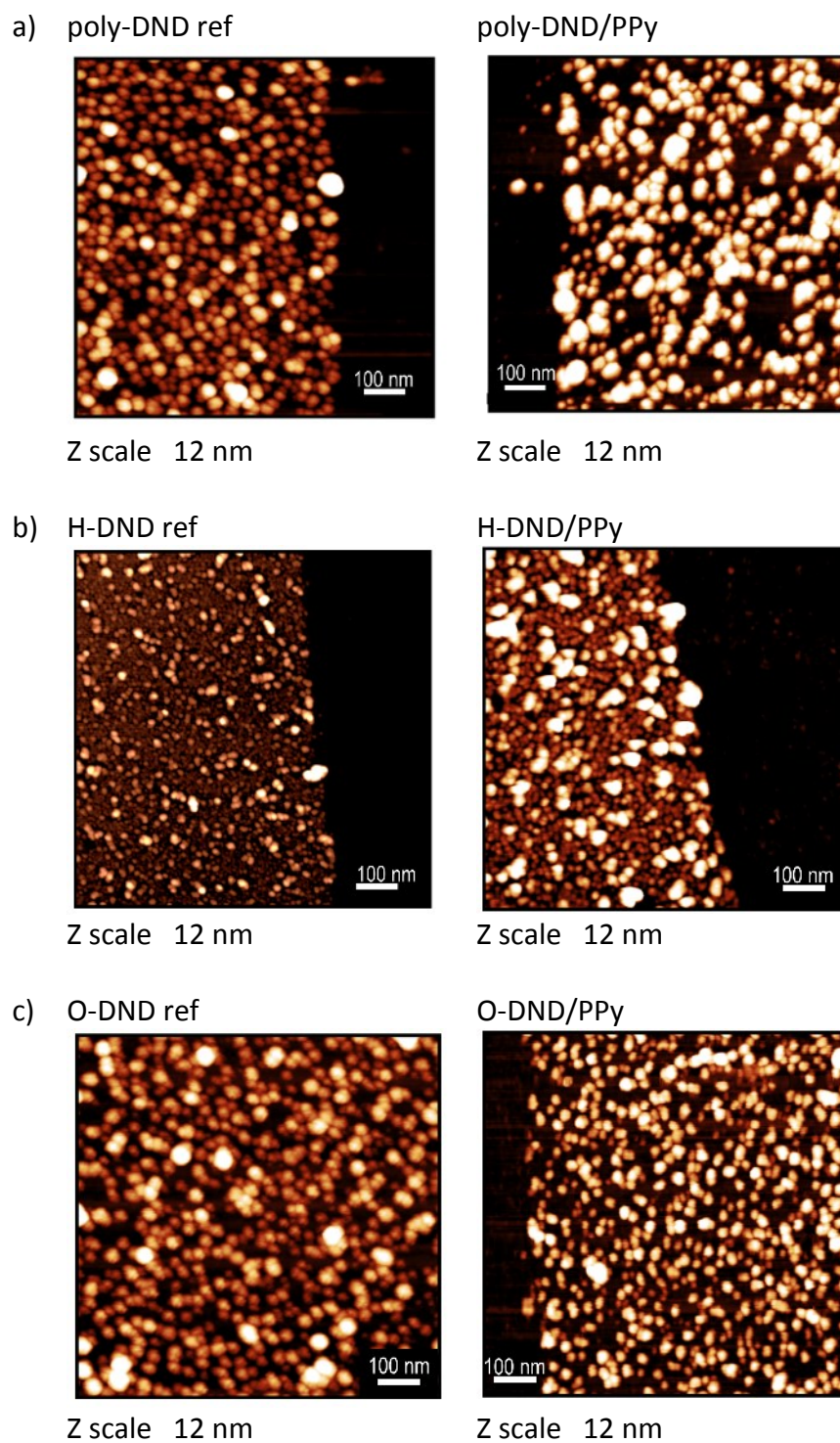

Z scale   12 nm   Z scale   12 nm

Figure S2. AFM morphology images of DND reference particles along with DND/PPy composites. The exposed substrate is at the reference zero height.
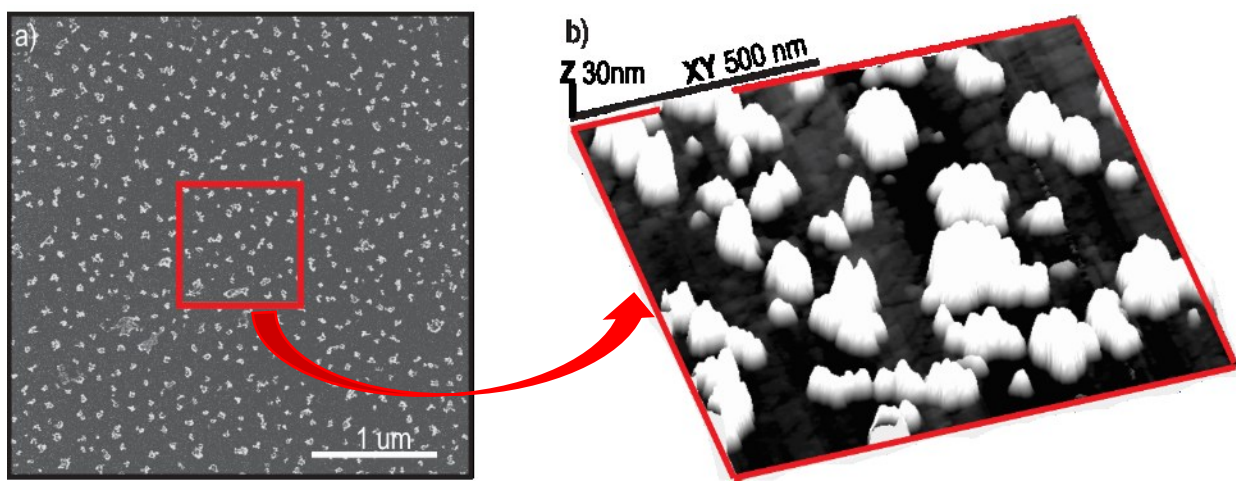
Figure S3. Low-density coverage of silicon substrate by poly-DND agglomerates (average size 30 nm) revealed by (a) SEM (b) AFM.
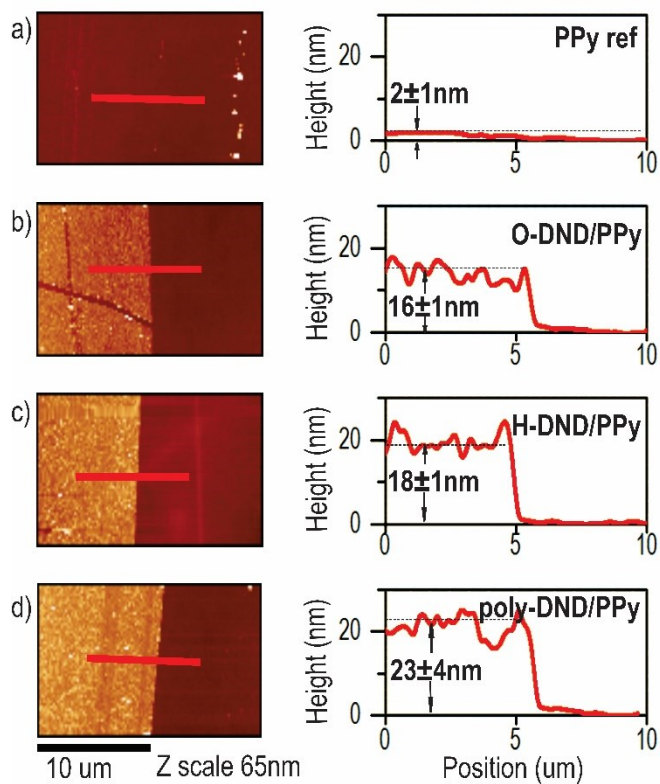
Figure S4. AFM images of the samples on the border with exposed bare glass substrate and corresponding height cross-sections of a) PPy reference b) O-DND/PPy c) H-DND/PPy d) poly-DND/PPy.
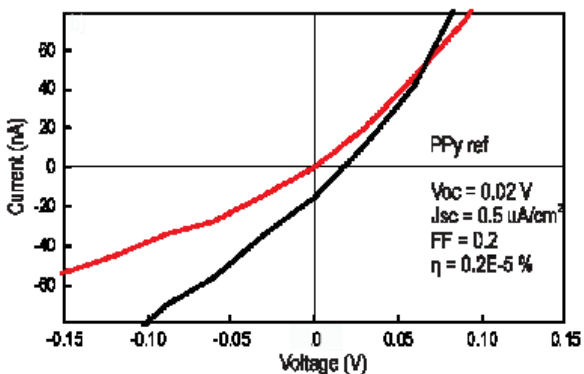

Figure S5. IV curves in dark (black) and under solar simulator irradiation (red) of solar cell with PPy reference as an active material.

physica status solidi a
www.pss-a.com
applications and materials science

**Part of Topical Section on
Recent Advances in Diamond Science and Technology**

Synthesis of polypyrrole on nanodiamonds with hydrogenated and oxidized surfaces

Daria Miliaieva[*,1,2], Stepan Stehlik[1], Pavla Stenclova[1], and Bohuslav Rezek[1,2]

[1] Institute of Physics ASCR, Cukrovarnicka 10, Prague 6, Czech Republic
[2] Faculty of Electrical Engineering, Czech Technical University, Technicka 2, Prague 6, Czech Republic

[*] Corresponding author: e-mail miliaieva@fzu.cz, Phone: +420220318433, Fax: +420233343184

Composite nanoparticles of detonation nanodiamond (DND) and polypyrrole (PPy) were produced in colloidal solution and on surfaces by wet chemical process. Changes of vibrational bands (in particular $>C=O$ and C–H) in Fourier-transform infrared spectroscopy revealed the DND/PPy composite formation and tight interaction of PPy with hydrogenated DND (H-DND) and oxidized DND (O-DND). Atomic force microscopy showed uniform PPy coating but different PPy thickness on H-DND (7.0 nm) and O-DND (3.5 nm). These results suggest different bonding nature and arrangement of PPy on H-DND and O-DND surfaces.

1 Introduction Semiconducting conjugated polymers are considered as a promising alternative to the traditional solar cell materials due to narrow band gap, broad solar spectrum absorption, superior charge transfer, mechanical flexibility, and less expensive fabrication [1]. To design an organic-based photovoltaic system, polymer as a donor of electrons should be combined (just mixed or chemically grafted) with an acceptor of electrons so the free charges could be generated. Different forms of carbon are usually used as electron acceptors in combination with the polymers.

Blends of fullerene derivatives, such as [6,6]-phenyl-C_{61}-butyric acid methyl ester ($PC_{60}BM$) and its analog [6,6]-phenyl-C_{71}-butyric acid methyl ester ($PC_{70}BM$), with semiconductive conjugated polymer poly-3-hexylthiophene (P3HT) have been extensively studied [2, 3]. Record efficiency of 7.4% for fullerene-based blends was achieved in the blend of indene-C_{60}-bisadduct (ICBA) and P3HT [4]. High synthetic cost, limited optical absorption, poor bandgap tunability, and morphological instability of commonly used fullerenes push forward research on the alternatives of fullerenes for light-harvesting blends [5].

Single wall carbon nanotubes (SWCNT) may be used for fabrication of the blend with a polymer for photovoltaic applications due to their excellent transport properties and ability to quench the photolumenescence of polymer [1]. The highest efficiency 0.72% was reported for the composite of SWCNT coated with the ordered layer of P3HT [6].

Graphene having high electrical conductivity and charge mobility ($\sim10^4\,cm^2\,V^{-1}\,s^{-1}$ at room temperature) while being transparent in visible region is a suitable material for applications in optoelectronic devices as well [1]. Liu et al. [7] fabricated the mixture of graphene, functionalized by phenyl isocyanate, and P3HT with power conversion efficiency of 1.1% (compared to pristine P3HT efficiency of 0.005%).

Bulk diamond interface with the semiconducting conjugated polymer polypyrrole (PPy) was also shown to provide facile exciton dissociation [8]. This property of the diamond-PPy composite is beneficial for free charge generation. Considering good conductivity of PPy [9] and its ability to absorb visible light [10], diamond-PPy composite could be a valuable, light-harvesting component for photovoltaic devices. At the same time, covalent bond detected between hydrogenated bulk diamond and PPy [11] could provide strong interaction and stabilization between the components of the composite.

If bulk diamond in the diamond-PPy composite is substituted with the detonation nanodiamond (DND), the cost of composite fabrication technology would decrease greatly because of inexpensive DNDs production [12]. DNDs are chemically stable [13], have rich surface chemistry, and established techniques for changing the surface termination and size by processing in large volumes [14]. This opens the way to use wet chemistry for DND modification and consequently could decrease the production cost compared to electrochemical methods used so far to prepare diamond/nanodiamond composites with PPy [15]. In addition, due to the short exciton diffusion length of 10 nm in organic polymers [16] high surface-to-volume ratio of nanodiamonds (ND) may be beneficial. Moreover, DND/PPy composite may also be a promising material for biosensing. Owing to the amine group in pyrrole (Py) ring, the composite might be used for peptides sensing [17].

Few reports have appeared in the recent years about ND/PPy composite fabrication [15, 18]. Ashassi-Sorkhabi et al. [15] fabricated ND/PPy composite electrochemically for corrosion protection applications. Being environmentally stable and non-toxic [9], PPy was used as a physical barrier against the corrosion. NDs as nanofillers of PPy made the structure of the material denser and blocked the pores in PPy as evidenced by SEM [15]. Due to such morphology, ND/PPy composite provided enhanced anticorrosion protection compared to pristine PPy coating. Ashraf et al. [18] fabricated the composites in which as received and carboxylated NDs were overlayed with multilayers of conjugated polymers (polyaniline, polypyrrole, polyazopyridine). An increase in the thermal stability and heat resistance was detected in the composites compared to the pristine conjugated polymers. In addition, functionalization of ND increased the conductivity of the final composite due to the stronger interaction between functionalized ND and the conjugated polymer. The nature of such interaction as well as the effect of ND surface termination on the ND-polymer interaction have not been investigated yet. However, knowing the bonding nature in ND/polymer composites is crucial for understanding their properties as well as for their applications.

In this work, with view to the prospective application in photovoltaics, we developed novel wet-chemical technology to fabricate DND/PPy composites. By using infrared spectroscopy and atomic force microscopy (AFM), we characterized DND/PPy properties, namely the interaction between PPy and DND of different terminations (hydrogenated and oxidized), and provided a structural model of such composite material.

2 Experimental

2.1 Materials
DNDs were manufactured by Lingyun Granda Nano (China) and distributed by New Metals and Chemicals (Japan). Fourier-transform infrared spectroscopy (FTIR) of as-received DNDs showed pronounced peak at 2800–3000 cm^{-1} which corresponds to C–H surface groups. Zeta potential of as-received DNDs is positive, $+41$ mV, as measured by Malvern Zetasizer. Therefore, to simplify the notation and emphasize the presence of C-H groups as-received DNDs will be referred to as H-DND further in the text. O-DNDs were obtained from H-DND by air annealing at 490 °C for 10 min [7]. Zeta potential of annealed in such a way DNDs is -39 mV. Hydrochloric acid (HCl, 37%) and pyrrole (98%) were purchased from Sigma–Aldrich (USA) and used as received.

2.2 Sample preparation procedure
In order to overcome the problem of determining the right proportion of DNDs, pyrrole and hydrochloric acid for wet chemistry synthesis, the technology inspired by Ref. [19] was applied. The main stages of the procedure could be described as: (i) dispersing and simultaneous soaking of DND particles in Py monomer; (ii) removing non-adsorbed Py from the reaction medium; (iii) polymerizing the adsorbed Py on DND particles. The same procedure was applied to H-DND and O-DND.

In the first step, 30 mg of DND powder were sonicated for 1 h in 2 ml of Py using a Hielscher 200W ultrasound horn to properly disperse DNDs in Py. The resulting DND/Py colloid was then centrifuged for 1 h at $\sim$13 000$\times g$ (Eppendorf mini plus) to remove the aggregated DNDs. After the centrifugation, 1 ml of supernatant was pipetted out of the test-tube. The parameters for sonication and centrifugation were the same as described by Stehlik et al. [20]. In Ref. [20], such procedure in water resulted in a colloidal solution of DNDs with mean size of $\sim$5 nm as determined by AFM. The composite mixtures of H-DND and O-DND after step 1 are referred to as H-DND/Py-1 and O-DND/Py-1, respectively.

In the second step, 1 ml of deionized water was added to 1 ml of the supernatant from the first step. Two-layered solution was formed with the yellowish Py layer on the top (due to lower Py density of 0.97 g ml^{-1}). The solution was left still for 24 h so that DND/PPy particles would sediment from Py down to the water layer. After 24 h, the bottom water layer was carefully pipetted out and processed in the step 3 of the procedure. The composite mixtures of H-DND and O-DND after step 2 are referred to as H-DND/Py-2 and O-DND/Py-2, respectively.

In the third step, the solution from step 2 was mixed with 0.3 M HCl solution in the proportion of 1:9. HCl solution plays a role of the initiator and catalyst of Py polymerization reaction [21]. The mixture was stirred for 24 h with the magnetic stirrer at 250 rpm for uniform coating of the particles with PPy. The composite mixtures of H-DND and O-DND with PPy obtained after step 3 are referred to as H-DND/PPy-3 and O-DND/PPy-3, respectively.

For preparation of PPy reference solution, all steps of the procedure were kept the same except the addition of DND powder in the reaction mixture. O-DND and H-DND reference solutions were prepared by sonication of 0.5 mg of DND powder in 1 ml of deionized water for 15 min.

Products of each step were analyzed by FTIR (see the details below).

To prepare samples for AFM measurements, the PPy modification was performed directly on nucleated with DNDs substrates to avoid possible agglomeration of the DNDs/PPy composite particles during their deposition on the substrate. Silicon (Si) substrates were at first nucleated with H–DNDs by sonication of the substrate for 15 min in H-DND water supernatant prepared as per Ref. [20]. After that one of the substrates was annealed in air at 490 °C for 10 min in order to oxidize the surface of DNDs. Substrates, nucleated with H-DND and annealed DND (O-DND), were immersed into Py solution and held there for 24 h without air and light exposure. Subsequently, the substrates were immersed into 0.3 M HCl solution and left there for 24 h. Afterwards, the substrates were rinsed with deionized water, dried, and scanned with AFM. The above procedure for nucleated substrates is analogous to three-step procedure for the composite fabrication in solution.

2.3 Sample characterization techniques Composition of DND/Py and DND/PPy composites and its changes after each step of processing were characterized by grazing angle reflectance Fourier transform infrared (GAR-FTIR) spectroscopy. FTIR spectra were measured using N_2-purged Thermo Nicolet 8700 spectrometer equipped with KBr beam splitter and MCT detector cooled by liquid nitrogen. 100–150 µl of the solutions were dropcasted on Au mirrors and dried at 100 °C for 2 min just prior to the GAR-FTIR measurement. The optical absorbance was calculated in the standard absorbance units as $A = -\log(R/R_0)$, where R is the reflectance of analyzed material and R_0 is the reflectance of the clean Au mirror prior to the analyte application. In all cases, a spectrum represents an average of 128 scans recorded with a resolution of $4\,cm^{-1}$. Each spectrum was normalized to the intensity of the strongest peak in the spectrum.

AFM (NTMDT Ntegra) morphology of the reference H-DND and O-DND nucleated substrates as well as the substrates after the final step of composite formation was measured in an attractive force regime using Si cantilevers of 300 kHz resonance frequency. To evaluate the thickness of PPy layer, the height of DNDs/PPy composites should be measured relatively to the bare Si substrate. To expose the bare substrate so-called "nanoshaving" [22] was performed that is AFM scanning in contact mode with applied contact force (in our case 10 nN).

Six scans were performed in AFM contact mode for DNDs/PPy composites followed by non-contact scans across the nanoshaved areas. For the DND reference samples, only AFM in non-contact mode was performed (6 scans) as there was large enough area of bare Si-substrate used as a reference for particles' height evaluation. Mean particle height versus substrate and characteristic autocorrelation length (L_x) were evaluated using AFM software. Thickness of PPy on DNDs, h_{PPy}, was calculated by the following equation:

$$h_{PPy} = h_{DND/PPy} - h_{DND}$$
$$+ \sqrt{SD_{DND}^2 + SD_{DND/PPy}^2}, \qquad (1)$$

where $h_{DND/PPy}$ is average height of DND/PPy composite particles evaluated from the samples nanoshaved in the contact regime, h_{DND} is average height of DND particles determined from the non-contact scanning of pristine DND samples, SD_{DND} is standard deviation (root mean square) of the height values of pristine DND particles, and $SD_{DND/PPy}$ is standard deviation (root mean square) of the height values of DND/PPy composite particles.

3 Results Figure 1 shows FTIR spectra of the composites after each step of the process and they are compared to the spectra of reference DNDs, Py, and PPy.

FTIR spectra in Fig. 1 show that a characteristic feature of H-DND, the band of C–H vibrations in the region of 2800–3000 cm^{-1}, is clearly pronounced in the initial H-DNDs, and its intensity decreased dramatically in H-DND composite spectra in all processing steps. From Fig. 1 it is also seen that the peak of carbonyl group, which is present in the reference O-DND spectrum at 1800 cm^{-1}, is shifted to 1720 cm^{-1} in O-DND composite spectra. In the final composites, H-DND/PPy-3 and O-DND/PPy-3,
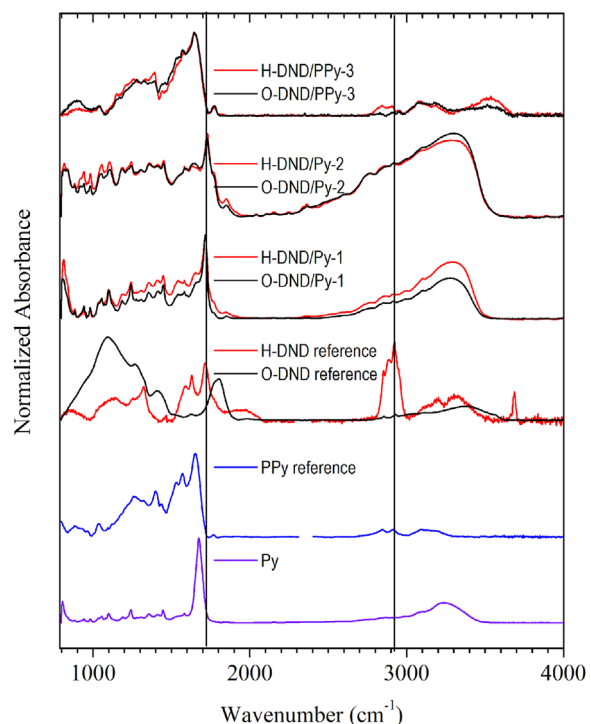

Figure 1 FTIR spectra of the composites after each process step are compared to the reference DNDs, Py, and PPy spectra. The vertical lines denote peaks corresponding to carbonyl (>C=O) and hydrogen-containing (C–H) groups and show the evolution of these groups in the composite spectra compared to the reference DNDs.
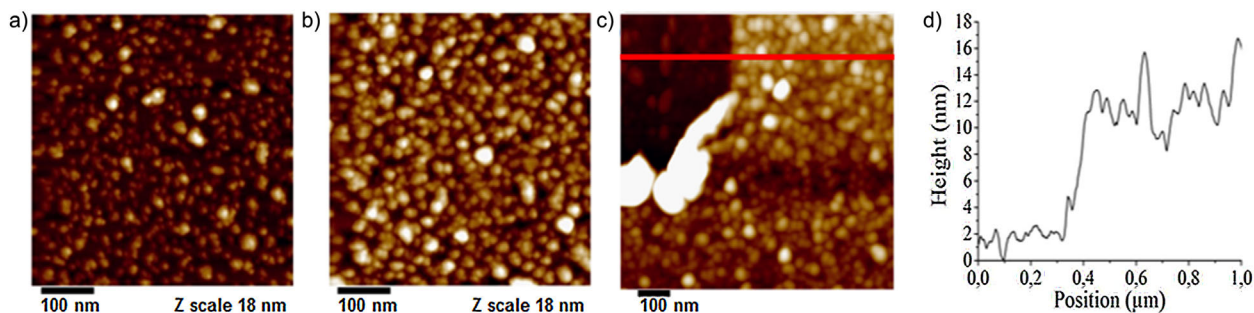
Figure 2 AFM topography images of substrates with (a) H-DND, (b) H-DND/PPy, (c) H-DND/PPy which was locally nanoshaved in AFM contact mode (shaved area is in the top left corner of the image). (d) Cross-sectional height profile denoted by the red line in the image (c).

the peaks that could be attributed to DNDs are either merged with PPy peaks or disappeared. However, the spectra of H-DND/PPy-3 and O-DND/PPy-3 are not the same as the PPy reference spectrum. There are two distinct features: (i) newly appeared band at $3520\,cm^{-1}$ that can be attributed to the vibrations of NH groups in pyrrole rings [23] of PPy; (ii) different appearance of peaks and bands in the $800–1800\,cm^{-1}$ region.

Figures 2 and 3 show AFM images of DNDs and DNDs/PPy particles on Si substrates as well as images of the locally nanoshaved DNDs/PPy samples. AFM revealed negligible change (within error bar) in roughness prior and after the PPy process on both H-DNDs and O-DNDs (see Table 1). Yet L_x values of autocorrelation function have increased after the modification process, in agreement with different appearance of DNDs and DNDs/PPy particles in AFM morphology images. Higher L_x values for O-DND/PPy compared to H-DND/PPy could be due to some non-specifically adsorbed PPy around O-DNDs. Equation (1) was used to calculate the thickness of PPy on the respective DNDs. The obtained values including error range are summarized in Table 1. The main result is that PPy coating on H-DNDs is about twice thicker than on O-DND (7.0 vs. 3.4 nm). The significance of difference in the average heights of H-DND/PPy and O-DND/PPy was

evaluated via analysis of variance (ANOVA). P-value is equal to 0.001 (below the limit of 0.05) and indicates that there is a statistically significant difference between the thickness of PPy on O-DND/PPy and H-DND/PPy composites.

4 Discussion Comparison of FTIR spectra of Py (monomer) reference and DNDs after the first (Py adsorption) step in Fig. 1 shows that adsorption of Py on O-DND as well on H-DND particles occurred during the first step of the modification process. Mutual interaction between O-DND and Py in O-DND/Py-1 is indicated by several FTIR features in Fig. 1: (i) shift of the peak from $1800\,cm^{-1}$ in reference O-DND, which is attributed to carbonyl group (most likely ester) [24], to $1720\,cm^{-1}$ in O-DND/Py-1 (carbonyl peak from carboxylic acid group [24]); (ii) pronounced decrease of the intensity in $1100–1500\,cm^{-1}$ region in O-DND/Py-1 compared to the reference O-DND. The region corresponds to C–O–C vibrations (along with OH and CH deformation vibrations and C–C stretching vibrations) [24] and decrease of the band intensity could be due to ester rearrangement.

In H-DND/Py-1 spectrum, the triple peak at $2800–3000\,cm^{-1}$, which corresponds to C–H vibrations and which is found in the reference H-DND, diminishes
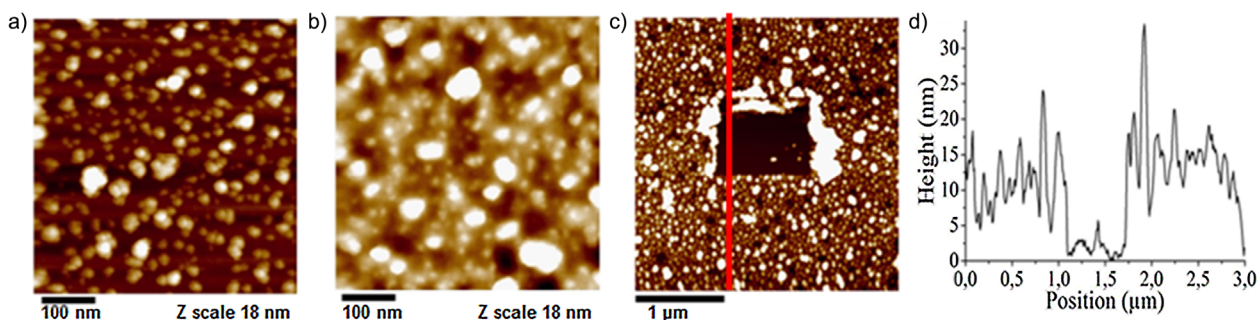

Figure 3 AFM topography images of substrates with (a) O-DND, (b) O-DND/PPy, (c) O-DND/PPy which was locally nanoshaved in AFM contact mode (shaved area is the rectangle in the center of the image). (d) Cross-sectional height profile denoted by the red line in the image (c).

Table 1 Summary of AFM morphology data on substrates with H-DND/PPy, O-DND/PPy, and respective reference (initial) substrates with H-DNDs and O-DNDs.

sample	mean particle height (nm)	roughness (nm)	L_x (nm)	thickness of PPy (nm)
H-DND	3.6 ± 0.5.	2.9 ± 0.4	10.0 ± 2.0	
H-DND/PPy	10.6 ± 2.0	3.1 ± 0.5	13.8 ± 2.5	7.0 ± 2.1
O-DND	3.1 ± 0.5	2.8 ± 0.3	11.5 ± 2.6	
O-DND/PPy	6.5 ± 0.9	2.4 ± 0.2	17.2 ± 2.8	3.4 ± 1.0

considerably. This suggests adsorption of Py on H-DND through C-H bonds.

Thereby, the most distinct features that make difference in FTIR reference spectra of H-DND and O-DND (peaks of C–H and >C=O vibrations, respectively) disappeared after Py adsorption on the particles and the spectra of H-DND/Py-1 and O-DND/Py-1 look similar. After the step 2, at which the medium for DNDs was changed from Py to water, FTIR shows that DND particles did not change compared to the particles after the step 1 except for more pronounced –OH band in H-DND/Py-2 and O-DND/Py-2, which may be related to larger amount of adsorbed water on the composite nanoparticles. Similarity of spectra of composites after the steps 1 and 2, thus, shows that Py remains adsorbed on DNDs after particles' medium was changed from Py to water.

Note that in the first and second steps of the experiment there is no Py polymerization initiated; DNDs are covered with adsorbed Py (with perhaps only negligible amount of PPy spontaneously formed in the solution).

After the step 3, when HCl was added to H-DND/Py-2 and O-DND/Py-2 particles, both spectra of O-DND/PPy-3 and H-DND/PPy-3 differ from the spectra of the step 2 composites as well as the reference PPy spectrum. This indicates mutual interaction between DNDs and PPy in O-DND/PPy-3 and H-DND/PPy-3. Thus, we can assume that in the final composites O-DND and H-DND particles are coated with PPy.

The FTIR spectra of O-DND/PPy-3 and H-DND/PPy-3 also differ mutually: the bands in 1600–4000 cm^{-1} region are more pronounced for H-DND/PPy-3. According to Lei et al. [25], the difference in 1600–4000 cm^{-1} region results from the different level of PPy doping. This could be due to different type of bonding (chemisorption or physisorption) in H-DND/PPy-3 and O-DND/PPy-3 or different interaction of merely physisorbed PPy with particular type of DNDs (chemisorption of PPy to O-DND is unlikely to occur [8, 11]).

To clarify the processes that may occur in the step 3, AFM data (Table 1) are valuable. The thickness of PPy layer on H-DNDs and O-DNDs as revealed by AFM is different (7.0 ± 2.1 vs. 3.4 ± 1.0 nm). At the same time, the surface RMS roughness remained about the same compared to the pristine DNDs. On the other hand, AFM morphology

images and L_x values showed that lateral features increased in size. All these facts indicate that both H-DNDs and O-DNDs are uniformly coated by PPy after the modification process and the substrate is coated by PPy as well.

The difference in PPy thickness on H-DND and O-DND could be due to several reasons. PPy chain length in H-DND/PPy-3 and O-DND/PPy-3 could be different. As polymerization of Py was governed by HCl acid only (in the reference solutions with DNDs and Py and no HCl acid there was observed no Py polymerization) and the amount of acid was equal for preparation of both H-DND/PPy-3 and O-DND/PPy-3, then the PPy chain length should be similar in the final composites.

Different extent of physisorption of Py on H-DND and O-DND in the step 1 could be another reason for different PPy thickness. This possibility is excluded by (i) similar size and zeta potential magnitude of H-DND and O-DND, on one hand, and pyrrole polarity (1.82 D), on the other hand; (ii) pyrrole affinity for both polar and non-polar solvents [20] which makes difference of adsorbed Py amount due to hydrophobic and hydrophylic interactions with H-DND and O-DND (observed for adsorbed water molecules on DNDs [19]) negligible.

Thus, we can assume that PPy has different thickness in H-DND/PPy-3 and O-DND/PPy-3 due to the different type of bonding. Such effect was found on monocrystalline diamond. In Ref. [8], it was shown that PPy is chemisorbed to H-diamond, while in [11] PPy physisorption was evidenced on O-diamond. Theoretical calculations by Matunova et al. [26] show upright position of chemisorbed PPy relative to H-DND. Indeed, if we consider that interaction between H-DND and PPy is realized by analogy with bulk hydrogenated diamond-PPy interaction [8], then the covalent C–C bond is formed between carbon surface atom of DND and α-C atom of PPy chain. For such a reaction to happen, PPy chain, which consists of Py rings connected through α-C atoms [27], should be arranged so that α-C atom on the edge of PPy chain will be close to H-DND surface. It means that PPy chain should stand more or less upright relative to H-DND surface. To suggest the arrangement of physisorbed PPy around O-DND we consider that NH of neighboring Py rings of PPy chain point in the opposite directions [27] and form hydrogen bonds with oxygen-containing groups of O-DND surface. As there is an equal probability for NH bonds on both sides of PPy chain to form hydrogen bonds then we can assume
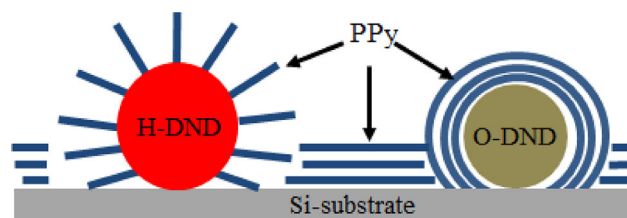
Figure 4 The scheme of PPy binding to H-DND, O-DND, and the Si substrate.

that PPy chains overlay O-DND surface. Further layers of PPy could build up via stacking interactions. Possible structural arrangement is schematically illustrated in Fig. 4.

5 Conclusions H-DND/PPy and O-DND/PPy composites were successfully fabricated by wet chemistry procedure. Based on the FTIR and AFM results: (i) uniform thin coating of DNDs by PPy has been achieved; (ii) different type of bonding in H-DND/PPy and O-DND/PPy was assumed with subsequent different PPy arrangement on H-DND and O-DND. Direct proof of the different bonding type in H-DND/PPy and O-DND/PPy composites is still missing though.

Nevertheless, the DND/PPy composites possess several properties that might be valuable for their use in photovoltaics. FTIR measurements revealed tight interactions between DNDs and PPy in H-DND/PPy and O-DND/PPy. PPy thickness in each of the composites is below typical exciton diffusion length in organic materials (10 nm). These features may be advantageous for efficient exciton collection from PPy and exciton dissociation at the PPy-diamond interface. Further research on the bonding nature in H-DND/PPy and O-DND/PPy composites as well as their (opto) electronic properties is going on.

References

[1] P. Saini, Fundamentals of Conjugated Polymer Blends, Co polymers and Composites: Synthesis, Properties, and Applications (Wiley-Scrivener, Somerset, 2015), pp. 9, 11, 307.

[2] M. T. Dang, L. Hirsch, and G. Wantz, Adv. Mater. **23**, 3597 (2011).

[3] E. A. Lukina, M. N. Uvarov, and L. V. Kulik, J. Phys. Chem. C **118**, 18307 (2014).

[4] X. Guo, C. Cui, M. Zhang, L. Huo, Y. Huang, J. Hou, and Y. Li, Energy Environ. Sci. **5**, 7943 (2012).

[5] S. Holliday, R. S. Ashraf, A. Wadsworth, D. Baran, S. A. Yousaf, C. B. Nielsen, C.-H. Tan, S. D. Dimitrov, Z. Shang, N. Gasparini, M. Alamoudi, F. Laquai, C. J. Brabec, A. Salleo, J. R. Durrant, and I. McCulloch, Nature Commun. **7**, 11585 (2016).

[6] S. Ren, M. Bernardi, R. R. Lunt, V. Bulovic, J. C. Grossman, and S. Gradečak, Nano Lett. **11**, 5316 (2011).

[7] Q. Liu, Z. Liu, X. Zhang, N. Zhang, L. Yang, S. Yin, and Y. Chen, Appl. Phys. Lett. **92**, 223303 (2008).

[8] B. Rezek, J. Čermák, A. Kromka, M. Ledinský, and J. Kočka, Diam. Relat. Mater. **18**, 249 (2009).

[9] T. V. Vernitskaya and O. N. Efimov, Russ. Chem. Rev. **66**, 443 (1997).

[10] P. S. Abthagir and R. Saraswathi, J. Appl. Polym. Sci. **81**, 2127 (2001).

[11] E. Ukraintsev, A. Kromka, W. Janssen, K. Haenen, and B. Rezek, Int. J. Electrochem. Sci. **8**, 17 (2013).

[12] M.-H. Hsu, H. Chuang, F.-Y. Cheng, Y.-P. Huang, C.-C. Han, J.-Y. Chen, S.-C. Huang, J.-K. Chen, D.-S. Wu, H.-L. Chu, and C.-C. Chang, ACS Appl. Mater. Interfaces **6**, 7198 (2014).

[13] D. Shin, B. Rezek, N. Tokuda, D. Takeuchi, H. Watanabe, T. Nakamura, T. Yamamoto and C. E. Nebel, Phys. Status Solidi A **203**, 3245 (2006).

[14] V. N. Mochalin, O. Shenderova, D. Ho, and Y. Gogotsi, Nature Nanotechnol. **7**, 11 (2011).

[15] H. Ashassi-Sorkhabi, R. Bagheri, and B. Rezaei-Moghadam, J. Mater. Eng. Perform. **25**, 611 (2016).

[16] B. Rezek, J. Čermák, A. Kromka, M. Ledinský, P. Hubík, J. J. Mareš, A. Purkrt, V. Cimrová, A. Fejfar, and J. Kočka, Nanoscale Res. Lett. **6**, 1 (2011).

[17] J. Čermák, B. Rezek, P. Hubík, J. J. Mareš, A. Kromka, and A. Fejfar, Diam. Relat. Mater. **19**, 174 (2010).

[18] R. Ashraf, A. Kausar, and M. Siddiq, Iran. Polym. J. **23**, 531 (2014).

[19] B. Pourabbas and F. Pilati, Synth. Met. **160**, 1442 (2010).

[20] S. Stehlik, M. Varga, M. Ledinsky, V. Jirasek, A. Artemenko, H. Kozak, L. Ondic, V. Skakalova, G. Argentero, T. Pennycook, J. C. Meyer, A. Fejfar, A. Kromka, and B. Rezek, J. Phys. Chem. C **119**, 27708 (2015).

[21] M. Can, H. Özaslan, Ö. Işıldak, N. Ö. Pekmez, and A. Yıldız, Polymer **45**, 7011 (2004).

[22] B. Rezek, D. Shin, H. Uetsuka, and C. E. Nebel, Phys. Status Solidi A **204**, 2888 (2007).

[23] M.-C. Bernard-Houplain and C. Sandorfy, Can. J. Chem. **51**, 1075 (1973).

[24] G. Socrates, Infrared and Raman Characteristic Group Frequencies: Tables and Charts (Wiley, Chichester, 2004).

[25] J. Lei, W. Liang, and C. R. Martin, Synth. Met. **48**, 301 (1992).

[26] P. Matunová, V. Jirásek, and B. Rezek, Phys. Status Solidi A **213**, DOI: 10.1002/pssa.201600228 (2016).

[27] Y. Tan and K. Ghandi, Synth. Met. **175**, 183 (2013).

STUDY OF PHOTOVOLTAGE STABILITY ON NANODIAMOND-POLYPYRROLE COMPOSITES BY KELVIN PROBE METHOD

[1,2]Yen-Chen CHANG, [1,2]Daria MILIAIEVA, [1,2]Bohuslav REZEK

[1] Institute of Physics of the Czech Academy of Science, Prague, Czech Republic, changyen@fzu.cz
[2] Faculty of Electrical Engineering, Czech Technical University, Prague, Czech Republic

Abstract

Diamond thin films and nanodiamond particles are considered promising for addressing the long-term challenge of organic photovoltaics: efficiency and stability. In this work, we characterize stability of surface potential and photovoltage on polyfunctional detonation nanodiamonds merged with polypyrrole oligomers. The polyfunctional-detonation nanodiamond (poly-DND), polypyrrole (PPy), and poly-DND/PPy composites were prepared on p-type silicon wafer substrates. In order to investigate illumination induced effects, surface potential and photovoltage of the samples were characterized by macroscopic Kelvin Probe method as a function of time. The poly-DND/PPy composite exhibits better stability of surface potential and surface photovoltage in short-term as well as in long-term (up to 8 weeks) compared to individual materials. The nanodiamond composites thus appear advantageous for use in organic photovoltaics.

Keywords: Diamond, nanoparticles, polypyrrole, scanning Kelvin probe

1.   INTRODUCTION

Organic-based photovoltaic (OPV) devices are not so much limited in output under low-light or diffuse light conditions compared with silicon PV modules. OPV production and installation is also easy on large areas and in various shapes as they can be made on polymer foils. However, the main drawback of OPV is their long-term instability due to various chemical degradation processes and susceptibility to humidity. Many solutions including non-fullerene inorganic acceptors are being investigated. Diamond may provide interesting properties in this respect. The diamond interface with polypyrrole (PPy) was already shown to promote exciton generation and dissociation [1]. This property of the hybrid diamond/PPy composite may be thus beneficial to generate free charge. For this purpose it may be beneficial to use diamond in form of nanoparticles, so called nanodiamonds, which are commercially available in large quantities. Similarly as bulk diamond, nanodiamonds are reported as non-toxic [2,3] and generally chemically stable [4]. Synthesis process and structural interactions in nanodiamond/PPy composite were recently reported in our previous article [5]. In this work, opto-electronic properties of such composite are studied by Kelvin Probe. We present time-resolved measurements [6] of surface potential in dark and under illumination and we assess how stable the photovoltage of the nanodiamond-dye composite is compared with individual materials.

2.   MATERIALS AND METHODS

We employed commercially available polyfunctional detonation nanodiamonds (NanoAmando) with oxygen and hydrogen surface chemical groups (poly-DND). The poly-DND particles, polypyrrole (PPy), or poly-DND/PPy composite were deposited on p-type silicon wafers according to the established protocol [5]. Briefly, the substrates were covered with poly-DND particles using 1 hour ultrasonication in aqueous colloidal poly-DND solution with concentration of 20 mg/mL [7] and then rinsed with deionized water. The process leads to a dense coverage by poly-DND [5]. The substrate with poly-DND layer was immersed in Py monomer solution (98 %) for 1 hour in dark to adsorb Py monomers on the nanodiamonds. The substrate

with adsorbed Py was immersed into HCl acid (0.3 M) for 16 hours under indoor illumination to induce polymerization. Finally, the sample was taken out, rinsed with deionized water, and blown dry with nitrogen.

Scanning Kelvin probe (SKP) method was used to determine the surface potentials [6,8] of the samples in dark and under illumination with light intensity of about 200 W/m^2 (white cold light source with halogen lamp). SKP setup is shown in Figure 1 (a). Figure 1 (b) is the detailed photograph of the sample in Kelvin probe setup. Measurement of each sample was conducted with a gold-plated tip electrode of 2 mm in diameter. The surface potential was detected at similar location on the sample in each measurement. At first, we measured surface potential in dark and waiting till it was stable for 100 seconds. Then we turned the light on quickly within 5 seconds and kept measuring the potential for 100 seconds. The procedure was continuously repeated during 12 min. Finally the measurement was stopped in the dark. Then the surface photovoltage was calculated from the surface potential data.
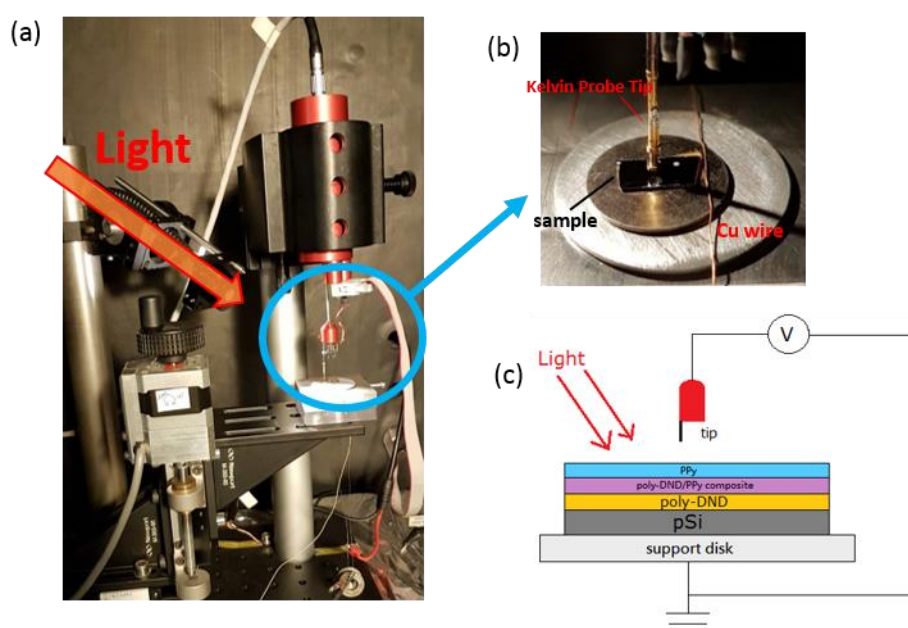

Figure 1 (a) Photograph of Scanning Kelvin probe setup. (b) Detailed photograph of the sample in Kelvin probe setup. (c) The scheme of macroscopic Scanning Kelvin Probe measurement with poly-DND/PPy composite.

3.   RESULTS AND DISCUSSION

Figure 2 shows the results of surface potential (SP) measurement in the short-term. We can see that all surface potentials are stable (within 6 mV of standard deviation) and regularly reproducible during light switching in each measurement. Thus we averaged the whole surface potential measurement data in dark and under illumination for each material. The averaged surface potential with standard deviation in dark and under illumination was: pSi (-101 ± 6 mV and -272 ± 5 mV), PPy (-189 ± 3 mV and -311 ± 5 mV), poly-DND (-34 ± 4 mV and -230 ± 6 mV), and poly-DND/PPy composite (-202 ± 4 mV and -69 ± 3 mV).
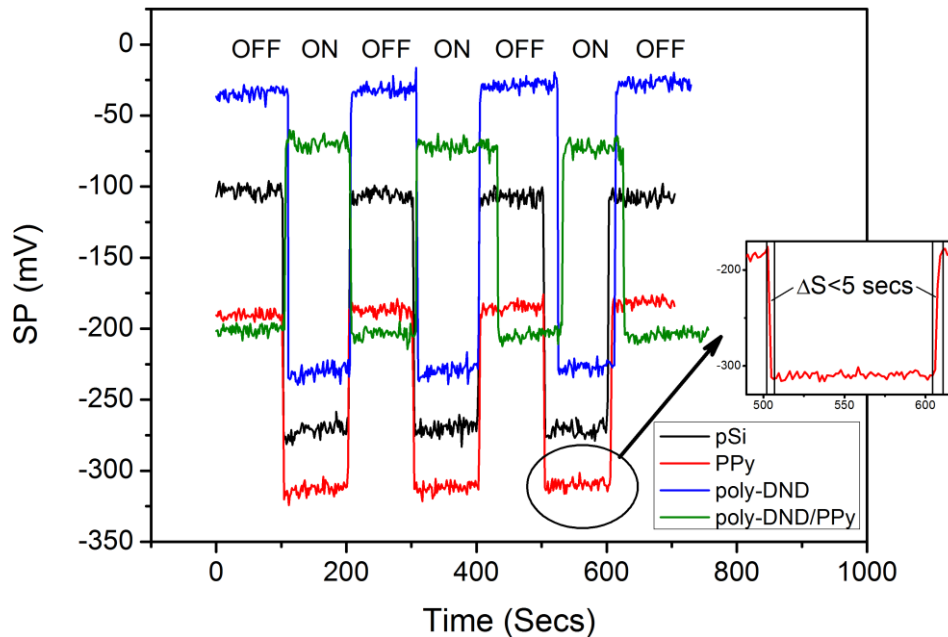
Figure 2 Surface potential of pSi, PPy, poly-DND, poly-DND/PPy as a function of time and visible light illumination in the short-term (0 – 12 min). The potential profiles correspond to measurements after 7 weeks. The inset shows that the rise and fall edges when illumination changes.

Then we repeated the short-term measurements every week for 8 subsequent weeks to investigate the long-term stability. Shape of the short-term profiles with the fast rise and fall edges was the same for the whole 8 weeks. Thus we averaged Kelvin Probe data in dark and under illumination each week. The averaged potential in dark and under illumination is plotted in Figure 3. Standard deviation of the average value is used as the error bar. We can see that in the long-term (during 8 weeks), the potentials in dark and under illumination are slowly fluctuating. The potential fluctuations are qualitatively very similar for all the studied materials, hence they are most likely related with some external factors.
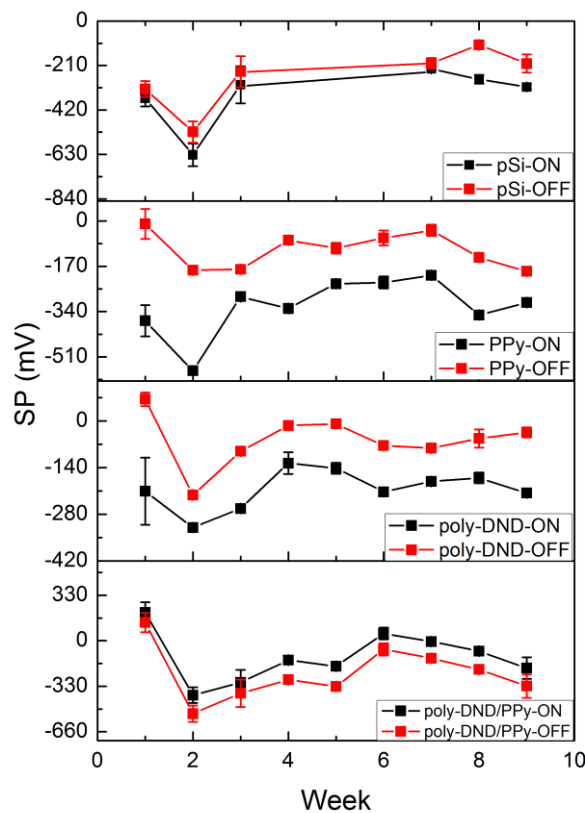
Figure 3 Average value of surface potential in dark and under illumination plotted as a function of time for the long-term stability evaluation.

The surface potentials exhibit similar fluctuation in dark and under illumination. Evaluation of surface photovoltage was thus use to observe actual material (in)stability in spite of the overall potential fluctuations. In Figure 4 (a) presents surface photovoltage (SPV) that was calculated as ($SP_{illumination}$ - SP_{dark}) each week for 8 weeks.

SPV exhibits the most pronounced changes during the first 3 weeks (area I), than during the remaining 6 weeks it seems fluctuating around a stabilized value (area II). To characterize this (in)stability, we calculated average SPV and its standard deviation in each area (values at the boundary were accounted for in both areas). The averaged SPV values with standard deviation in area I and area II are: pSi (-85 ± 33 mV and -91 ± 59mV), PPy (-281 ± 155 mV and -166 ± 55 mV), poly-DND (-182 ± 90 mV and -137 ± 30 mV), and poly-DND/PPy (95 ± 33 mV and 124 ± 22 mV).

Figure 4 (b) shows in the form of bar graph the standard deviation as a measure of SPV (in)stability. We can see the standard deviation difference of the averaged SPV between area I and area II on pSi (33 mV and 59 mV), PPy (155 mV and 55 mV), poly-DND (90 mV and 30 mV), and poly-DND/PPy (33 mV and 22 mV). The minimum standard deviation is observed on poly-DND/PPy composite during the whole 8 weeks.
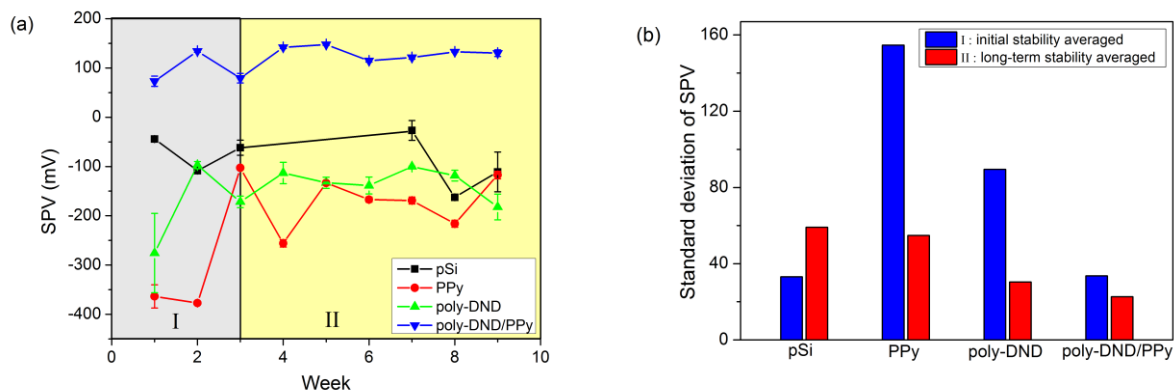
Figure 4 (a) Surface photovoltage (SPV) of all the materials for 8 weeks. Area I is defined as initial stability and area II as long-term stability. (b) The standard deviation of the averaged SPV value.

Thus the SPV of the poly-DND/PPy composite was the most stable from the very beginning after fabrication till the last measurement after 8 weeks. The material interaction in poly-DND/PPy composites thus contributes to photovoltage stability [6,9]. Note in this respect that surface photovoltage of of poly-DND/PPy composite has opposite (positive) sign compared the SP of pSi, PPy and poly-DND. Such positive charging of the surface, i.e. polypyrrole, is in agreement with theoretical atomic scale calculations [10] and indicates role of nanodiamonds as electron acceptors. This effect together with polypyrrole tight binding to nanodiamond may explain the improved stability of the composite.

4. CONCLUSION

In the range of minutes, surface potential (SP) under dark and illumination was stable and well reproducible for all the materials. In the long-term (weeks), the surface potentials of all materials were slowly fluctuating in similar way, most likely due to external factors. The generated photovoltage revealed actual material stability. The photovoltage was the most stable in the case of the poly-DND/PPy composite compared with individual materials. The improved stability is most likely due to the tight material interaction in poly-DND/PPy composites and nanodiamond acting as an electron acceptor. Nanodiamond composites may be thus advantageous for improving organic photovoltaics.

ACKNOWLEDGEMENTS

REFERENCES

[1] REZEK, B., ČERMÁK, J., KROMKA, A., LEDINSKÝ, M., and KOČKA, J. Photovoltage Effects in Polypyrrole–Diamond Nanosystem. *Diamond and Related Materials.* 2009. vol. 18, no. 2–3, pp. 249–252. Available from: DOI: 10.1016/j.diamond.2008.07.019.

[2] VAIJAYANTHIMALA, V., TZENG, Y.K., CHANG, H.C., and LI, C.L. The Biocompatibility of Fluorescent Nanodiamonds and Their Mechanism of Cellular Uptake. *Nanotechnology.* 2009. vol. 20, no. 42, p. 425103. Available from: DOI: 10.1088/0957-4484/20/42/425103.

[3] SCHRAND, A.M., HENS, S.A.C., and SHENDEROVA, O.A. Nanodiamond Particles: Properties and Perspectives for Bioapplications. *Critical Reviews in Solid State and Materials Sciences.* 2009. vol. 34, no. 1–2, pp. 18–74. Available from: DOI: 10.1080/10408430902831987.

[4]   KOZAK, H., REMES, Z., HOUDKOVA, J., STEHLIK, S., KROMKA, A., and REZEK, B. Chemical Modifications and Stability of Diamond Nanoparticles Resolved by Infrared Spectroscopy and Kelvin Force Microscopy. *Journal of Nanoparticle Research.* 2013. vol. 15, no. 4, p. 1568. Available from: DOI: 10.1007/s11051-013-1568-7.

[5]   MILIAIEVA, D., STEHLIK, S., STENCLOVA, P., and REZEK, B. Synthesis of Polypyrrole on Nanodiamonds with Hydrogenated and Oxidized Surfaces. *Physica Status Solidi (A).* 2016. vol. 213, no. 10, pp. 2687–2692. Available from: DOI: 10.1002/pssa.201600278.

[6]   REZEK, B., ČERMÁK, J., KROMKA, A., LEDINSKÝ, M., HUBÍK, P., MAREŠ, J.J., PURKRT, A., CIMROVÁ, V., FEJFAR, A., and KOČKA, J. Synthesis, Structure, and Opto-Electronic Properties of Organic-Based Nanoscale Heterojunctions. *Nanoscale Research Letters.* 2011. vol. 6, no. 1, p. 238. Available from: DOI: 10.1186/1556-276X-6-238.

[7]   STEHLIK, S., VARGA, M., LEDINSKY, M., JIRASEK, V., ARTEMENKO, A., KOZAK, H., ONDIC, L., SKAKALOVA, V., ARGENTERO, G., PENNYCOOK, T., MEYER, J.C., FEJFAR, A., KROMKA, A., and REZEK, B. Size and Purity Control of HPHT Nanodiamonds down to 1 nm. *The Journal of Physical Chemistry C.* 2015. vol. 119, no. 49, pp. 27708–27720. Available from: DOI: 10.1021/acs.jpcc.5b05259.

[8]   ČERMÁK, J., KOIDE, Y., TAKEUCHI, D., and REZEK, B. Spectrally Dependent Photovoltages in Schottky Photodiode Based on (100) B-Doped Diamond. *Journal of Applied Physics.* 2014. vol. 115, no. 5, p. 053105. Available from: DOI: 10.1063/1.4864420.

[9]   ZHONG, Y.L., MIDYA, A., NG, Z., CHEN, Z.K., DAENEN, M., NESLADEK, M., and LOH, K.P. Diamond-Based Molecular Platform for Photoelectrochemistry. *Journal of the American Chemical Society.* 2008. vol. 130, no. 51, pp. 17218–17219. Available from: DOI: 10.1021/ja805977f.

[10]   MATUNOVÁ, P., JIRÁSEK, V., and REZEK, B. Computational Study of Physisorption and Chemisorption of Polypyrrole on H-Terminated (111) and (100) Nanodiamond Facets. *Physica Status Solidi (A).* 2016. vol. 213, no. 10, pp. 2672–2679. Available from: DOI: 10.1002/pssa.201600228.